Understanding Star Formation in the Perseus Molecular Cloud

by

Helen Marjorie Kirk
Hon.B.Sc., University of Toronto, 2003

A Dissertation Submitted in Partial Fulfillment of the
Requirements for the Degree of

MASTER OF SCIENCE

in the Department of Physics and Astronomy

Contents

List of Tables

List of Figures

Supervisor: Dr. Doug Johnstone
Co-Supervisor: Prof. Don VandenBerg

ABSTRACT

We present an analysis of ∼3.5 square degrees of submillimetre continuum and extinction data of the Perseus molecular cloud. We identify 57 clumps in the submillimetre map and we identify 29 structures ('cores') and 14 associations of cores ('super cores') in the larger extinction map. The cumulative mass distribution of the submillimetre clumps and extinction cores have steep slopes (α of $\sim 2{\pm}0.1$ and 1.8 ± 0.1 respectively), steeper than the Salpeter IMF ($\alpha = 1.35$), while the distribution of extinction super cores has a shallow slope ($\alpha = 0.8 \pm 0.2$). Most of the submillimetre clumps are well fit by stable Bonnor-Ebert spheres with 13 K $<$ T $<$ 25 K and $5.5 < \log_{10}(\mathrm{P}_{ext}/\mathrm{k}) < 6.2$. The clumps are found only in the highest column density regions ($\mathrm{A}_V >$ 5-7 mag), although Bonnor-Ebert models suggest that we should have been able to detect them at lower column densities if they exist. This is similar to the extinction threshold found in the Ophiuchus molecular cloud (Johnstone, Di Francesco, & Kirk 2004). The relationship between submillimetre clumps and their parent extinction core has been analyzed. Extinction cores containing structure have approximately a Jeans mass of submillimetre clumps, which is fragmented into a larger number of clumps in the higher mass cores. The mass of the submillimetre clumps tends to be more concentrated toward the core centre than the total core mass. The submillimetre clumps, however, tend to lie in preferential directions just off of the peak, suggesting an external triggering event is responsible for their formation.

Supervisor: Dr D. Johnstone (Herzberg Institute for Astrophysics, Department of Physics and Astronomy)
Co-Supervisor: Prof. D. VandenBerg (Department of Physics and Astronomy)

Acknowledgements

I am grateful for the tremendous support, encouragement, and inspiration from my supervisor, Dr. Doug Johnstone, as well as from Dr. James DiFrancesco, who has become an unexpected and most welcome surrogate advisor. It has been a remarkable and enjoyable adventure and I am excited to embark on the challenges ahead. A big thank you to my family and friends in both Ontario and Victoria who have been there for me along the way — you are much appreciated! A final word of thanks to my excellent teachers in high school, especially Mr. Krawczyk who introduced me to physics.

Chapter 1

Introduction

The study of the formation of stars and the molecular cloud environment in which this occurs is important. Without the formation of the Sun, we would not exist. Understanding how planets are able to form requires that the formation of the parent star be well understood first. Stars are responsible for the formation of most of the heavy elements in the Universe and also contribute a significant amount of the radiation observed. They are a primary building block of galaxies, and their formation can play an important role in understanding the outcome of galaxy mergers, for example. Since the process of star formation begins within molecular clouds, this environment must also be understood.

1.1 Early Observations

Molecular clouds were first discovered as patches in the sky lacking visible stars. Initially, the popular theory was that these regions actually had an absence of stars. Careful observations in the early twentieth century began to suggest that instead of being empty, these regions were 'dark nebulae' (or dark clouds) where starlight was obscured (e.g., Barnard 1913) by an unknown source. The existence of 'dark nebulae' as tangible objects encouraged further in-depth studies of them, leading to photographic catalogs (e.g., Barnard 1919), and later, quantified studies attempting to measure the extinction and proper motion of the clouds (e.g., Hiemstra 1938).

The development of radio telescopes for astronomical observations later led to the discovery of molecules in the dark clouds (e.g., Palmer et al. 1969; Wilson et al. 1970). CO was (and continues to be) a popular molecule to observe, as it is the most abundant molecule after H_2. Surveys of the Galactic plane in CO (e.g., Dame et al. 1987) allowed the discovery and characterization of nearby molecular clouds in the galaxy. The local molecular clouds were found to have a scale height corresponding to a half width at half maximum of 87 pc with a mean density at the midplane of 0.0068 $M_\odot$ pc^{-3}, corresponding to ~ 0.1 cm^{-3} (Dame et al. 1987). The molecular clouds are concentrated along the Galactic plane and towards the northern quadrants due to the Sun's proximity to the closest spiral arm.

Advances in detectors have allowed large scale CO maps to be made efficiently at reasonable resolution. These maps are effective in providing rich details into the overall substructure of molecular clouds (e.g., Kramer et al. 1998; Onishi et al. 1998). The molecular cloud structure traced in the CO maps has been found to have a power-law distribution of mass on the large scale (e.g., Williams, de Geus, & Blitz 1994).

Problems became apparent in the interpretation of the CO observations, however, in comparisons with observations of other molecular species on the smaller scale of dense cores. CO observations indicated that the density *decreased* in regions where other molecules implied increasing densities. This discrepancy in densities was eventually solved through the discovery of CO depletion in cold, high density regions through preferential freeze out onto dust grains (Tafalla et al. 2002). Other molecules such as N_2 were found to be less prone to such freeze out, leading to higher levels of nitrogen bearing molecules such as N_2H^+ (some of which are actually predicted to form more frequently due to the removal of a competing chemical reaction associated with the CO). Thus dense regions are best traced by molecular species such as N_2H^+ for which freeze out is less of a concern. Due to the higher critical density of N_2H^+ $J = 1 \rightarrow 0$ ($n_{cr} \sim 10^5$ cm^{-3}; Womack, Ziurys, & Wyckoff 1992), it is not a suitable tracer of density in the low density regions.

Concurrent with the development of molecular line observations were continuum observations. The dust grains responsible for the extinction of starlight first noted in optical observations of 'dark clouds' offer an alternate method to discern the structure of molecular clouds. The dust grains emit thermal radiation in the infrared which can be observed, however, absorption and emission of water molecules in the Earth's atmosphere make observations over much of the wavelength regime impossible by ground-based telescopes.

The atmosphere can be avoided through balloon-borne or space-based telescopes — such as IRAS, and more recently the Spitzer Space Telescope (SST). Observations from the IRAS satellite (Neugebauer et al. 1984) provided complementary infrared data in the mid 1980's that were used to derive the dust temperature and gas column density of the clouds as well as to detect the young stars and protostars still enshrouded in dust (e.g., Kuiper et al. 1987). IRAS was designed to detect the mid-infrared light emitted by warm dust (i.e. dust at temperatures of several hundred Kelvin). These temperatures are ideally suited for the detection of evolved protostars which warm their surroundings with emission, but IRAS cannot detect the dense clumps from which these protostars form due to their colder temperatures of tens of Kelvin. (Note that the SST's longest wavelength observations are suitable for such detections.)

Ground-based observations in the millimetre and submillimetre present another method to observe the cold dust. Several wavelength bands exist where the atmosphere can be transparent to water vapour, etc. Observations in these bands still require considerable effort to remove the effects of the atmosphere, and usually employ a technique that effectively removes information on the larger scales of the structure (see the following chapter for a discussion of observational techniques). Structure on the small scale (containing on the order of several solar masses) can still be effectively observed (e.g., Motte et al. 1998). A further drawback with any continuum observation is that only 2-dimensional data is obtained, with no information about the third dimension such as velocity, as is obtained with spectra. In crowded fields, this can lead to multiple objects overlapping in projection to produce an apparent single object in the data with no measure available to distinguish between them. Thermal emission by dust, however, is less sensitive to the chemical and excitation effects that complicate interpretation of line observations. For a given column density, thermal dust emission is dependent only on temperature and dust opacity which can be reasonably constrained.

Traditionally, submillimetre observations have focussed on small regions of previously known star formation activity, ignoring the cloud as a whole to maximize observing efficiencies. Advances in detector sensitivities have led to the recent development of large (degree) scale surveys [notably Johnstone, Di Francesco, & Kirk (2004)'s study of the Ophiuchus molecular cloud included as Appendix A and Hatchell et al. (2005)'s study of the Perseus molecular cloud]. Large area surveys unbiased towards previously known star formation sites such as these have the potential to provide clues into the large scale environment of molecular clouds and hence the role of both turbulent and magnetic support in the cloud and the formation of substructure.

Observations of molecular clouds over a range of scales have revealed that they have a hierarchical, possibly fractal structure (e.g., Sánchez et al. 2005). Discussion about the structure on the various scales is complicated by the lack of standard terminology used to describe these structures. In this work, clouds represent the largest structure, possessing sizes around 50 pc and containing tens of thousands of solar masses of material. We define cores as denser regions spanning tenths of a parsec and containing hundreds to thousands of solar masses. Clumps are defined as the small dense regions spanning hundredths of a parsec and containing $\sim 1/10$ to 10 $M_\odot$ of material. Clumps are the progenitors of stars, although not all may collapse to form stars, and others may fragment to form a system containing several objects.

1.2 Theoretical Framework

Here we introduce the theoretical concepts which comprise the basic star formation framework.

1.2.1 Jeans Mass

Molecular clouds require support on the largest scales to prevent collapse. The Jeans mass (M_J), the maximum mass in which thermal pressure alone provides sufficient support to counteract gravitational collapse, is

$$\mathrm{M_J} \approx \left(\frac{\pi^{3/2}}{\mathrm{G}^{3/2}\ \mu^{1/2}\ \mathrm{m_H^{1/2}}} \right)\ \mathrm{c_s^3 n^{-1/2}} \tag{1.1}$$

(from Hartmann 1998), where c_s is the sound speed, G the gravitational constant, μ the mean molecular weight ($\sim$ 2.35), m_H the mass of a proton, and n the mean number density. For typical molcular cloud conditions (i.e., n $\approx 10^2$ cm^{-3} and temperature T $\approx$ 10 K), the Jeans mass is $\sim$500 $M_\odot$. Molecular clouds contain tens of thousands of solar masses of material, and therefore significant additional support must be present unless the entire cloud is in a state of dynamic collapse. In the following subsections, we describe the various models of star formation and how the above applies.

1.2.2 Magnetic Support

Magnetic fields have been thought to be important in molecular clouds for many years. Mestel & Spitzer (1956) outlined the effect of magnetic fields in the formation of clumps that can collapse to form stars. The equilibrium state of magnetized molecular clouds was calculated and analyzed in further detail by Mouschovias (1976) and others. Shu, Adams, & Lizano (1987) propose in their 'standard model' of star formation that magnetic fields threading star forming regions are the key to support of molecular clouds. The model expands on the work mentioned above as well as that by others to present a detailed theory for magnetically mediated star formation. Ionized species are tied to the magnetic field lines and may not move perpendicular to them in the case of a strong magnetic field (termed 'subcritical' if the field strength is large enough to prevent the collapse of the cloud). Neutral species, on the other hand, are not directly affected by the magnetic field and are able to move perpendicular to the field lines to form denser regions. This process, known as ambipolar diffusion, is a slow one because moving perpendicular to the field lines also involves moving through the ions which are tied to the field. After a period of time, neutral material can build up a dense enough region for the gravitational pull to be sufficient for the ions to overcome the magnetic fields (forming a 'supercritical' region) and allowing for collapse into a protostar. The timescale for ambipolar diffusion is slower for higher densities of ions due to the more frequent neutral-ion collisions. The densest regions of the molecular cloud, where cosmic rays are the sole source of ionization, are the only regions that have a structure formation timescale that is not prohibitively long (McKee 1989). The timescale for collapse is

$$\mathrm{t_{AD}} \simeq 1.6 \times 10^{14}\ \phi_{\mathrm{AD}}\ \mathrm{x_e}\ \mathrm{yrs} \tag{1.2}$$

where ϕ_{AD} is a constant of order unity and x_e is the ionization fraction. Observations show the ionization fraction is on the order of 10^{-7} (Williams et al. 1998), yielding an ambipolar diffusion timescale of $\sim 10^7$ yr.

Magnetic field strengths, often measured through Zeeman line splitting, have been observed to be strong enough to play an important role in molecular cloud support, although they may not be strong enough for regions to be subcritical (Crutcher 1999). Regardless of their strength, magnetic fields are only able to provide support across field lines, not along them. Without some other source of support, clouds would collapse to form sheet-like structures.

1.2.3 Turbulent Support

An alternate theory of support which has recently gained popularity in the star formation community is that of turbulent support (see MacLow & Klessen 2004, for a review). Under the turbulent support scenario, fast (often supersonic) motions of large scale flows in the cloud prevent global collapse, while smaller regions where these flows intersect may be unstable to collapse. One of the difficulties with the turbulent support model is the source of the turbulence. Without a driving source, turbulence will dissipate in a region quickly due to shocks, etc (MacLow & Klessen 2004).

Simulations without a driving source for turbulence find that collapse of substructure occurs after the turbulence has died away (Tilley & Pudritz 2004). Turbulent damping takes a longer time in simulations of a few Jeans masses and result in the formation of a few massive clumps. Simulations containing many Jeans masses, however, show that turbulence decays faster and allows for the formation of many clumps, with a mass distribution similar to that observed in dust clumps (detected by SCUBA) in molecular clouds (Tilley & Pudritz 2004).

Many simulations do include a driving source for turbulence, arguing that since turbulence is universally observed with very similar properties (e.g. small variations in structure function parameters), it must be driven on the largest scales (Heyer & Brunt 2004). The source of the driving is not certain, although possibilities considered include supernovae from a previous generation of star formation or collisions of large scale diffuse atomic flows (see MacLow & Klessen 2004, for a more complete listing and discussion). The driving of the turbulence must take place on large scales in order to match the observations above; however, this typically leads simulations to produce a star formation efficiency much larger than is observed. Typically, only a few percent of the total mass of a molecular cloud is converted into stars, although high density cluster regions have efficiencies on the order of 20% (Lada & Lada 2003). In turbulent simulations, the star formation efficiency has been found to scale with the driving scale of the turbulence (e.g., MacLow & Klessen 2004). The inclusion of magnetic fields can help to reduce the star formation efficiency through lowering the number of collapsing clumps that are able to form, while having little effect on the formation timescale of an individual clump (Vázquez-Semadeni et al. 2005).

In both the driven and non-driven cases, the formation timescale is several dynamical timescales of the cloud, given by

$$\mathrm{t_{ff}} = \left(\frac{3\pi}{32\ \mathrm{G}\ \mu\ \mathrm{m_H}} \right)^{1/2}\ \mathrm{n}^{-1/2} \tag{1.3}$$

(from MacLow & Klessen 2004), giving a timescale of $\sim 10^6$ yr.

Regardless of the present simulations, observations of supersonic linewidths have been well documented in molecular clouds for many years (for example, see Larson 1981), indicating that turbulent effects are important to consider.

1.2.4 Triggering

In the above two theories, the molecular cloud as a whole is viewed in a quasi-equilibrium manner (static or dynamic), isolated from its surrounding environment. This is more explicit in the magnetic support model where the magnetic fields evolve quasi-statically and less explicit in the turbulence scenario where simulations are only of the interior regions of the cloud. Periodic boundary conditions are usually used under the assumption that all surrounding regions are similar. Other effects, such as the role of nearby massive stars or the instability of the outer cloud edge could have a significant impact on the evolution of a region.

The theory of triggered star formation, an idea that has been around for many years (see the review by Elmegreen 1998), explicitly considers the above effects. Triggering can take on different forms depending on the scale on which it occurs. On the smallest scale, ('globule-squeezing' in Elmegreen 1998), pre-existing structure is compressed, causing collapse into protostars. One possible example of this type of triggering source is high pressures originating in expanding HII regions of nearby O and B stars. On intermediate scales ('collect and collapse' in Elmegreen

1998), pre-existing material in a cloud is collected into a higher density region, which then would be able to form substructure and collapse. This could occur on the edge of an expanding HII region, for example. On the largest scales ('shells and rings' in Elmegreen 1998), expansion around a high pressure source leads to material outside of the initial dense region being swept up into shells or rings which are then able to form substructure and collapse.

Larger scale triggering can also be linked to the formation of the entire molecular cloud. Hartmann et al. (2001) propose a scenario wherein regions of sufficient densities to contain molecular species form as part of large scale processes such as interacting HI flows generated by expanding shells. In such a situation, the formation and dispersion of the entire molecular cloud is linked to the same processes that control the formation of the stars within the region.

Edge effects also play an important role in all of the above — Burkert & Hartmann (2004) demonstrate that gravity alone acting on inhomogeneities in the outer boundary of a collapsing sheet can lead to fragmentation into filamentary geometries as well as the generation of supersonic infall motions typically interpreted as being turbulent in origin.

In all of the above triggering scenarios, magnetic fields and turbulence can still play a role, although the nature and importance of this is different in the different scenarios. For example, in the 'globule-squeezing' type of scenario, the initial structure would be formed through some influence by turbulent and magnetic support, but neither directly leads to the collapse of this structure. Chapter 7 discusses some interesting results we find which suggest small-scale triggering may be important in Perseus.

1.2.5 Timescales

One major predicted difference between the magnetic and turbulent support framework is the timescale for the formation of stars. Observationally, the formation timescale is still open to debate. For example, Hartmann et al. (2001) argue that observations imply short formation timescales while Tassis & Mouschovias (2004) argue that the data do not rule out long timescales for the initial formation stages. Young & Evans (2005) present simulations (under non-turbulent initial conditions) of the evolution of a protostar from class 0 to II [the observation-based evolutionary classes progress from 0 to III (developed in Adams et al. 1987) and are followed by the main sequence stage]. The results depend on both the mass of the protostar and the observational measure used to define the evolutionary class, but show formation timescales of the order of a few 10^5 yrs. Recent work including both turbulent and magnetic effects has shown a convergence of the short- versus long-timescale predictions. Inclusion of magnetic effects in a turbulence-dominated regime has shown an increase in the formation timescale of the entire simulated region (Vázquez-Semadeni et al. 2005) and inclusion of turbulence in the magnetic-dominated regime has been shown to shorten the ambipolar diffusion timescale (Nakamura & Li 2005).

A second important measure is the dispersion in ages across a region. Hartmann et al. (2001) argue that observations show some molecular clouds have a small dispersion in ages between one edge and the other. In fact, such a small dispersion is seen that the difference is too small for any local triggering to propagate from one end of the cloud to the other. Large scale triggering would be required to cause the formation of stars in such distant locations over a small time. Alternatively, Palla & Stahler (2002) argue that the ages of young stars in some molecular clouds (eg the Taurus-Auriga complex) show evidence for continual star formation (albeit with an increasing rate) over roughly the last 10^7 yrs. This would argue against molecular clouds as existing only for a few dynamical times.

1.3 This Work

In this work, we analyze observations of the Perseus molecular cloud with both submillimetre continuum and extinction maps to investigate evidence supporting or conflicting with the star formation and molecular cloud support scenarios discussed above.

This chapter provided an overview of observations of molecular clouds as well as current theories on how they are supported and how structure within them is able to form and further collapse into stars.

Chapter 2 presents our submillimetre observations (plus archival data) of a large region (several square degrees) of the Perseus molecular cloud. These are a part of the CO-ordinated Molecular Probe Line Extinction and Thermal Emission (COMPLETE) Survey (see `http://cfa-www.harvard.edu/COMPLETE`) whose goal is to provide insight into star formation through observations of three nearby molecular clouds; namely Perseus, Ophiuchus, and Serpens which are also observed in the Spitzer 'c2d' program (Evans et al. 2003). The extensive multi-wavelength coverage the COMPLETE survey provides over large common regions will provide statistical measures to aid in answering some of the many questions remaining in how stars form. In this work, we use both submillimetre observations as well as extinction data from the COMPLETE survey. The region covered includes the well-known star forming regions of B5, B1, IC348, NGC1333, L1455, and L1448. The observational and data reduction procedures are also presented in Chapter 2.

In Chapter 3, we explain our procedure for identifying structure in both the submillimetre and extinction maps. We then investigate basic properties of the structures identified. We calculate the mass distribution of structures in both the submillimetre and extinction, and further model the submillimetre structure as Bonnor-Ebert spheres.

In Chapter 4, we compare the submillimetre clump locations to the extinction map, representing the large scale structure of the molecular cloud. We demonstrate that clumps do not form in regions of low extinction ($<$ 5-7 mag).

In Chapter 5, we further analyze the relation between submillimetre and extinction structure in terms of bulk submillimetre clump properties within the local dense extinction cores.

In Chapter 6, we discuss possible evidence of triggered star formation in the Perseus molecular cloud and how it corresponds to the different scenarios discussed in this chapter.

In Chapter 7, we summarize the work presented here and discuss future directions for research.

Appendix A and B contain published and accepted papers relating to the research presented here. Appendix C provides definitions of frequently used symbols in this work for easy reference.

Chapter 2

Observations / Data Reduction

2.1 Submillimetre Continuum

Submillimetre data at 850 μm of the Perseus molecular cloud were obtained using the Submillimetre Common User Bolometer Array (SCUBA) on the James Clerk Maxwell Telescope (JCMT) on Mauna Kea[1]. The data we present here are a combination of our own observations (∼1.3 square degrees) with publicly available archival data[2] for a total of ∼3.5 square degrees.

SCUBA is an array of bolometers that can currently observe at 850 μm and 450 μm bands, where atmospheric windows exist. SCUBA has a dichroic mirror which allows both bands to be simultaneously observed, allowing an approximate determination of the dust temperature to be made. Data at 450 μm, however, require finer sampling due to higher resolution at shorter wavelengths, and thus a region requires more time to be mapped at 450 μm. Furthermore, the opacity

---

[1] The JCMT is operated by the Joint Astronomy Centre in Hilo, Hawaii on behalf of the parent organizations Particle Physics and Astronomy Research Council in the United Kingdon, the National Research Council of Canada and The Netherlands Organization for Scientific Research.

[2] Guest User, Canadian Astronomy Data Centre, which is operated by the Dominion Astrophysical Observatory for the National Research Council of Canada's Herzberg Institute of Astrophysics.

of the sky at 850 μm is less affected by weather changes than at 450 μm. As temperature information was not crucial for our study and as we wished to cover the maximum area possible, we chose to use SCUBA's 'fast scan' observing mode which allows large regions of the sky to be mapped quickly but provides only 850 μm data (with a sampling of $6''$). Scan maps in SCUBA consist of scanning back and forth across the sky to fill uniformly the desired region using all of the bolometers in the array. (The separation of the bolometers leads to gaps within the data map for a fixed pointing of the telescope.) Throughout the movement of the scan, the secondary mirror is switched between two positions (known as two-point chopping), typically separated by $\sim 30''$ on the sky, to produce a difference map. The chops are much faster than the scanning speed, and thus can be thought of as taking place independently. The chopping procedure helps to eliminate spurious signal from varying atmospheric conditions and as well as within the instrument. Each fast scan observation consists of a $\sim$400 square arcminute field which is scanned by the array six times using different chopping amplitude and direction. We scan along the three principal axes of the bolometer array (the bolometers are arranged in a hexagonal pattern) and chop along the scan using $30''$ and $44''$ chops. These parameters were chosen in order to complement the matrix inversion map reconstruction technique (Johnstone et al. 2000a), discussed in more detail below. The data from all fields can be combined to create the final map.

Following the standard procedure, all of the raw data were first flat-fielded and extinction corrected using the standard SCUBA software (Holland et al. 1999). This procedure converts the difference measures from electronic signals into observed flux differences, accounting for sky emission through sky opacity measurements taken at the nearby CSO telescope (at $\lambda = 1330$ μm) combined with less frequent skydips taken with SCUBA. The CSO opacity measurements for a night are fit to a polynomial and converted into opacities at the 850 (and 450) μm bands using the SCUBA skydips for calibration. To convert the corrected difference measures into an image, we apply the matrix inversion technique of Johnstone et al.

(2000a), which was shown to better reproduce images from chopped data than other commonly used procedures such as the Emerson technique for Fourier deconvolution (Emerson et al. 1979), commonly employed at the JCMT. The matrix inversion technique has several other advantages. The Emerson technique requires chopping in fixed co-ordinates on the sky which often forces the direction of the scan and chop to differ; the matrix inversion technique has greater flexibility in scan and chop directions, allowing for chopping in the direction of the scan. Chopping along the scan provides an additional contraint in the map reconstruction since the total difference along the length of the scan should be zero. Including this additional constraint allows for correction of effects such as a non-zero baseline signal. The matrix inversion technique is also better suited for data sets with non-uniform noise by weighting observations according to their noise. This is particularly important for the analysis of archival data which include observations taken under different weather conditions. Finally, only the matrix inversion technique allows for the inclusion of chopped observations in both the form of scan and jiggle maps[3].

The resulting map is calculated as a projection onto a tangent plane fixed by the centre of the map (the size of the map means that curvature effects are small but not negligible at the map edges). The map has a pixel size of $6''$, set by the sampling rate (discussed earlier) and an intrinsic beamsize of $14''$ FWHM as set by the telescope. In order to remove pixel-to-pixel noise which interferes with the ability to properly identify clumps, the map was convolved with a $\sigma = 6''$ Gaussian (FWHM = $14.1''$), producing an effective beam with a FWHM of $19.9''$.

Structure on scales several times larger than the chop throw ($>120''$) may be an artifact of the image reconstruction (this is independent of the reconstruction

---

[3] Jiggle maps are $\sim 2.3'$ in diameter and are observed by moving the telescope in a small 'jiggle' pattern to fill in the gaps between the bolometers (similar to dithering) while switching the secondary mirror between the region and two empty regions on opposite sides (three-point chopping). The 'jiggle' motion of the telescope is independent of the secondary three-point chop.

technique Johnstone et al. 2000a), and thus should also be removed from the map. We first tried a simple ‘flattening’ technique whereby the small-scale-smoothed map of above had subtracted from it a version of itself smoothed on a scale several times the chop throw. The large-scale-smoothed image represents the large scale structure. We created the large-scale-smoothed image through convolution with a Gaussian of $\sigma = 90''$ (FWHM = $212''$). This technique suffers from oversubtraction of flux around bright sources, producing negative “bowls”. In order to minimize this effect, we redid the flattening procedure. We first replaced all pixels in the original (small-scale-smoothed) map with values of $> |5|$ times the mean noise per pixel with specifically +5 or -5 times the mean noise prior to convolution, and then convolved with the same Gaussian as above. This ensures that less negative ‘bowling’ occurs but that all noise in regions of large scale structure are still smoothed and subtracted.

Since various portions of the map were observed under different weather conditions and depths, the noise across the final map is not uniform, although it typically varies by only a factor of less than five. The mean and rms standard deviation are ~8 mJy/bm and ~7 mJy/bm respectively. The resulting map is shown in Fig. 2.1, with close-ups in Figures 2.2 and 2.3.

2.2 Extinction

Dust grains along the line of sight have the effect of both dimming and reddening starlight passing through. Both of these properties have been used to determine the total dust column density along the line of sight. The dust column density is then converted to total gas plus dust column density assuming a constant gas to dust ratio (typically 100). Dimming has been used in the context of star counts, the premise being that a larger column of dust grains will lead to fewer of the stars behind a region being visible. To calculate the column density, observations of a control region are needed to characterize the distribution of luminosities for unextincted stars. Background stars are assumed to follow an approximately uniform spatial distribution. In the extincted region, the area covered by a fixed number of stars is compared to the control field to determine the extinction over that region. The resolution of the calculated dust column density map is variable. Regions of low dust column density have larger numbers of stars visible, and thus the column density can be well determined over small angular scale. In regions of high dust column density, few stars are visible, and thus a much larger angular region must be averaged over in the determination of extinction. This method for determination of column density/extinction was used by Cambrésy (1999), for example.

The second method utilizes the reddening caused by dust. Typical colours for stars are measured and compared with those behind a region containing the dust, and the difference in colours between the groups is used to determine the amount of reddening. This method is particularly effective at longer wavelengths (eg the infrared) where reddening and extinction are less severe, so that a greater number of stars can be used in the analysis. This technique, known as Near Infrared Colour Excess (NICE) is described in more detail in Lada et al. (1994).

The extinction data used here were derived from the Two Micron All Sky Survey (2MASS) stellar reddening data by Alves et al. (2005) as a part of the COMPLETE Survey, using a variation of the NICE technique - NICE Revisited (NICER), as outlined in Lombardi & Alves (2001). The NICER technique expands on that of NICE through optimizing the dust column density determination through the measure of reddening in more than one colour (i.e., using observations in at least three bands), as well as other procedures to optimize the data.

Inclusion of foreground stars in the dust density calculation is a major concern in both the NICE and NICER techniques. If foreground stars are not separated from the background sources for the extinction calculation, the extinction calculated will be too low. This would also impact the morphology observed for the cloud. As long as most stars in a patch of the sky are located behind the source of extinction, then foreground stars can be identified as sources that are significantly bluer than average. The NICER technique uses several different approaches to remove the effect of foreground stars in the calculation of extinction to determine the optimum method for each region. These approaches involve either the removal of stars with colours several standard deviations from the mean colour, or the weighting of each star according to its colour properties. Protostars embedded within the molecular cloud would also lead to a lowering of the calculated extinction. Protostars are more difficult to eliminate from the sample of background stars using any of the above techniques, and likely do lead to some error in a few regions of the extinction map.

A final point to consider in viewing the extinction maps is the resolution - the resolution of the Perseus extinction map is $\sim 2.5'$. Accurate determination of the extinction in a region requires measurements from many stars, hence without very deep infrared observations, the resolution is necessarily low.

Low resolution will smooth small scale structure in the map, diluting regions of high extinction. Very compact regions of high extinction can be missed entirely as there is an insufficient number of background stars observed to contribute signifiantly to the extinction calculation. Images from the Palomar sky survey (`http://archive.stsci.edu/cgi-bin/dss_form`) can be used to get a rough idea of the dust column density distribution at higher resolution, although the interpretation is complicated by effects such as emission from reflection nebulae. Visual comparison of the Palomar sky survey images and the calculated 2-MASS extinction map for Perseus suggests that parts of the extinction map are affected by the low resolution as discussed above.

The extinction data are denoted by contours overlaid on Figures 2.2 and 2.3.

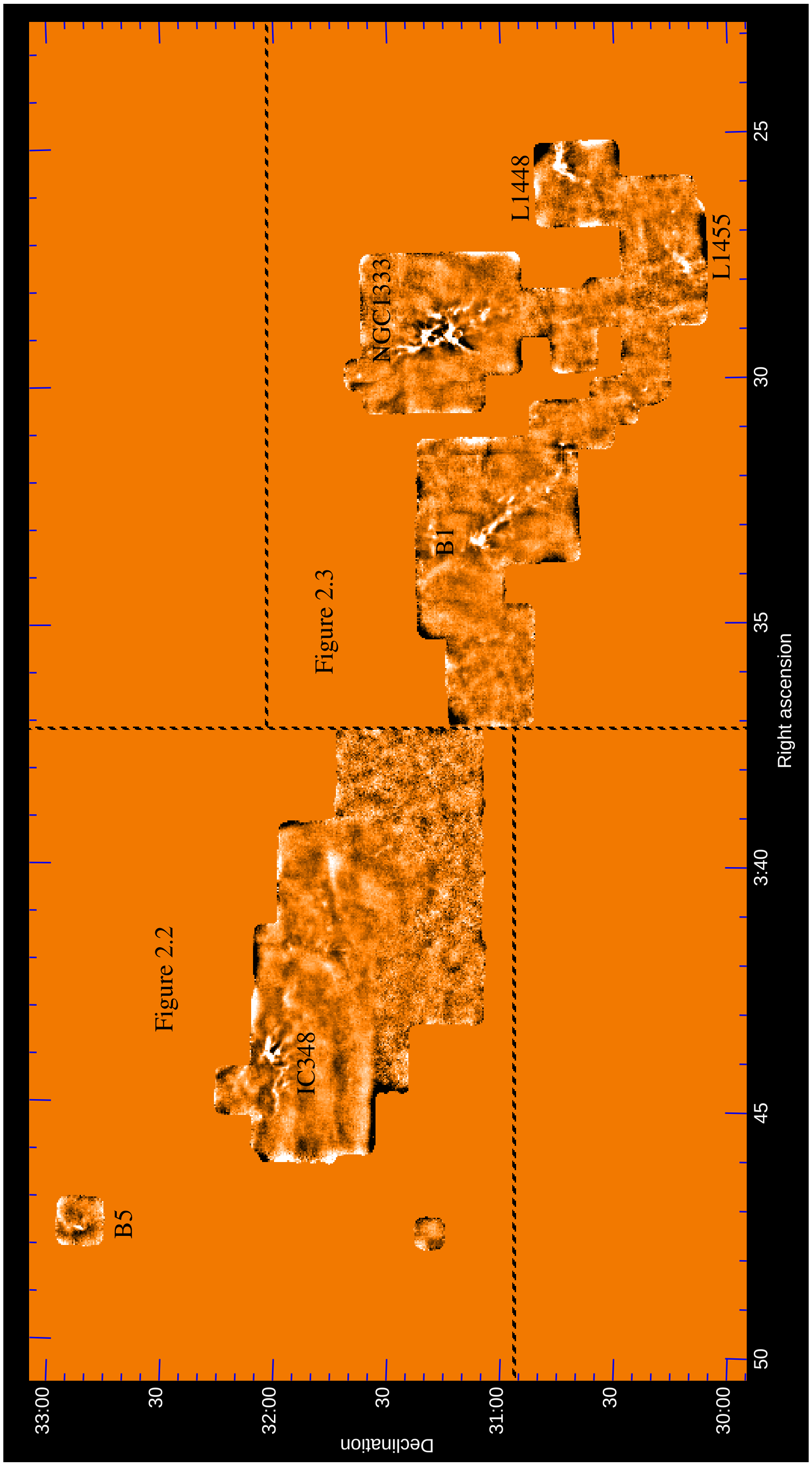

Figure 2.1: 850 μm observations of the Perseus molecular cloud. White regions correspond to a flux of ∼80 mJy/bm and black to ∼-50 mJy/bm. The dashes indicate the regions covered by the following two figures.

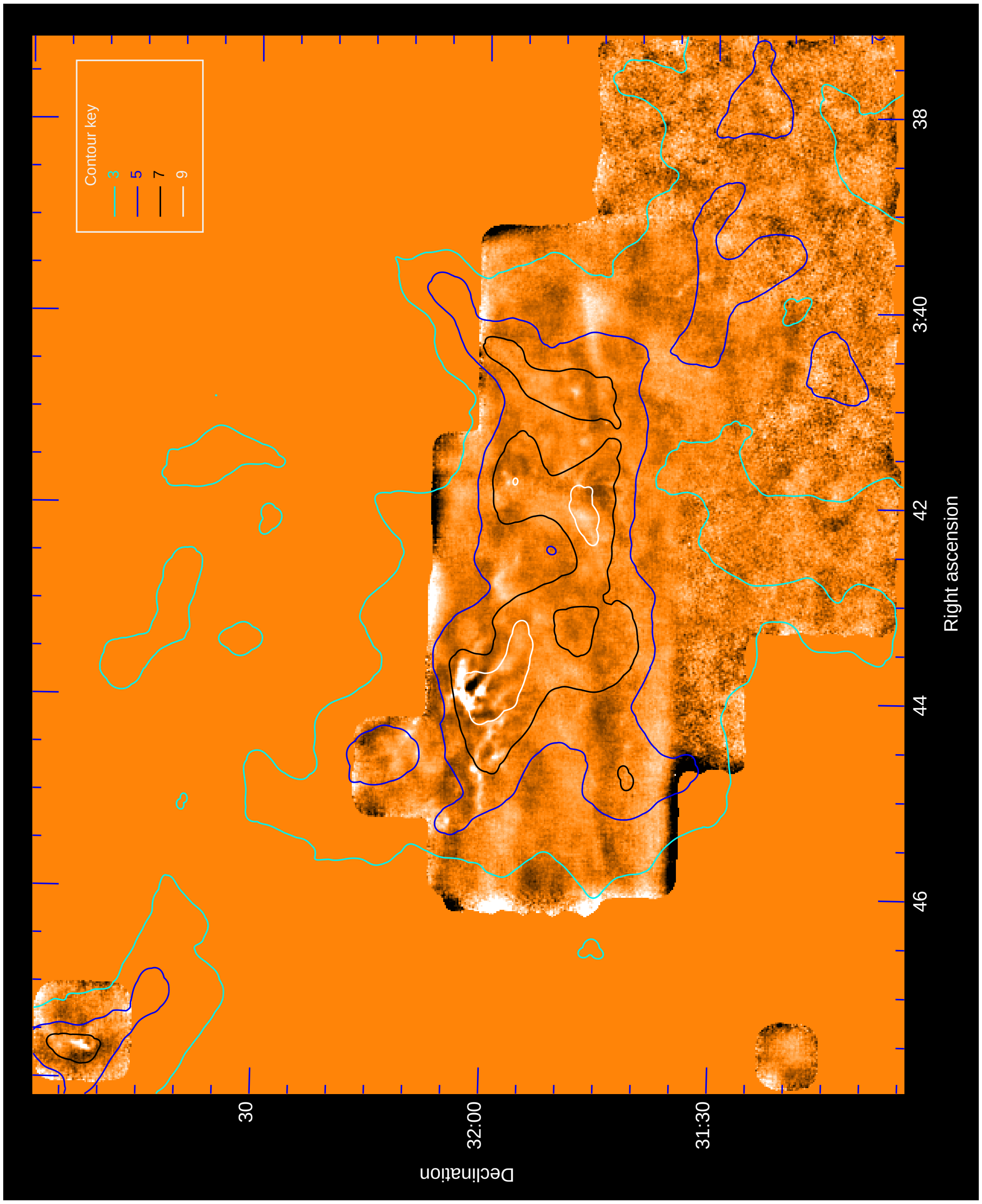

Figure 2.2: 850 μm observations of the eastern half of Perseus. White regions correspond to a flux of ~80 mJy/bm and black to ~-50 mJy/bm. Overlaid are contours denoting the extinction in magnitudes (from Alves et al. 2005, see text for further details).

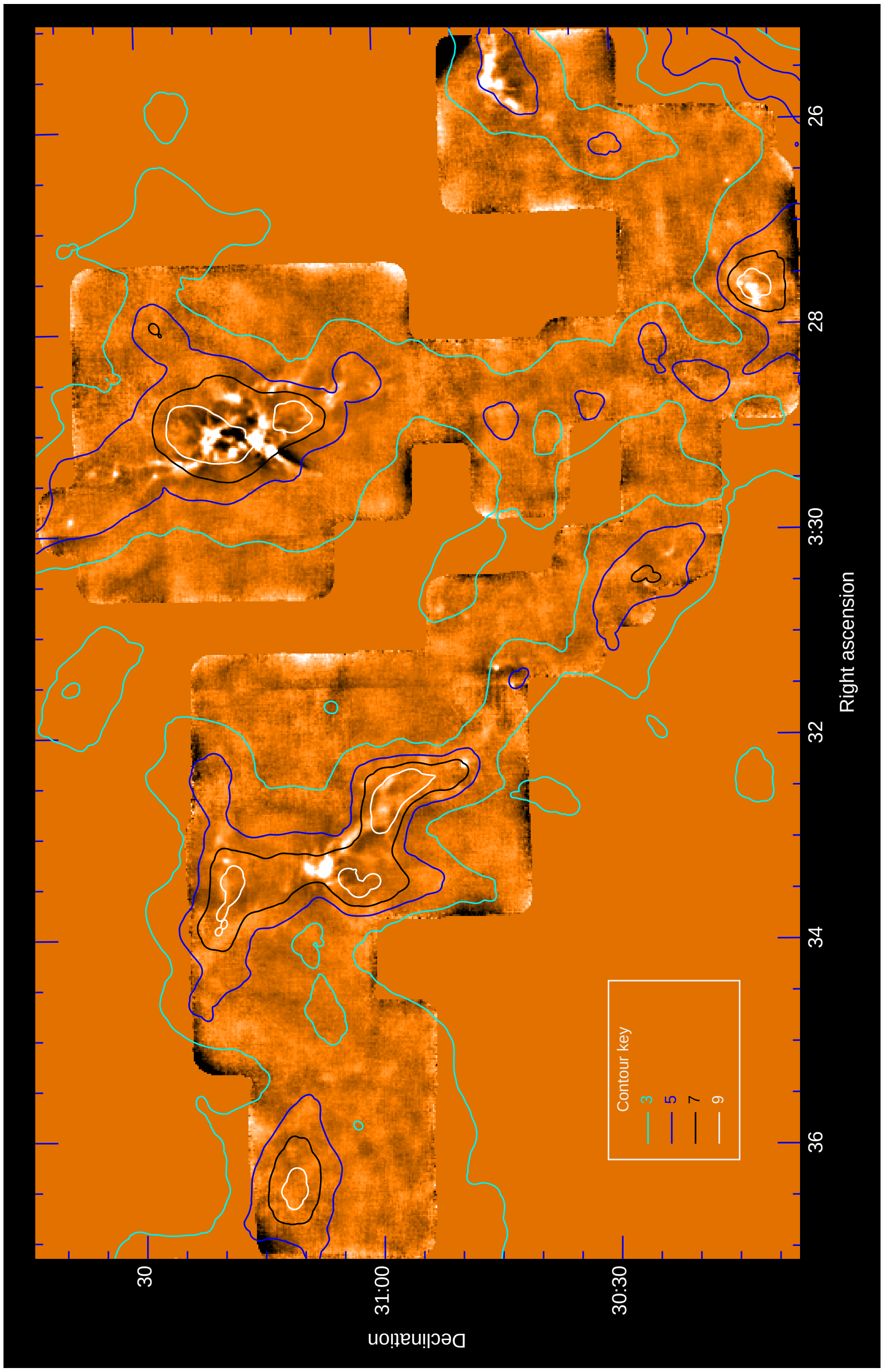

Figure 2.3: 850 μm observations of the western half of Perseus. White regions correspond to a flux of ~80 mJy/bm and black to ~-50 mJy/bm. Overlaid are contours denoting the extinction in magnitudes (from Alves et al. 2005, see text for further details).

Chapter 3

Identification and Analysis of Structure

As illustrated in Figures. 2.2 and 2.3, structure exists in both the submillimetre and extinction maps. Below we describe our identification of structure in each, followed by an analysis of the structure.

3.1 Structure Identification - Submillimetre Continuum

To identify structure in the 850 μm map, we used the automated routine Clumpfind (2D version; Williams, de Geus, & Blitz 1994). Some clump-identifying algorithms assume a pre-determined shape for the structure (typically Gaussian); however, Clumpfind has the advantage of not assuming a shape, which can lead to the artificial division of more complex objects. Clumpfind instead utilizes contours to determine clump boundaries. In particular, clumps are identified at local maxima every two σ_C[1] and extend until reaching a user-defined minimum flux value or encountering a minimum flux border with a second clump. Use of Clumpfind

---

[1] The user- defined contouring interval used in Clumpfind; typically the noise level in the map.

also allows for easier comparision with previous work (e.g., Johnstone et al. 2005; Reid & Wilson 2005; Johnstone, Di Francesco, & Kirk 2004; Johnstone et al. 2001, 2000b, etc.) which also use Clumpfind. Bulk clump properties such as the clump mass distribution have been shown to be similar to those found assuming a Gaussian profile for clumps (Johnstone et al. 2000b). Our map has a pixel size subsampling of the beam, thus the σ_C we use in Clumpfind is the mean standard deviation *per pixel.* We identify 57 submillimetre clumps down to a level of 3 σ_C, after removal of 64 spurious objects that were either smaller than the beam or noise spikes appearing in regions of higher than average noise (the vast majority of which occur at the map edges). Figures 3.1 and 3.2 illustrate where these clumps were found. Hatchell et al. (2005) have recently published a similar analysis on much of the same region of Perseus using a different method for the data reduction and the identification of clumps, and our analysis shows good agreement with their results. Hatchell et al. (2005)'s clumps tend to have slightly higher peak fluxes, as the final submillimetre map presented in that paper was neither flattened nor smoothed. Table 8.1 lists the properties of the clumps we identify, along with the corresponding designations from Hatchell et al..

The total flux of each clump can be converted into mass assuming that the dust is optically thin and emits thermally. Following Johnstone et al. (2000b), the conversion is

$$\mathrm{M_{clump}} = 0.38\ \mathrm{S_{850}} \left(\exp\left(\frac{17\ \mathrm{K}}{\mathrm{T_d}}\right) - 1\right) \left(\frac{\kappa_{850}}{0.02\ \mathrm{cm^2\ g^{-1}}}\right)^{-1} \left(\frac{\mathrm{D}}{320\ \mathrm{pc}}\right)^{2} \mathrm{M}_\odot \quad (3.1)$$

where $\mathrm{S_{850}}$ is the total flux at 850 μm, $\mathrm{T_d}$ is the dust temperature, κ_{850} is the dust opacity at 850 μm, and D is the distance. Following the SST c2d team (Evans et al. 2003) and Hatchell et al., we adopt a distance of 320 pc to the Perseus molecular cloud as found by de Zeeuw et al. (1999). We also take a typical internal temperature of 15 K and, following Johnstone et al. (2005), a dust opacity of $\kappa_{850} = 0.02\ \mathrm{cm^2\ g^{-1}}$. Therefore, the conversion factor between Jy and $\mathrm{M}_\odot$ is 0.8. Several of the constants adopted in the above equation are not precisely

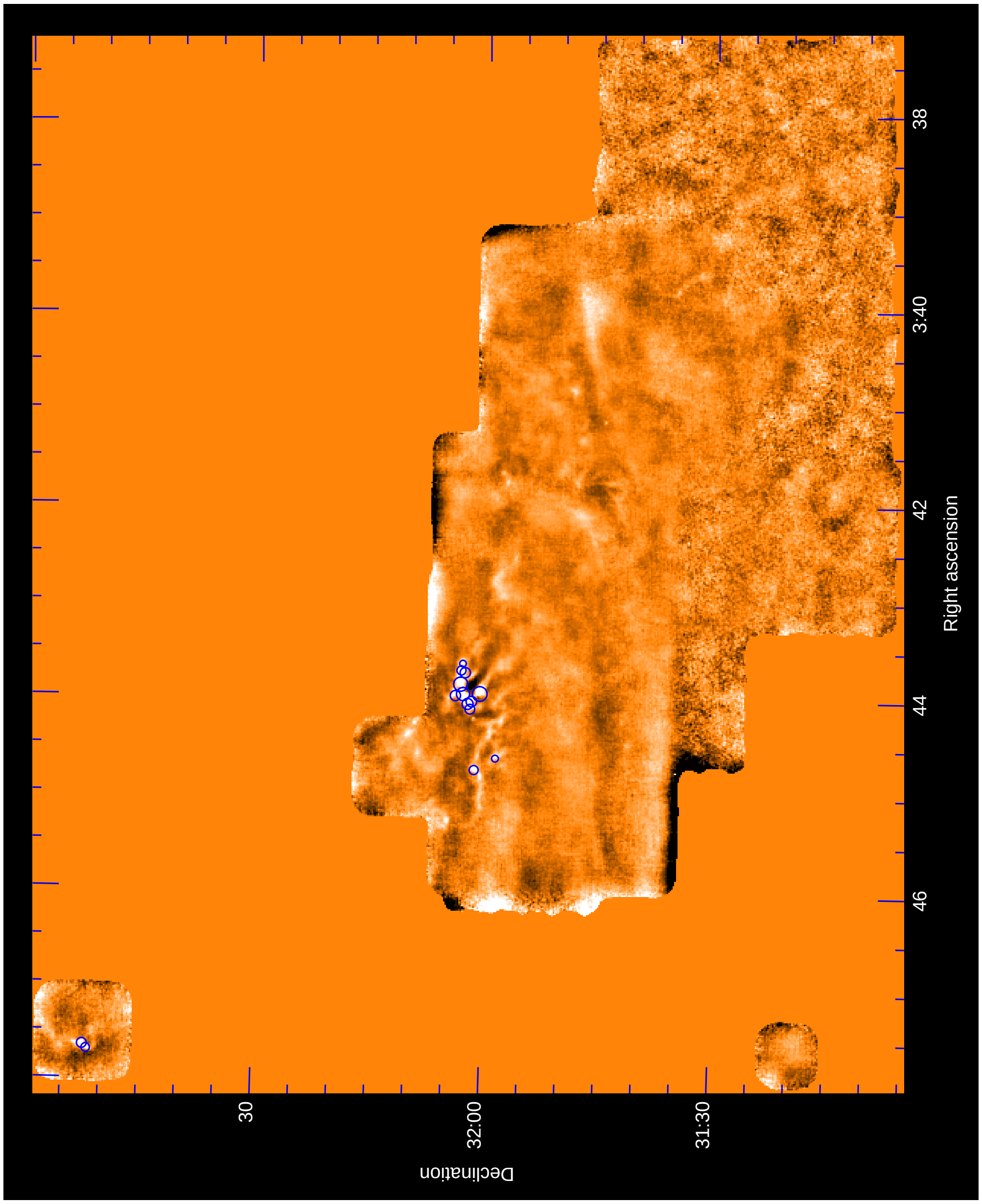

Figure 3.1: Eastern portion of 850 μm data of Perseus. The white represents a flux of ∼80 mJy/bm and black a flux of ∼-50mJy/bm. The blue circles denote the clumps identified by Clumpfind, with the radius being 1.5 times the mean radius found by Clumpfind.

known, leading to some uncertainty in this conversion factor. For example, the

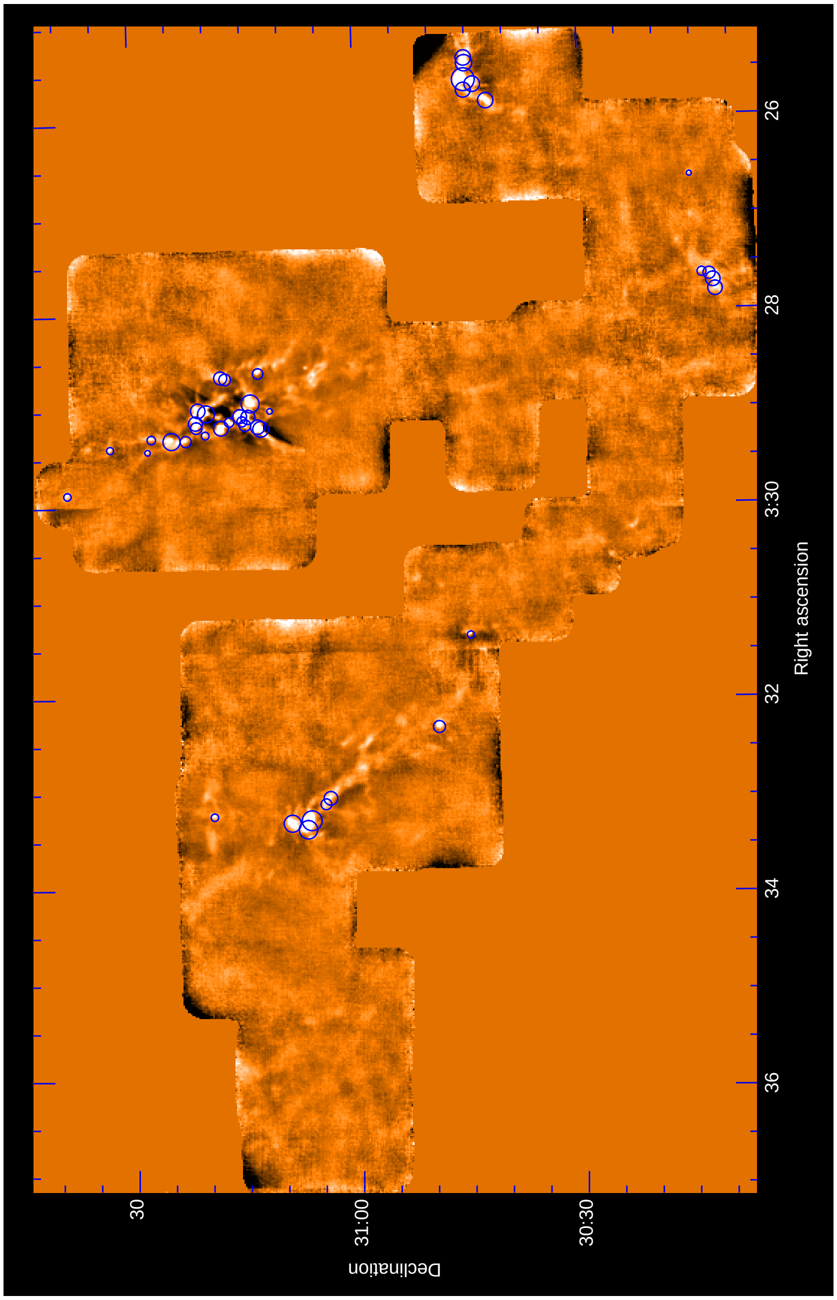

Figure 3.2: Western portion of 850 μm data of Perseus. The white represents a flux of ~80 mJy/bm and black a flux of ~-50mJy/bm. The blue circles denote the clumps identified by Clumpfind, with the radius being 1.5 times the mean radius found by Clumpfind.

distance to the Perseus molecular cloud has been argued to be anywhere from 220 pc (Cernis 1990) to 350 pc (Herbig & Jones 1983). The adopted opacity is also uncertain as it relies on knowledge of the composition of the dust grains (eg if they are ice covered). Hatchell et al. adopt a value of $\kappa_{850} = 0.012$ cm^{2}g^{-1}, which is within a factor of 2 of the value we use. The temperature is also not precisely constrained. Although the interiors of molecular clouds are known to be cold, a range of temperatures is still possible, especially for young protostars which may be heated through accretion, thus adopting a temperature several degrees cooler or warmer than 15 K is not unreasonable (Hatchell et al. assume a temperature of 12 K). The combination of these uncertainties in parameters results in the quoted mass being certain to a factor of two or three. The derived clump masses are also listed in Table 8.1. Analysis of these clumps is presented in the following section.

Using the effective clump radii found by Clumpfind, we can estimate the number density for each clump. This is found to range between $\sim 10^5$ cm^{-3} and 10^6 cm^{-3}, which yields temperatures of several tens of Kelvin being required for the clumps to be supported by thermal pressure alone (using the Jeans criteria). Since these temperatures are of the same order of magnitude as the 10 K of the cloud, we will return to analyze the submillimetre clumps as entities in hydrostatic equilibrium in Section 3.4.

3.2 Structure Identification - Extinction data

As is evident from Figures 2.2 and 2.3, the extinction data also appear to be 'clumped'. Examining the data by eye, it was clear that there are two types of 'clumping' in the extinction data. The smaller scale consists of compact objects, while the larger scale consists of groupings of the compact objects within a diffuse background. We term these two types of structures as cores and super cores. The extinction level in the diffuse regions of super cores is varied, hence we were not able to find a completely automated method for defining the structures. In order to be as unbiased as possible in the definition of the structures, we ran Clumpfind on the extinction map (using $\sigma_C = 1$ mag to prevent excessive subdivision of structure). Cores were defined through the subdivision by hand of several of the Clumpfind objects and the super cores were defined through the mergers of several Clumpfind objects. Figures 3.3 and 3.4 show the extinction map with outlines denoting these structures. It is important to note that the definition of the cores and super cores could be affected by any errors in the extinction map caused by embedded protostars. An artificial dip in the middle of a high extinction region could cause the division of this region into two cores, for example. Visual inspection of the map does not provide any obvious examples of this, but it is a possible source of error in the clump and super clump definitions.

Assuming a conversion factor of $N_H/A_V = 2 \times 10^{21}$ cm^{-2} and $\mu = 2.35$, we find the total mass in the extinction map is $\sim$50,000 M$_\odot$ ($\sim$17,000 M$_\odot$ in the region for which we have submillimetre data). Previous mapping in CO has resulted in smaller mass estimates, but only by a factor of a few - Bachiller & Cernicharo (1986) estimate 17,000 M$_\odot$ in mass over a 6.4 square degree area, while Carpenter (2000) estimates $\sim$ 13,000 M$_\odot$ from Padoan et al. (1999)'s observations. The difference between these two mass measures and ours could be at least partially accounted for by diffuse extinction permeating the region that CO observations likely miss — an A_V of one over our entire map region provides a mass of $\sim$22000 M$_\odot$. CO observations are insensitive to mass contained in the cloud's atomic surface layer, where CO is unlikely to form.

Our observations show individual super cores range in mass from $\sim$200 M$_\odot$ (for the more isolated regions) to $\sim$6,000 M$_\odot$ for the largest of the complexes. Table 8.2 and 8.3 show the properties of these structures. Using the mean radius (derived from the total areal coverage) to infer the total volume of each core, we find they have number densities of $\sim$10^5 cm^{-3} (see Table 8.2 and 8.3), and would require temperatures of several hundred Kelvin to be supported only by thermal presssure. The required temperatures for thermal support are much higher than

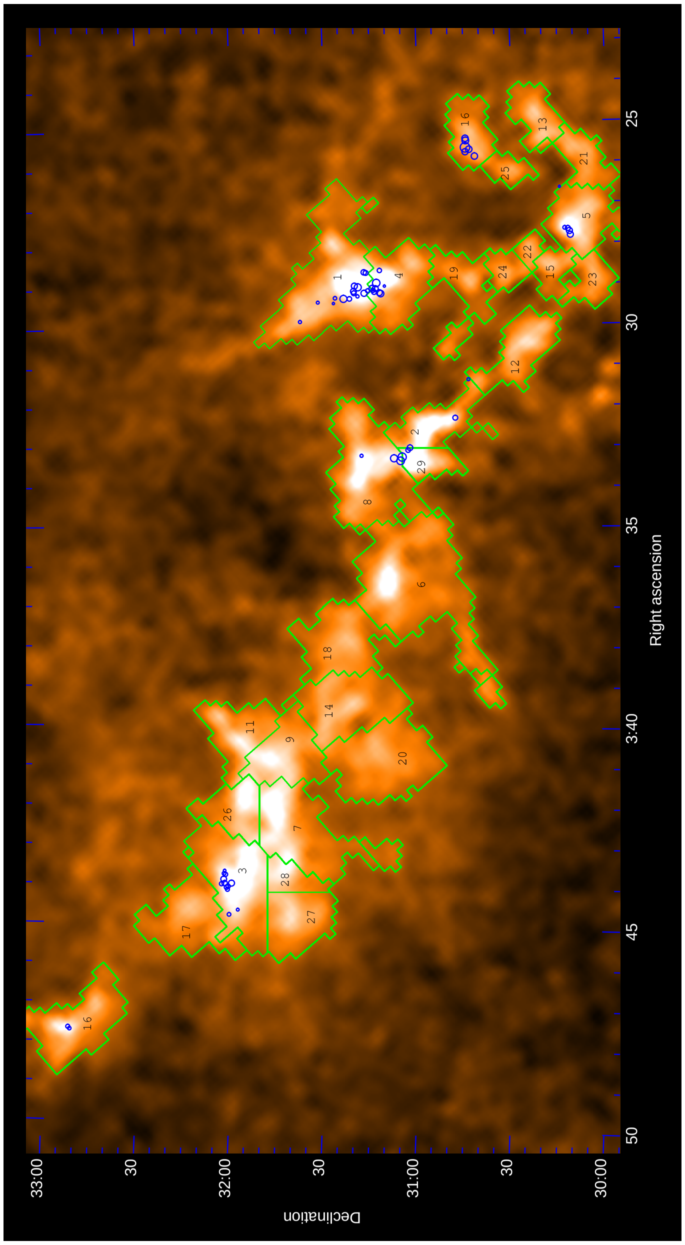

Figure 3.3: Division of extinction data (Alves et al. 2005) into 'cores'. White represents an extinction of ∼8 mags, while black is ∼1 mag. The green outlines denote extinction cores identified while the blue circles denote the submillimetre clumps (the circles have a radius of 1.5 times that found by Clumpfind).

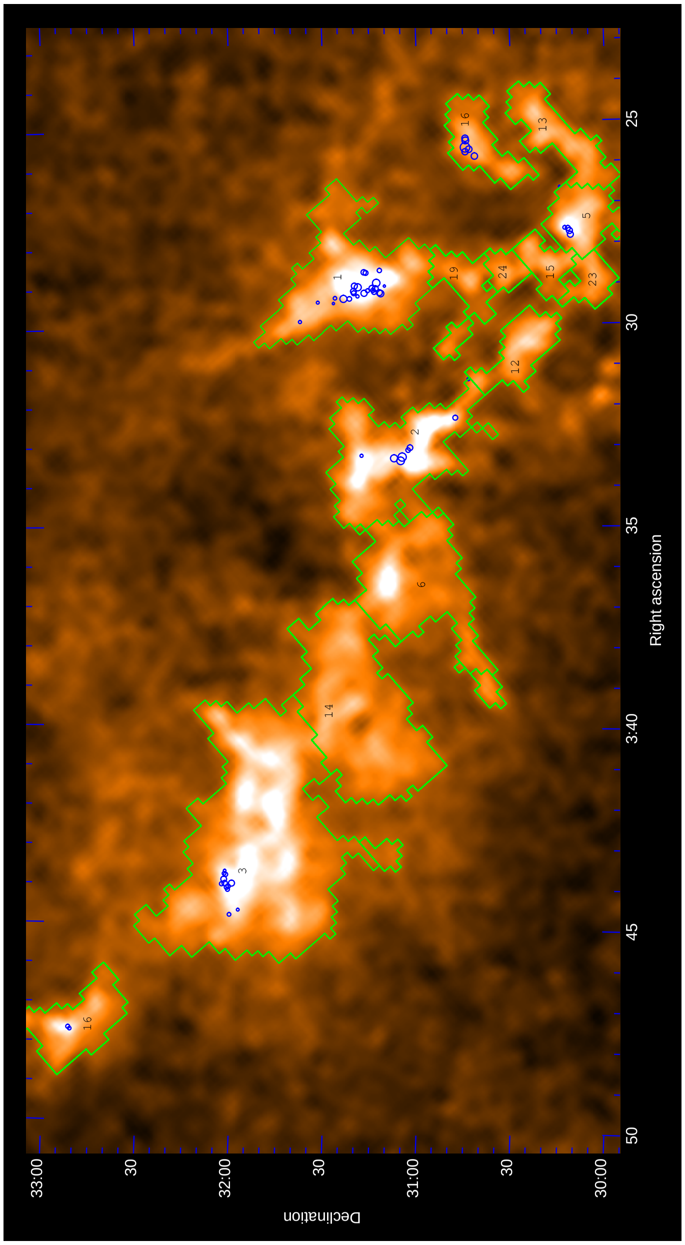

Figure 3.4: Division of extinction data (Alves et al. 2005) into ‘super cores’. White represents an extinction of ∼8 mags, while black is ∼1 mag. The green outlines denote extinction super cores identified while the blue circles denote the submillimetre clumps (the circles have a radius of 1.5 times that found by Clumpfind).

the ∼10 K temperature of the cloud, implying either significant sources of non-thermal support, or that the cores and supercores are not in equilibrium.

To analyze further the extinction cores, we note the extensive diffuse extinction within which these structures appear to lie. To gain a more accurate interpretation of these objects, we fit the cores with 2D Gaussians (using the publicly available IDL mpfit2d package by Craig Markwardt) and estimate the mass above the background level contained within each core, as well as estimate their typical size through their Gaussian sigma (see Appendix C). Table 8.2 also shows the resulting fit parameters. The super cores, as associations of cores, are not shaped regularly enough to be fit with Gaussians. The effect of using Gaussian fit parameters for only the extinction cores in subsequent analysis is discussed in the relevant sections below. The number densities for the exinction cores as calculated with the Gaussian fit properties are several times smaller, as are the temperatures required for only thermal support. The drop in density found with the Gaussian fit is due to the exclusion of the background column density. The temperatures found using the densities from Gaussian fitting are still ∼50 K or greater, and so the implications discussed above still apply.

3.3 Structure Analysis - Mass Distribution

The mass distribution of structure is a useful bulk property to quantify. This is usually expressed cumulatively, where N(M) is the number of objects with mass above M. This distribution can often be well fit by a power law or broken power law characterized by slope α, where $N(M) \propto M^{-\alpha}$. The distribution of masses that stars are formed with, the stellar initial mass function (IMF), was initially observed by Salpeter (1955) as having α of 1.35. This has been more recently modified to a broken power law with $\alpha \sim 1.3$ for masses above 0.5 $M_\odot$, and tending to a shallower slope of $\alpha \sim 0.3$ for lower masses (Kroupa 2002). The stellar IMF does not appear to vary with the region in which the stars formed [although the Taurus molecular cloud appears to have a much shallower slope; (e.g. Briceño et al 2002)]. Within molecular clouds, CO observations on large scales have revealed a mass distribution where the bulk of the mass is contained in the most massive structures, with α between 0.6 and 0.8 (Kramer et al. 1998). Structures observed in the submillimetre continuum, on the other hand, tend to have a mass distribution where most of the mass is contained in the least massive objects. Other (sub)millimetre observations of other starforming regions show a clump mass distribution that can be fitted by a broken power law with the high mass end characterized by a slope α similar to that of the stellar IMF and displaying a turn-over at some mass to a shallower power law; for example, see Motte et al. (1998), Johnstone et al. (2000b), Johnstone et al. (2001), Johnstone et al. (2005) for clump mass distributions in the Ophiuchus and Orion B molecular clouds. The turnover location is probably not physically meaningful as it occurs where incompleteness in the clump sample likely becomes significant. While observations show the slope of the high mass end of the mass distribution has small variations between regions, there does not appear to be a systematic trend with environmental variables such as metallicity. Many theories exist as to why the clump mass function appears to be so uniform over different regions including turbulent fragmentation (e.g., Padoan & Nordlund 2004), competitive accretion (e.g., Bonnell 2005) and thermal fragmentation (e.g., Larson 2005). Some theories predict that small variations in the clump mass distribution are possible in individual regions due to small number statistics for any given region, especially as it applies to the formation of the rarer massive objects which affects the formation of the less massive objects; (Padoan & Nordlund 2004). This may account for the scatter in slopes of clump mass distributions observed of different molecular clouds.

The similarity between the roughly invariant clump mass function and the invariant stellar IMF is suggestive of a direct link between the two. There are, however, several concerns with this idea. The total submillimetre clump mass often exceeds that expected to be in the final stars (see Larson 2005, for a review).

This difference might be acounted for through inefficient star formation (e.g., if all clumps lost some percentage of the clump mass reservoir to outflows during formation). A second problem is that there is no evidence that all clumps do form stars. In the turbulent support framework, a significant number of clumps in fact re-expand (e.g., Vázquez-Semadeni et al. 2005).

The difference between the large and small scale mass distributions is also a puzzle. It may be due to different methods of observations in the definition of structure, or chemistry effects (CO is affected by freeze-out), or possibly to real differences in the structures at the large and small scales due to the different physical processes that are responsible for fragmentation.

3.3.1 Submillimetre Continuum

The submillimetre clumps we identify in Perseus have a broken power law mass distribution, similar to those found in other star-forming regions (see Figure 3.5). The slope at the high mass end is slightly steeper than is typically found, with $\alpha \sim 2 \pm 0.1$ using clump masses calculated using a temperature of 15 K (solid line). The dashed line shows the mass distribution calculated using a Bonnor-Ebert model temperature fit to each clump (see the following section for a discussion on Bonnor-Ebert modelling). The mass distribution using the BE temperatures has a much steeper slope at the high mass end with $\alpha \sim 3.7 \pm 0.5$. Observations in other molecular clouds have found high mass slopes varying from $\alpha \sim 1 - 1.5$ (Johnstone et al. 2000b) to $\alpha \sim 2$ (Reid & Wilson 2005) and thus our results using T=15 K do lie within the range found by previous authors. The mass distribution we estimate using T=T_{BE} is too steep to fall within this range and it is unlikely that such a large difference could be explained by statistical variation. The difference in the slopes of the T = 15 K and T_{BE} mass distributions in our plots is caused by the higher BE temperatures (hence lower masses for a given flux) adopted for the highest flux clumps in our sample. (This trend is illustrated in Figure 3.11 and discussed in more detail in the following section.) We argue that the T=15 K mass distribution is the more reliable one to use.

We find that the mass distribution at the low mass end has $\alpha \sim 0.4 \pm 0.1$, with the turn-over between the high and low mass regimes occuring around 0.7 $M_\odot$, approximately where our sample may suffer from incompleteness. New clumps were identified through Clumpfind down to a peak of 5 σ_C and allowed to extend to the 3 σ_C level, thus we expect to miss clumps peaking around the $3-5\sigma_C$ level. Taking a 'typical' clump extent of 1800 sq. arcsec or 0.5 sq. arcmin (although the largest extend over 2.0 sq. arcmin), we find clumps of masses ∼0.5 to 0.9 $M_\odot$ would be missed. Therefore we judge our sample to be incomplete around this level. This incompleteness level is higher than by Hatchell et al.'s analysis. Our 1.3 sq. deg of fast-scan observations (not included in Hatchell et al.) have a higher noise level than the public archival data analyzed in both papers. To avoid identifying too many artificial clumps in the our composite map, we set our Clumpfind threshold higher than that which would be required using only the archival data analyzed by Hatchell et al.. We wished to keep our analysis of the entire region uniform, hence we did not apply different Clumpfind search thresholds in regions of lower noise.

3.3.2 Extinction

We also examined the mass distributions of the extinction cores and super cores (see Figure 3.6). Recall that unlike the submillimetre data, the extinction data is not chopped, and hence have sensitivity to large scale structure. The extinction cores have a similar mass distribution to the submillimetre clumps, with slopes of $\alpha \sim 1.8 \pm 0.2$ and 0.2 ± 0.05 at the high and low mass ends respectively, and a turnover at ∼120 $M_\odot$. However, the associations of cores (or super cores), have a much shallower mass distribution similar to that seen in CO, with a slope of $\alpha = 0.8 \pm 0.2$. The small numbers of cores and super core leads to a greater uncertainty in the derived slopes. Incompleteness is difficult to quantify accurately for the extinction data, given the modifications to the Clumpfind results (and Gaussian-fit mass estimates) but a rough estimate would be 100 $M_\odot$, using the

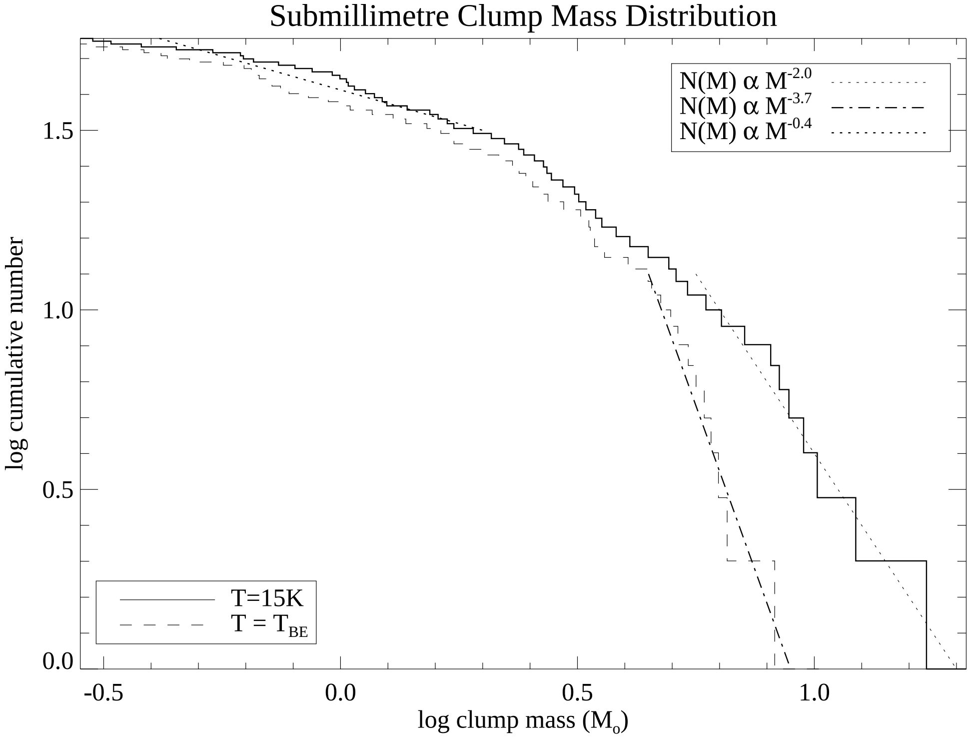

Figure 3.5: Cumulative mass distribution of the submillimetre clumps showing mass estimates using both a constant (T = 15 K) and Bonnor-Ebert model fit temperature.

same argument as in the previous subsection and taking a typical core area of 3,500,000$''^2$ ($10^{3/2}$).

The change in behaviour of the extinction core and super core mass distributions and their close correspondence to the two regimes previously observed in the submillimetre and CO is intriguing. Given the final by-hand definitions of both sets of objects, it is possible that the differences are a result of some bias that we introduced through these definitions. Figure 3.6 shows the Gaussian-fit masses for the extinction cores and the Clumpfind masses for the super cores. These different mass measures do not affect the findings — a similar distribution (at slightly higher masses) is found using the Clumpfind masses for the extinction cores. Projection effects may also play a role in the mass distribution measured: most of the cores and super cores are bounded by similar objects (unlike the submillimetre

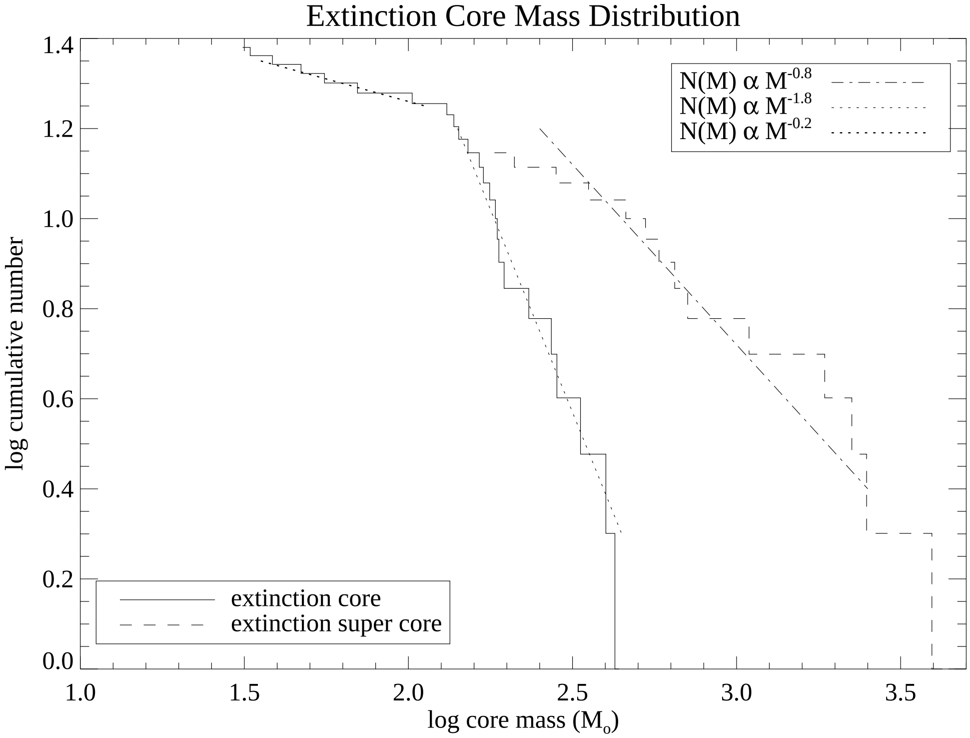

Figure 3.6: Cumulative mass distribution for extinction cores and super cores. The super cores are well fit by a single power law with a shallow slope, while the cores require a steep slope at the high mass end.

clumps), making the likelihood of overlap for the real 3D objects probable. This may have a greater effect on the super cores which are less regularly shaped and larger. Overlap would lead to larger numbers of massive objects (i.e., a shallower slope). With the above caveats on the derived mass distributions, if the slopes are truly different for the cores and super cores, this may be an indication of the scale over which fragmentation changes from a top -eavy to bottom-heavy mass function due to the importance of different physical processes.

3.4 Structure Analysis - Bonnor-Ebert fits

To gain physical insight, we model the submillimetre clumps as Bonnor-Ebert (BE) spheres - spherically symmetric structures that are isothermal, of finite extent, and bounded by an external pressure, where gravity is balanced by thermal pressure (Bonnor 1956; Ebert 1955; Hartmann 1998). Previous work (e.g., Alves et al. 2001; Johnstone et al. 2000b, 2001, 2005) has shown that submillimetre clumps can be well fit by a BE sphere model. Each BE sphere is dimensionalized by three parameters: the central density, external pressure, and temperature, which can be extracted from the best fit.

Recent work has shown that caution is needed in the interpretation of the fit to a BE sphere model, as dynamic entities produced in turbulent simulations can mimic the column density profile of a stable BE sphere (Ballesteros-Paredes et al. 2003). Ballesteros-Paredes et al. (2003) used data from numerical simulations of turbulent star formation to generate column density observations of the clumps formed. They demonstrate that many (65%) of the clumps identified in the simulations have radially averaged column density profiles that can be fit to a BE model, with 47% of these corresponding to stable configurations. Nevertheless, all of the clumps in the simulation either collapse into sink particles (where the simulation can no longer follow the evolution into a protostar) or re-expand into the surroundings again. The range of best fit physical parameters derived from the modelling (temperature, central column density, and external pressure) were similar to those found in the BE modelling of observed clumps although there was no good correlation between the 'true' simulation values and those found by the BE modelling. For example, the simulations were isothemal with T=11.3 K, while the BE model temperatures ranged from 5 to 60 K.

Differentiation between physical scenarios is most easily resolved through velocity information (Myers 2005), however, even this may not be enough to guarantee an accurate prediction of quasi-static equilibrium. Klessen et al. (2005) analyzed the velocity dispersions of the same cores examined in Ballesteros-Paredes et al. (2003) and showed that a significant fraction do not show signs of turbulence. Roughly half were found to be ‘coherent’ (the velocity dispersion remains roughly constant in different regions of the clump) and of these, 40% showed subsonic linewidths (with only 20% possessing significant non-thermal line widths). Clumps formed in turbulent simulations often have subsonic linewidths at their centres due to the formation mechanism of the clump - the flows are roughly stationary at the point of convergence. The origin of the coherence is less clear, although Klessen et al. (2005) speculated that the result may be due to density-weighting in the velocity observations. The densest (most quiescent) material contributes to the majority of the signal, leading to little change in the velocity dispersion across the region. Alternatively, until the pressure wave generated by the converging flows subsides, it is possible that the clumps are well represented by the BE sphere type of model since the continued evolution to either collapse or re-expansion occurs after this pressure wave has dissipated. Even with all of the caveats above, BE models are useful in illustrating the minimum level of support that would be necessary to prevent collapse in an object of a given mass bounded by a finite pressure.

The density profile of a Bonnor-Ebert sphere is obtained through the solution of the Emden equation (Hartmann 1998),

$$\frac{1}{\xi^2}\,\frac{\mathrm{d}}{\mathrm{d}\xi}\,\xi^2\,\frac{\mathrm{du}}{\mathrm{d}\xi} = \mathrm{e}^{-\mathrm{u}} \tag{3.2}$$

where u is the dimensionless density [u = -ln(ρ/ρ_c) and ρ_c is the central density] and ξ is the dimensionless radial measure ($\xi = r\sqrt{4\pi G\rho_c/c_s^2}$). We solve the Emden equation using a fourth-order Runge-Kutta routine (Press et al 1992) Bonnor-Ebert spheres are characterized by a one-dimensional radial density profile, with different truncation radii defining a particular family of models (see Figure 3.7). Each member of a family of models is identical up to a scaling factor, thus all family members share a dimensionless truncation radius and density profile shape but can have different values for the central density. Each family of Bonnor-Ebert spheres possesses a unique importance of self gravity. The importance of self-gravity can be parameterized by $\lambda = \rho_c/\rho_{edge}$, where ρ is the density. Clumps with $\lambda > 14$ are unstable (Hartmann 1998). The importance of self-gravity can also be thought of in terms of the central concentration of a clump - a higher concentration corresponds to a higher importance of self-gravity. Each concentration therefore alternatively defines a unique family of BE spheres (see Fig. 3.8). Following Johnstone et al. (2000b), we define the concentration to be

$$\mathrm{C} = 1 - \frac{\mathrm{S}_{850}}{(\pi \mathrm{R}_{\mathrm{eff}}^2)\,\mathrm{f}_0} \tag{3.3}$$

where C is the concentration, S_{850} the total flux, $\mathrm{R}_{\mathrm{eff}}$ the effective radius, and f_0 the peak flux. Table 8.1 also lists the concentrations for each clump. The concentrations are approximate due to the relatively large size of the beam compared with the clump radius. Non-spherical shapes of the clumps can also have an effect on the observed concentrations; Ballesteros-Paredes et al. (2003) demonstrated that non-spherical clumps appear to have different concentrations in different projections. To be fit by the Bonnor-Ebert sphere model, the concentration must be greater than 0.33 (corresponding to a uniform density sphere) and less than 0.72 (no stable model exists at concentrations above this; see Hartmann 1998). These regimes are also marked on Figs 3.7 and 3.8. To be stable from collapse, clumps with concentrations above 0.72 require additional support mechanisms (for example, pressure from magnetic fields). Alternatively, these high concentration clumps may be more evolved and already experiencing collapse. Walawender et al. (2005) analyzed multiwavelength data in the B1 core of Perseus and found that all clumps with concentrations above 0.75 contained protostars, while none of those at low concentrations (< 0.4) and few at the intermediate concentrations did. (See Appendix B for this multi-wavelength analysis.) Concentration thus appears to be a good indicator of source evolution.

We use the concentration to fit the clumps to stable Bonnor-Ebert spheres (using the closest stable concentration for clumps where necessary) following Johnstone et al. (2005), again adopting a distance of 320 pc and an opacity of 0.02

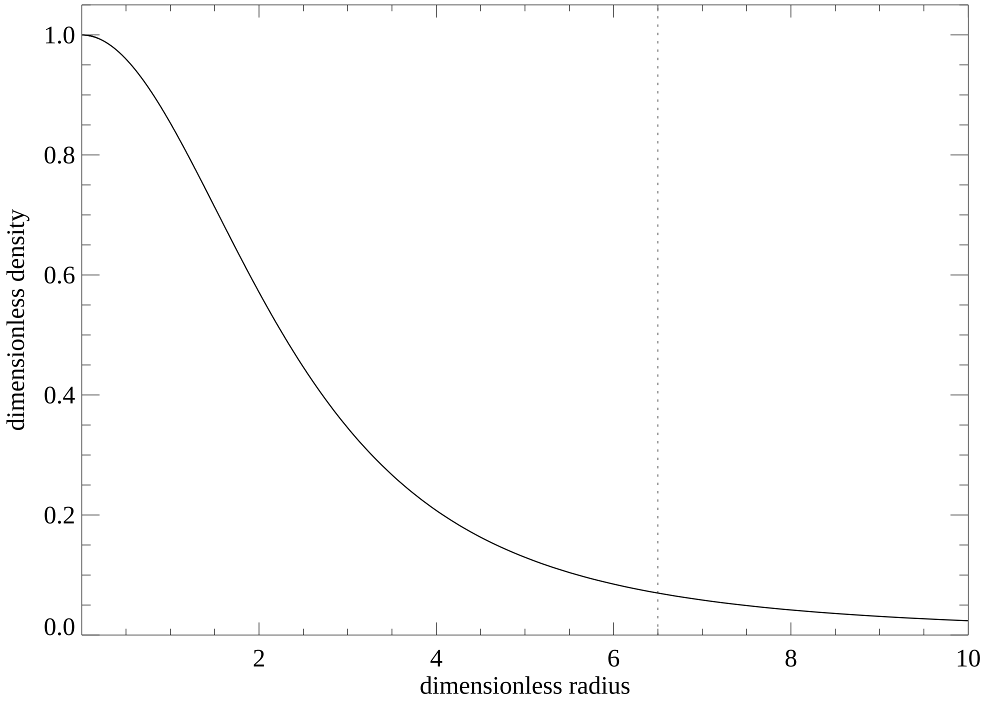

Figure 3.7: Bonnor-Ebert model profile — density (dimensionless) as a function of radius (dimensionless). Dotted line denotes the boundary between the stable (left) and unstable (right) regimes.

cm^2 g^{-1}. Non-thermal support may exist in the clumps. Goodman et al. (1998) find in their survey of prestellar cores that thermal and non-thermal support levels are roughly comparable. Following Johnstone et al. (2005), we assume an equal level of thermal and non-thermal support. Comparable levels of thermal and non-thermal support may not be the case everywhere, however. Tafalla et al. (2004) show that non-thermal support is negligible in the cores in the quiescent star-forming region Taurus. A lower level of non-thermal support would increase our best-fit temperatures. We find temperatures ranging from 13 to 25 K and external pressures within $5.5 \leq \log_{10}(P/k) \leq 6.2$ (see Table 8.1). Figures 3.9 and 3.10 also show these results. The asterisks denote clumps whose the concentration was outside the stable range, requiring fits using the closest stable value. The physi-

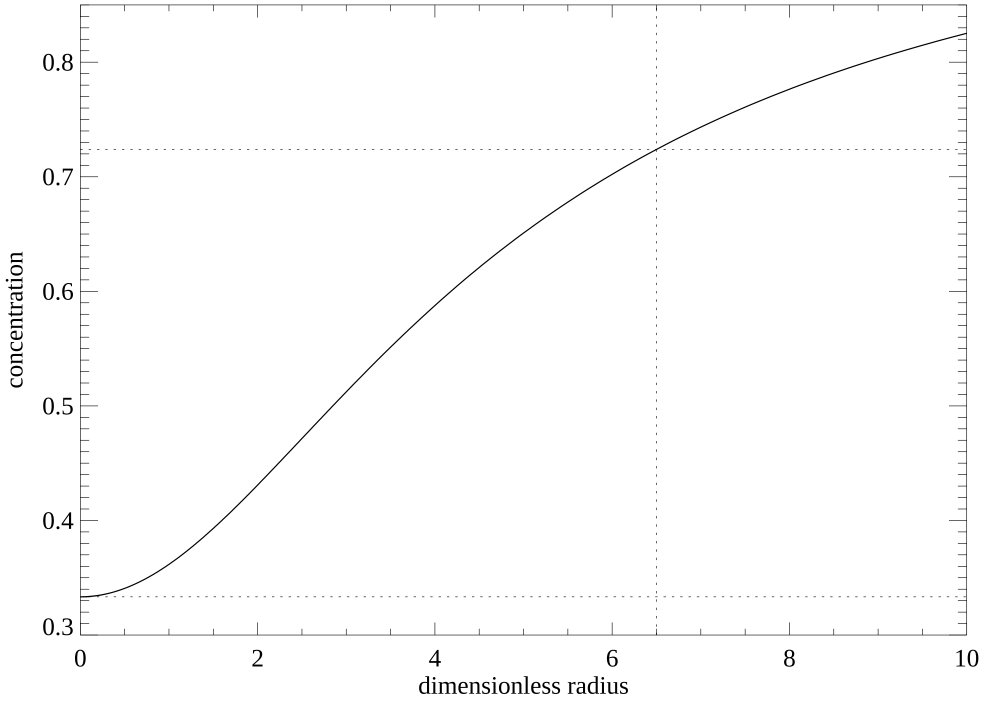

Figure 3.8: Bonnor-Ebert model profile — concentration as a function of radius (dimensionless). Dotted lines indicate boundary between stable and unstable regimes. Stable BE spheres must have concentrations between 0.33 and 0.72 (horizontal lines), corresponding to a maximum dimensionless truncation radius of 6.5 (vertical line).

cal properties (temperature, external pressure and central density) found for these clumps are thus less reliable, explaining why these clumps possess extremal values of temperature, external pressure, and central density more frequently than the other clumps (although none of the fit values fall outside of the range reasonably expected for the local clump environment).

The pressure due to the material in the molecular cloud can be written as $\mathrm{P/k = 1.7 \times 10^4 \overline{A}_V A_V\ cm^{-3}\ K}$, where the mean extinction is ~2 mag (see Section 4.1 for the derivation of this formula). The mean pressure in the molecular cloud is thus $\log_{10}(\mathrm{P/k}) \approx 4.9$. The highest extinction in the cloud is 11.8 mag, corresponding to a central pressure in the cloud due to the surrounding cloud ma-

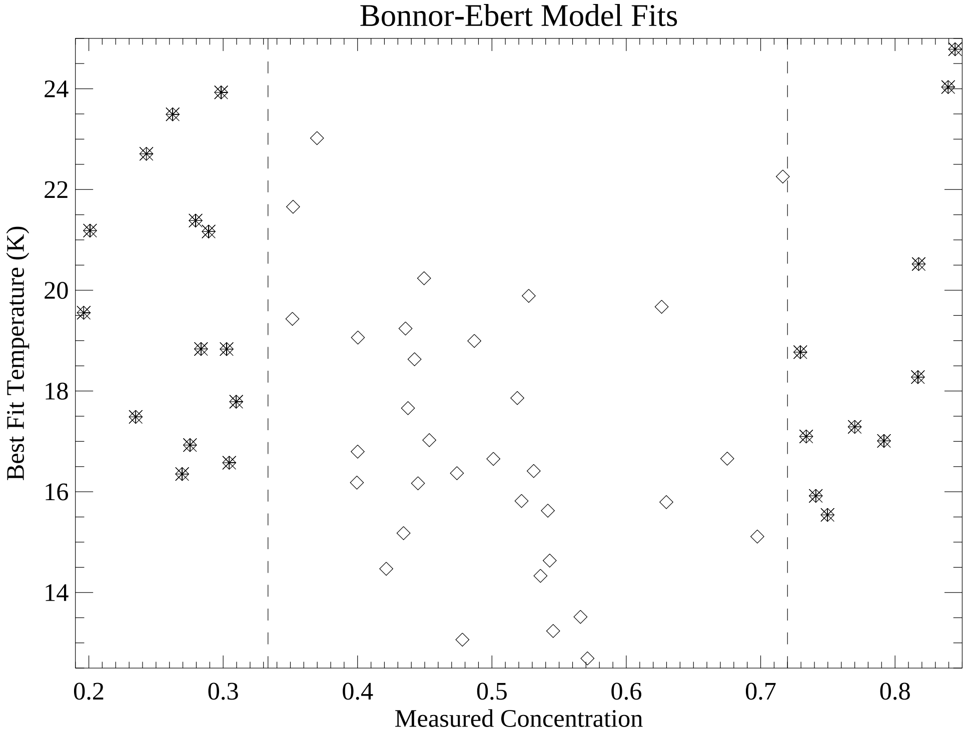

Figure 3.9: Results of the Bonnor-Ebert sphere modelling of submillimetre clumps — best fit temperature versus measured concentration. Clumps outside of the region indicated by the dashed lines cannot be fit by a stable BE sphere. See text for details.

terial of $\log_{10}(P/k) \approx 5.6$. Higher pressures can be generated by the extra weight of material in large cores with local mean extinctions higher than 2.2 mag. This demonstrates that the external pressures calculated with the BE model are reasonable, as they are in the range in which the cloud and extinction cores would supply. The pressures found from the BE modelling here are lower than those found by Johnstone et al. (2000b) in the Ophiuchus molecular cloud (they found $6 \quad \leq \log_{10}(P/k) \leq 7$), which is consistent with the findings here, as the total column densities (or extinctions) found in Ophiuchus are much larger. Johnstone, Di Francesco, & Kirk (2004) found a mean extinction of 4 mag and a peak extinction of 35 mag, implying the clumps there formed in a higher pressure environment than those we observe in the Perseus molecular cloud.

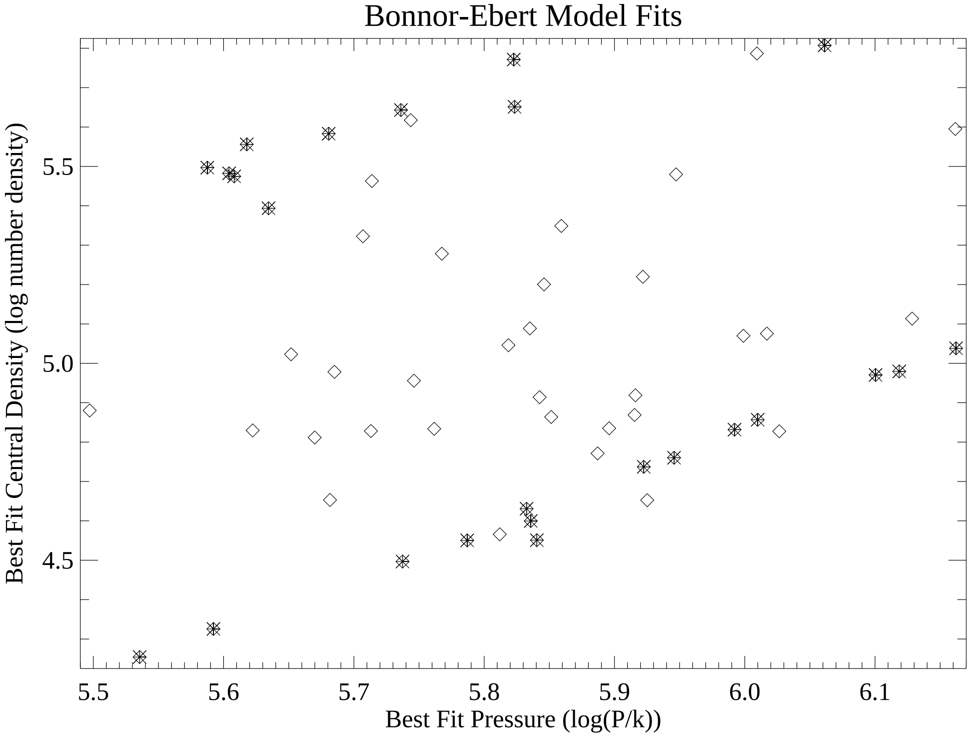

Figure 3.10: Results of the Bonnor-Ebert sphere modelling of submillimetre clumps — best fit pressure and central density. Asterisks denote clumps that have concentrations outside the range fit by a stable BE sphere model.

Using the temperatures derived from the Bonnor-Ebert fits, we can get a second estimate of the clump masses (also in Table 8.1). Figure 3.5 also shows the clump mass distribution using these values. As discussed in Section 3.3.1, the slope derived for the clump mass distribution function is much steeper using this temperature estimate than if a uniform clump temperature of 15 K is assumed.

Figure 3.11 shows the relation between clump flux and BE model temperature, demonstrating that the highest flux clumps (which almost exclusively have concentrations above the maximum stable value) have high derived temperatures. This may be a consequence of these objects being more evolved (see earlier discussion). The preference of higher temperatures for the largest flux objects has the consequence of steepening the cumulative mass distribution at the high end, as

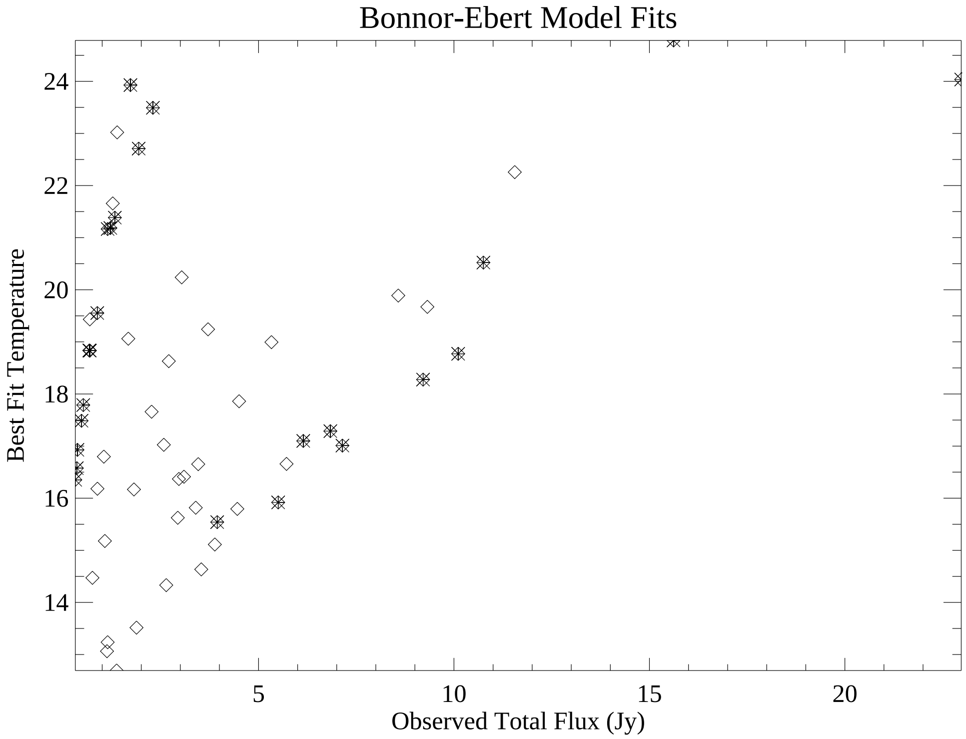

Figure 3.11: Results of the Bonnor-Ebert sphere modelling of submillimetre clumps - best fit temperature versus observed total flux. Asterisks denote clumps that have concentrations outside the range fit by a stable BE sphere model.

discussed in the previous section. This trend may be real; the highest flux objects have likely accreted the most mass and are more evolved (also evident from the typically high concentrations of these objects; see discussion in Section 3.4), which would lead to higher expected temperatures. Parameters fit to the BE model are less reliable for unstable BE spheres, however, as at supercritical concentrations in the model, small variations in the concentration lead to larger variations in the radius and density.

Chapter 4

Clump Environment Part I

The submillimetre observations are sensitive only to small-scale structure, regions where stars are likely to form. On the other hand, the extinction data, with (relatively) low resolution, are only sensitive to the large scale or overall structure of the cloud. These two data sets are complementary, and, through comparisons of the two, much can be learned about the environment in which clumps (and thus stars) form.

4.1 Extinction Threshold

We first examine where the flux in the submillimetre clumps lie in the extinction map. Table 4.1 and Figure 4.1 demonstrate that most of the mass of the cloud lies at low extinction (57% at $A_V < 5$ and 1% at $A_V > 10$), while the small scale submillimetre structure is strongly biased in location towards the highest extinction regions of the cloud (2% at $A_V < 5$ and 13% at $A_V > 10$). Furthermore, the extinction data cover a larger region than the submillimetre data. The region of the extinction map where submillimetre observations exist contains a higher fraction of high extinction material than is found in the extinction map in its entirety (also shown in both Table 4.1 and Figure 4.1). The extinction data of the entire region of Figure 2.1 suggest 84% of the mass of the cloud is at $A_V < 5$ and

Table 4.1. Distribution of mass in the Perseus molecular cloud binned with extinction.

A_V Range	Cloud Area [a] (%)	Cloud Mass [a] $M_\odot$	Cloud Mass [a] %	Cloud Mass [b] $M_\odot$	Cloud Mass [b] %	Clump Mass $M_\odot$	Clump Mass %	Mass Ratio [b] (%)
0-12	100	49768	100	17294	100	174.3	100	1.0
0-5	94.5	41786	84.0	9832	56.9	3.1	1.8	0
5-10	5.4	7756	15.6	7234	41.8	149.1	85.5	2.1
10-12	0.1	227	0.4	227	1.3	22.1	12.7	9.7

[a] Over entire area of our extinction map

[b] Over the region of the extinction map where submillimetre data also exist

a mere 0.4% at $A_V > 10$.

These data suggest small scale structure and hence stars are able to form only at higher extinctions but it is possible that this result is an observational bias. For example, in low extinction regions, the external pressure is lower (a lower column density is probably the result of a lower density) and structures can be expected to be more diffuse, and thus possibly more difficult to detect. Modelling of the clumps to determine the effect of lower extinction on observability is necessary to ensure that the above trend is real. We use the BE sphere model discussed in the previous chapter to represent the submillimetre clumps and thus determine the effect of a lower extinction environment on their observable properties. Following the procedure of Johnstone, Di Francesco, & Kirk (2004), we demonstrate that the preferential location of submillimetre structure in the highest extinction regions is not an observational bias.

We use the extinction as a measure of the local pressure and determine how a model clump's (BE sphere's) observable properties would be expected to vary with extinction for a given importance of self gravity (or λ). Following McKee (1989), the pressure at depth r is $P(r) = \pi G \overline{\Sigma} \Sigma(r)$ where $\overline{\Sigma}$ is the mean column density and $\Sigma(r)$ the column density measured from the cloud surface to depth r. Near

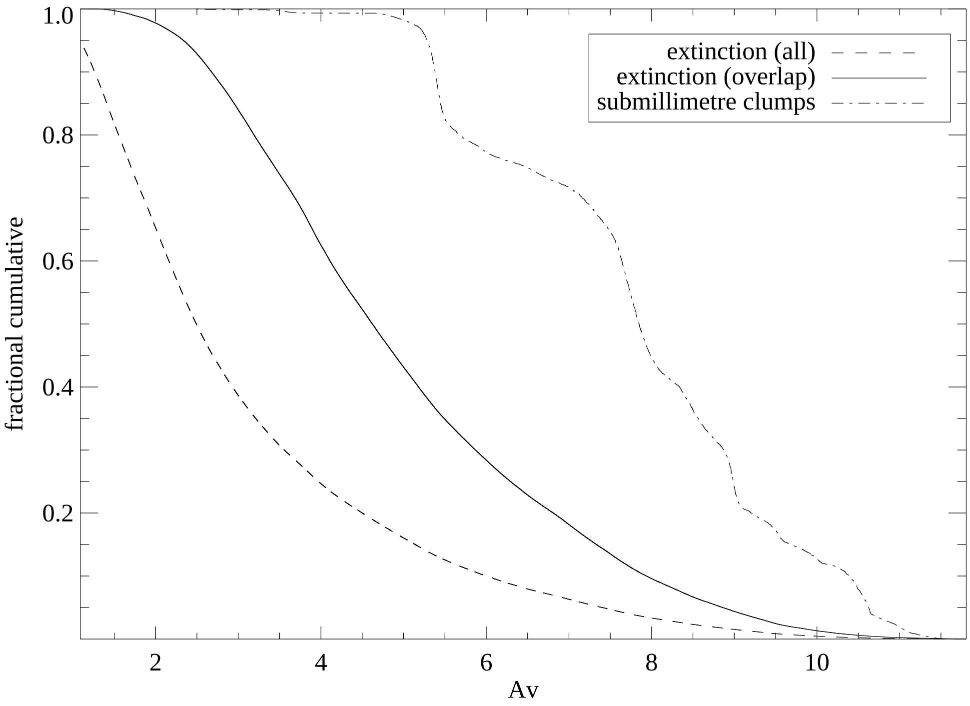

Figure 4.1: Cumulative mass in extinction and submillimetre map versus extinction. The dashed line indicates the extinction over the entire region of Fig. 2.1, while the solid line indicates the extinction only in the region of Fig. 2.1 where our submillimetre data exist.

the centre of the cloud, $\Sigma(\mathrm{r}) \simeq \Sigma(\mathrm{s})/2$, where $\Sigma(\mathrm{s})$ is the column density through the cloud at impact parameter s. The extinction can be expressed as $\mathrm{A_V} = (\Sigma/\Sigma_0)$ mag where $\Sigma_0 = 4.68 \times 10^{-3}$ g cm^{-2} (McKee 1989). The pressure in the cloud at depth r can then be approximated as $\mathrm{P(r)/k} = 1.7\times10^4 \overline{\mathrm{A}}_\mathrm{V}\mathrm{A_V(s)}$ cm^{-3} K, where $\overline{\mathrm{A}}_\mathrm{V}$ is the mean extinction through the cloud (which we take to be 2.2 mag) and $\mathrm{A_V(s)}$ is the extinction through the cloud at impact parameter s. For a given λ, or importance of self gravity, the mass and radius of a BE sphere scale as $\mathrm{M_{BE}} \propto \mathrm{P}^{-1/2}$ and $\mathrm{R_{BE}} \propto \mathrm{P}^{-1/2}$ (Hartmann 1998), and thus the column density scales as $\Sigma_\mathrm{BE} \propto \mathrm{P}^{1/2}$. If we assume a constant temperature and dust grain opacity, then for a given λ, observable clump properties scale as follows - $\mathrm{S_{850}} \propto \mathrm{A_V(s)}^{-1/2}$, $\mathrm{f_0} \propto \mathrm{A_V(s)}^{1/2}$, and $\mathrm{R} \propto \mathrm{A_V(s)}^{-1/2}$, where $\mathrm{S_{850}}$ is the total flux, $\mathrm{f_0}$ is the peak flux, and R the radius. All three quantities increase with increasing λ.

Fig. 4.2 plots these quantities versus the local extinction. The diamonds indicate all submillimetre clumps while the overplotted asterisks indicate all clumps except those in L1448 which may be in a more evolved core region (see the following section). The dashed line indicates the relationship expected for a critical BE sphere; although in our original BE analysis, all of the clumps were fit to stable (subcritical) BE spheres, some appear in the unstable regime of this plot due to the difference between the external pressure required for stability and that supplied by the local extinction. The dotted line shows the relationship at a lower λ, showing our detection of clumps at higher extinctions is incompatible with the non-detections at lower A_V. If all of the clumps detected are considered, the extinction threshold appears to be at $A_V \sim 5$. However, if we ignore the clumps in L1448 (non-asterisked diamonds) then we find an extinction threshold at $A_V \sim 7$.

Column density or extinction thresholds for star formation have been found in other regions. Our previous work (Johnstone, Di Francesco, & Kirk 2004, see also Appendix A) used the same method of analysis as outlined above to argue that an extinction threshold of $A_V \sim 10$ exists in the Ophiuchus molecular cloud.

The archival data included in the present analysis were also examined by

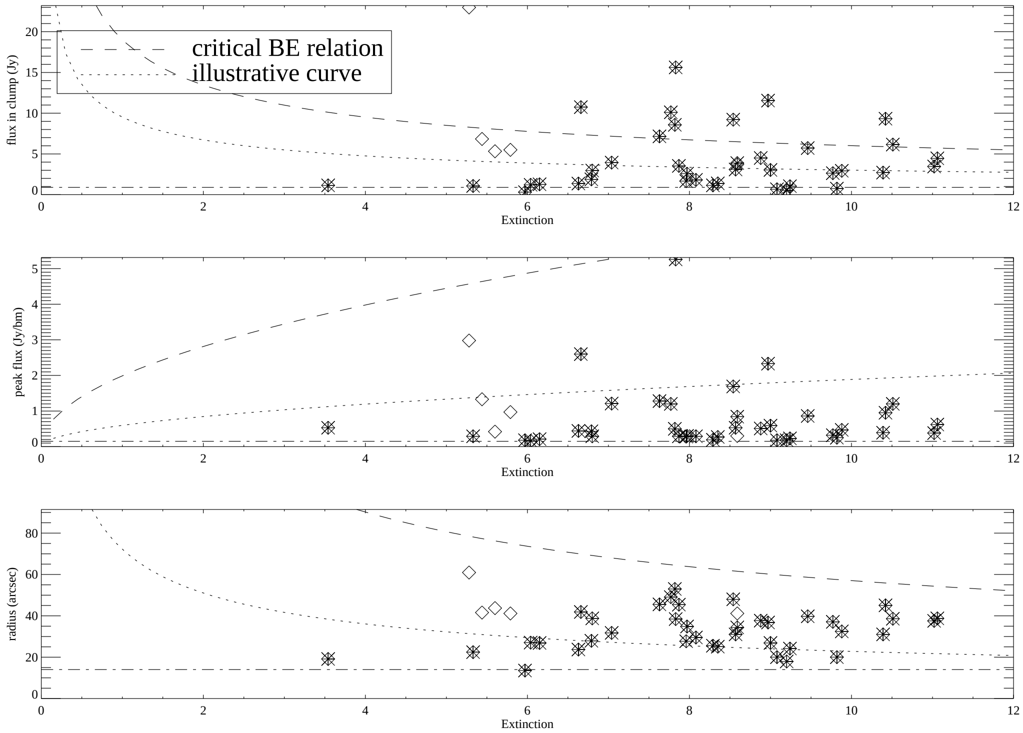

Figure 4.2: Extinction threshold of submillimetre clumps. Each clump's total flux, peak flux, and radius are plotted versus the extinction at that location. The dashed line indicates the critical Bonnor-Ebert sphere, while the dotted line is an illustrative curve at lower importance of self-gravity to guide the eye. The dash-dot line denotes the observational thresholds below which Clumpfind would not identify clumps. The observational threshold for the total flux is derived similarly to the incompleteness level for the mass distribution, as discussed in Section 4.1.1. Diamonds represent all of the clumps while the asterisks denote those not found in the L1448 region (see text for details).

Hatchell et al. (2005). $C^{18}O$ observations are used to measure the large scale structure of the cloud, and are compared with the submillimetre data to search for a column density threshold. Hatchell et al. examine the distribution of submillimetre clumps (identified through a contouring procedure rather than Clumpfind) with respect to the background column density inferred from $C^{18}O$ in terms of a probability distribution weighted towards how frequently each column density occurs in the map rather than an absolute threshold. They find a sharply decreasing likelihood towards submillimetre clumps existing at lower extinctions, but find a non-zero probability for their lowest extinction bin. The sharp decrease in probability is in agreement with the results we present in Table 4.1. However, Hatchell et al. find ten clumps at an $A_V < 5.2$, contrary to our results (we identify one, which may be noise). Our single low extinction clump corresponds to one of Hatchell et al.'s ten. A further three of the ten do not correspond to any structure in our map. As stated earlier, most of our clumps do correspond well to those found by Hatchell et al., with the differences mainly due to definitions of clump boundaries and identification thresholds which are not easily comparable given the different data reduction methods. The three unmatched clumps are located in regions where there is no structure in our map above the threshold we set for identification. In fact, by eye, there appears to be only possible noise features. The isolation of these three clumps from regions containing the bulk of the substructure and clumps coupled with the lack of visible structure in our map suggests that these have a higher probability of being noise features. The remaining 6 clumps are located in regions where we see substructure and clumps; however, the extinction we measure at these locations is much higher (two clump locations are at 5.5 - 6 mag, while the other four are around 8-9 mag in our map). It appears that the majority of the disagreement in clumps found at low column densities is due to the different methods of calculating column density and extinction. Our method (using extinction) is less prone to chemical effects such as freeze out and arguably produces a more accurate count of the total column density of material along the line of sight, although this method would include also any foreground dust along the line of sight and could be distorted by young embedded protostars (see discussion in Section 2.2).

In the Taurus molecular cloud, Onishi et al. (1998) analyzed $C^{18}O$ observations in combination with IRAS data to argue that recently formed protostars are found only in regions with a column density of $N(H_2) = 8 \times 10^{21}$ cm^{-2}, corresponding to an A_V of 8 (using the typical conversion factor of $N(H_2)/A_V = 10^{21}$). The sources considered to be recently formed protostars are 'cold IRAS sources' where the colours indicate that there is heavy dust enshroudment, corresponding roughly to the class I stage. Since $C^{18}O$ is known to deplete in high column density regions (Tafalla et al. 2002), the actual value of the threshold may be larger. Furthermore, Onishi et al. (1998) found that *all* regions with column densities above this threshold contain cold IRAS sources, suggesting that once the critical density is reached, formation occurs quickly. In contrast, we find several extinction regions (cores #6, 7, 9, 11, and 26 or super core #6) in Perseus above our extinction threshold that do not contain any submillimetre clumps. This may be a reflection of the different environment in which stars form in the two clouds, or it may an observational effect. The Taurus molecular cloud is roughly half as distant as the Perseus molecular cloud (140 ± 10 pc; Kenyon et al. 1994). With the greater distance and different wavelength for observation, perhaps the submillimetre clumps are more difficult to detect than the 'cold IRAS sources'. (We point out that we do not see any hint of structure in the single empty super core, even below our clump detection threshold, which argues that any submillimetre structure it does possess is not comparable to the bright sources in the other extinction cores. There are also no sources from the IRAS point source catalog found within this region, unlike the other cores.) A second possibility is in the definition of the high extinction regions — perhaps our extinction map is divided to a much greater extent. The angular resolution of the two surveys are comparable [Onishi et al. (1998)'s CO maps have a beamsize of $2.7'$, while the extinction maps we use have a resolution of $2.5'$], so that column density structures can be observed to half the physical extent in Taurus, which should make the Taurus structures further subdivided. Perhaps due to freeze out and other chemical effects, $C^{18}O$ observations give a smoother distribution, leading to larger regions being classified as cores than would be if extinction data were used.

In Johnstone, Di Francesco, & Kirk (2004), we argued that the extinction threshold we observed in Ophiuchus could be explained through a model of magnetic support for the clumps. The ambipolar diffusion timescale is expected to become reasonably short only for higher A_V's; in particular, McKee (1989) argues for an extinction between 4 and 8 mag, the exact value depending on the density of the cloud and the characteristic density in which cosmic rays dominate the ionization process. Cloud geometry would also play a role in the column density threshold observed. The extinction threshold we observe in Perseus is consistent with that expected from an ambipolar diffusion model of star formation.

4.2 L1448

This extinction core (#16) is unusual in that it is the only extinction core with a low value of peak extinction that contains submillimetre clumps. Previous studies have shown that L1448 contains several very powerful outflows which have been shown to contain at least as much momentum as that found in the quiescent cores in the region (calculated using the small turbulent velocity observed within the cores), and more energy than the gravitational binding energy of the region (Wolf-Chase et al. 2000). If there is a mechanism in place for transferring even a fraction of the momentum and energy into the surrounding core material, we can expect much of that material to dissipate. Since we are unlikely to have caught this process at its onset, it seems likely that a large amount of material may have already been cleared from this core, leading to the much lower peak extinction than seen in the other submillimetre clump-containing cores. Since this core may be more evolved than the others, we denote it with a different symbol in the extinction threshold analysis to allow considerations both with and without it. In the following analysis, we find the submillimetre clumps in this core exhibit similar properties to those in the other cores, and thus do not mark these separately.

A similar argument for advanced evolution might also be put forth for the NGC1333 region, well known for its active star formation and numerous protostellar jets. Here, we merely note that the extinction properties of submillimetre clumps within the L1448 core appear to be different than the other extinction cores and offer the above evolution argument as a possible reason for this difference.

Chapter 5

Clump Environment Part II

The relationship between the submillimetre clumps and the environment they form in can be further examined. Each submillimetre clump can be associated with the extinction core that it lies within. The properties of this core should determine the local conditions under which the clump was able to form. In this chapter, we examine trends between the submillimetre clumps and their associated extinction core in an effort to better understand the process of substructure formation. The bulk properties of clumps co-habitating an extinction core (eg the average clump mass) is shown in Table 8.4 for all extinction cores that contain at least one clump.

The distribution of clumps within each core is shown in Figure 5.1 for all cores containing more than two clumps. The contours denote the Gaussian fits to each of the cores while the diamonds indicate the clump locations. We will return to discuss the distinctly off-axis and non-uniform distribution of the clumps in each core in the following chapter in the context of a triggering mechanism for star formation in the region.

5.1 Clump Numbers and Masses

The first basic property that we examine is the number of submillimetre clumps found within each extinction core. Figure 5.2 shows that the highest number of

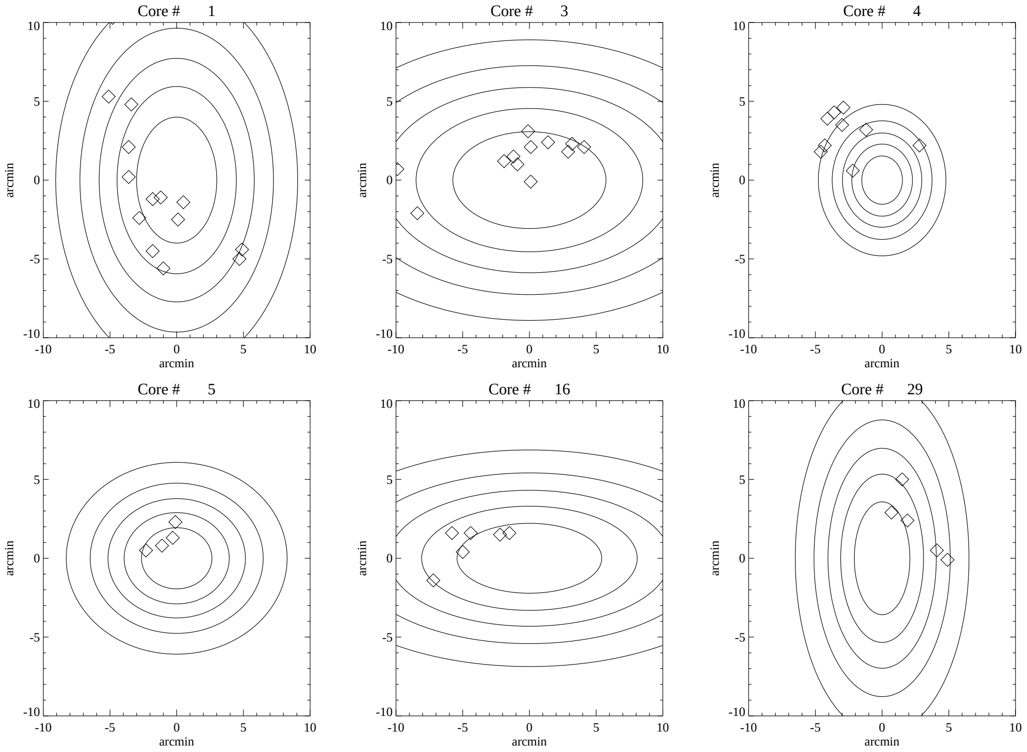

Figure 5.1: The distribution of submillimetre clumps in their parent extinction cores. The contours (spaced at five equal increments from the core peak downwards) show the Gaussian model fit to the core while diamonds indicate the locations of the clumps within. Note the preferentially off-centre distribution of clumps within each core. Only cores containing more than two clumps have been shown.

submillimetre clumps are found within the most massive extinction cores. There is considerable scatter in the trend however, and no distinct mass range in which cores can be separated into those containing and not containing clumps. The extinction core mass used in Figure 5.2 is the mass obtained from the Gaussian fitting of the cores, however, the resulting trend is the same if the total extinction core mass is used instead. The 80 $M_{\odot}$ core that contains a surprising number of clumps is discussed below.

Connected to the number of submillimetre clumps within each extinction core is the total mass of those clumps. Fig. 5.3 illustrates that unlike the total number

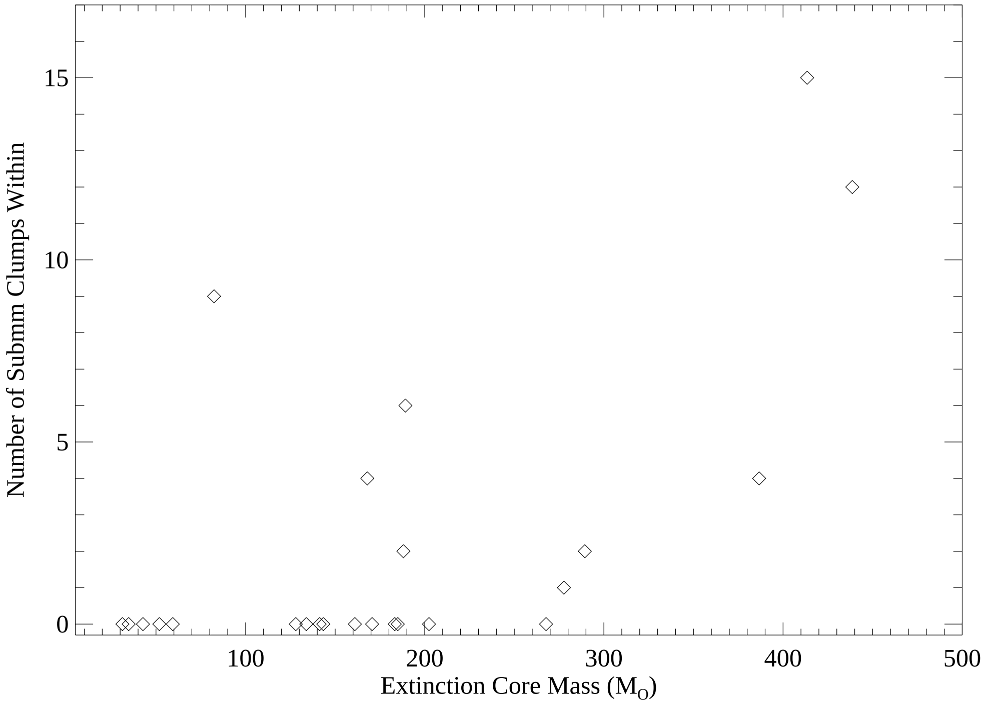

Figure 5.2: Number of submillimetre clumps per extinction core versus the core's mass

of clumps, the total mass in clumps does not appear to depend on the mass of the extinction core in which they reside. Mass estimates for the submillimetre clumps is shown using both a constant T=15 K for all clumps and the temperature for each clump determined in the BE analysis. The mass estimates are systematically higher for the T=15 K case, which may indicate that this temperature estimate tends to be too low for the majority of the clumps (since a higher temperature requires less mass of material to provide the same observed flux than a lower temperature would). Alternatively, the BE temperatures may be too high. Including a higher level of non-thermal support in the model would give lower BE fit temperatures. The highest flux clumps discussed in Section 4.2 do not exist in all of the extinction cores and thus are not solely responsible for the systematic mass difference. As with the previous plot, the overall trend (or lack thereof) does not change with the measure of core mass (Gaussian fit or total mass from Clumpfind). The Gaussian estimate of the masses of the extinction cores does appear to be an underestimate in one case. The core with a Gaussian mass of 80 $M_\odot$ (# 4) contains a significant fraction of this mass in submillimetre clump mass, which is unlikely. This particular extinction core had a larger than average background (4.1 mag) in the Gaussian fit. One would expect the background to be roughly the same for all of the cores. This core may have a higher background due to the neighbouring massive extinction core #1 influencing the best fit. An overly large background would cause an underestimate of the core mass.

The combination of the above two trends — more massive extinction cores tend to harbour more clumps but the same total mass implies smaller average clump masses for more massive regions. The total clump mass found in each extinction core is on the order of the Jeans mass - taking a typical core density of $n_H \sim 10^3$ cm^{-3} and a temperature of ∼15 K yields a Jeans mass of 37 $M_\odot$. Each core thus contains roughly a Jeans mass in submillimetre clumps. The Jeans mass is lower for denser regions which results in smaller Jeans masses for the more massive cores, and thus could encourage the trend of less massive clumps forming within the most massive cores.

The fraction of the extinction core's mass found in submillimetre clumps would be expected to be affected by any turbulent motions in the extinction core. Treating the extinction cores as supported by only thermal pressure, we can invert the Jeans mass equation to determine the temperature required for an extinction core to be supported by only thermal pressure. As discussed earlier, these temperatures are much higher than the environment of the molecular cloud is known to be. However, these derived temperatures can be used as an indicator of the level of non-thermal support required in the extinction cores: higher 'thermal support only' temperatures imply that a higher level of turbulence would be required to support the core. Higher levels of turbulence lead to greater difficulty in forming clumps, as more often the clumps disperse again (a higher level of turbulence leads to a higher effective Jeans mass). Indeed, Figure 5.4 demonstrates that extinction

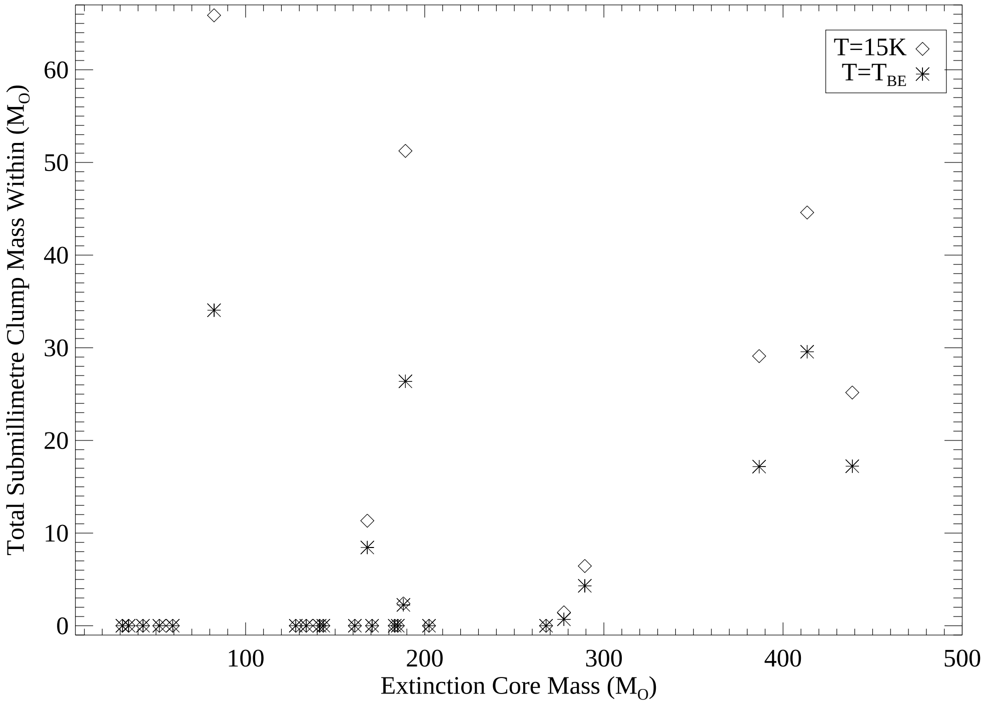

Figure 5.3: Total submillimetre clump mass within each extinction core

cores with the highest 'thermal support only' temperature cores have the lowest fractions of mass in the form of submillimetre structure.

Although the global efficiency of star formation is only several percent, it is observed to rise to around 20% in cluster-forming regions of molecular clouds (Lada & Lada 2003), consistent with the fraction submillimetre clump mass we find in most of the extinction cores (Figure 5.4).

5.2 Concentrations

As can be seen from Table 8.4, the submillimetre clumps generally have a similar range of properties in every extinction core. In particular, all of the cores containing a significant number of clumps (more than 2) possess at least one highly concentrated clump (C > 0.7). This is noteworthy because highly concentrated

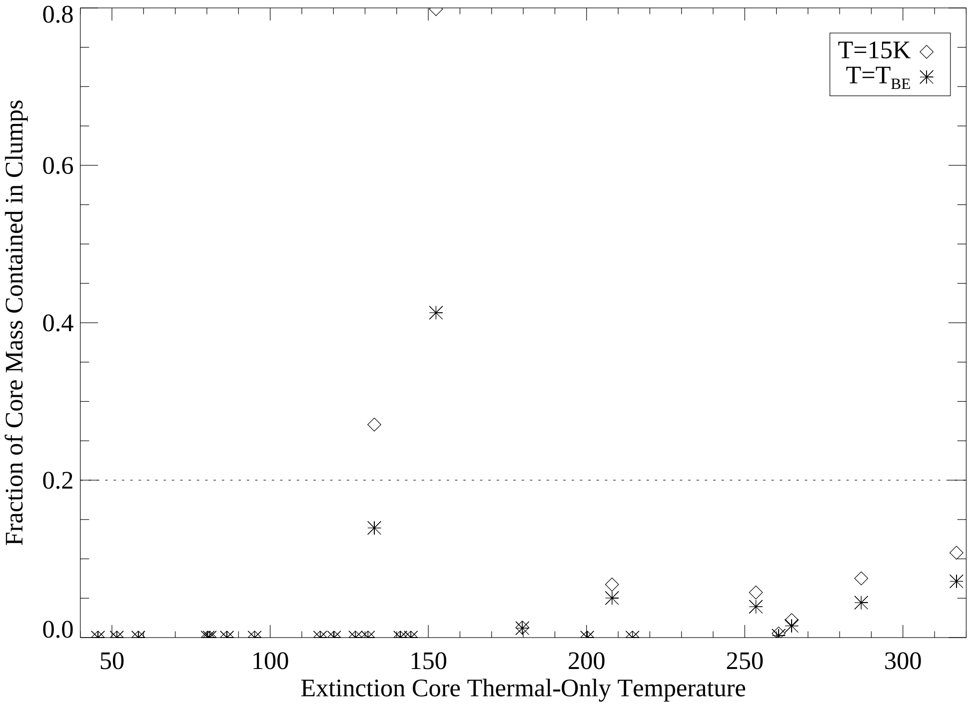

Figure 5.4: Temperature required for extinction core to be supported by only thermal support versus percentage of core's mass found in submillimetre clumps. The dotted line indicates the 20% level, the approximate star formation efficiency observed in most clustered regions (Lada & Lada 2003).

clumps may correspond to more evolved class 0 sources (see Section 3.4 for a discussion on concentration and Appendix B for the correlation between class 0 sources and high concentrations). The presence of at least one highly concentrated clump in each extinction core that contains clumps may therefore indicate that all of these contain at least one young protostar.

If the highly concentrated clumps are all class 0 sources, this has implications for the evolution of the region. For example, this would tie in well with the triggering scenario discussed in Section 3.4. The time for information to travel from an extinction core at one edge of our map to the other is $\sim 10^8$ yrs. (The separation is $\sim 235'$ or 4.5×10^6 AU (22 pc) and the sound speed is ~ 0.23 km s^{-1}

assuming T=15 K.) This time is much longer than the lifetime of the protostellar phase ($\sim 10^4 - 10^5$ yr; Lada & Lada (2003) and references therein). Either all of the cores independently formed a protostar at the same time or their formation was externally triggered throughout the entire region. Such a triggering might be related to the formation of the cloud itself through large scale flows (Hartmann et al. 2001), or through a more localized process such as the nearby formation of stars (see following chapter). The low concentration submillimetre clumps also found within these extinction cores could be either those which formed at a time after the triggering event and are continuing to accrete and increase in central concentration, or they could be the 'failed stars' of the turbulence simulations which simply re-expand into their environment. Other interpretations are also possible, especially since most of the highly concentrated clumps have not been verified as class 0 sources yet.

5.3 Clump Separations

We next examine the separation of submillimetre clumps from the column density peak of the parent extinction core. In order to best compare clumps associated with each core simultaneously, we express the separation in terms of the 'effective σ' of the parent core. The extinction core profiles are two dimensional, so for each submillimetre clump, we measure the Gaussian sigma that the parent core has *in the direction of the clump* ('σ_e') (ie taking into account the angle separating the core's major axis and the direction to the submillimetre clump, rather than averaging the semi-major and -minor axes).

The submillimetre clumps appear to be preferentially off-centre in Fig. 5.1, however we examine this here in a more quantitative fashion. Figure 5.5 shows how the mass in each core is distributed (using the Gaussian model) versus the mass in submillimetre clumps within the core, using the σ_e measure of separation discussed above. The axes have been normalized to unity for easier comparison.

For reference, the extinction cores appearing in the plots below have a mean σ ranging from ∼150″ to ∼400″. Fig 5.5 shows that the closest submillimetre clump is indeed farther separated from the extinction peak than the distribution of mass in the core would suggest. In general, however, the submillimetre clumps are more centrally concentrated than the extinction core mass. This may be explained through the extinction threshold preventing the formation of submillimetre clumps at the largest σ_e away from the core. For example, taking a typical background extinction level of 3 mag, and typical Gaussian fit peak extinction of 6 mag, an extinction threshold of 5-7 mag is reached in $\sim$ 1.5 - 0.9 σ_e. Most of clump mass distributions do indeed begin around this range of σ_e, while the extinction core extends out much further. The one extinction core in violation of this trend (#4) is the 80 $M_\odot$ one discussed in Section 6.1 as likely having a poor Gaussian fit.

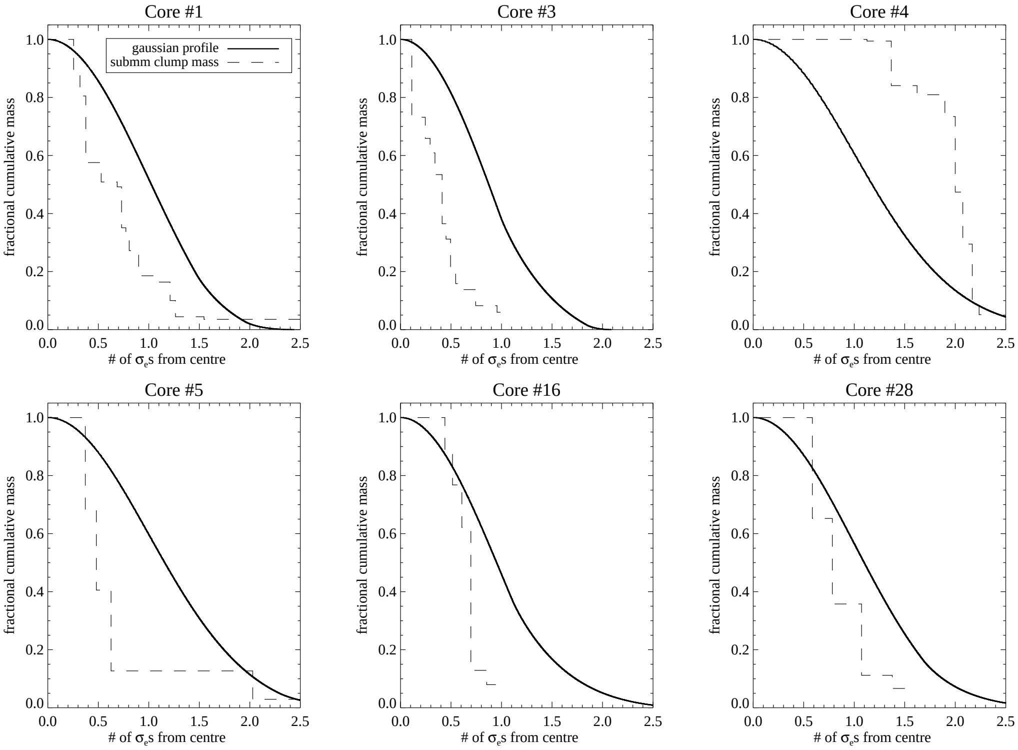

Figure 5.5: Distribution of mass in submillimetre clumps relative to the parent extinction core. The separation is measured in units of 'effective σ's from the centre (see text for details). The cumulative mass has also been normalized for easier comparison.

Chapter 6

Triggered Star Formation

As discussed in the previous chapter, Figure 5.1 illustrates that submillimetre clumps are preferentially located at certain off-axis regions of each extinction core. One would expect from simple models of either magnetic or turbulent support for substructure to preferentially form in the densest regions, which does not appear to be the case here, suggesting another mechanism is at play. Figure 6.1 shows the entire extinction map illustrating the positions of the 6 extinction cores shown in Figure 5.1. The correlation between the preferred submillimetre clump locations in each extinction core over the entire region again suggests the importance of an outside agent in substructure formation or evolution. Models of triggered star formation, as discussed in Chapter 1, may provide an explanation to the submillimetre clump locations seen in Figure 6.1.

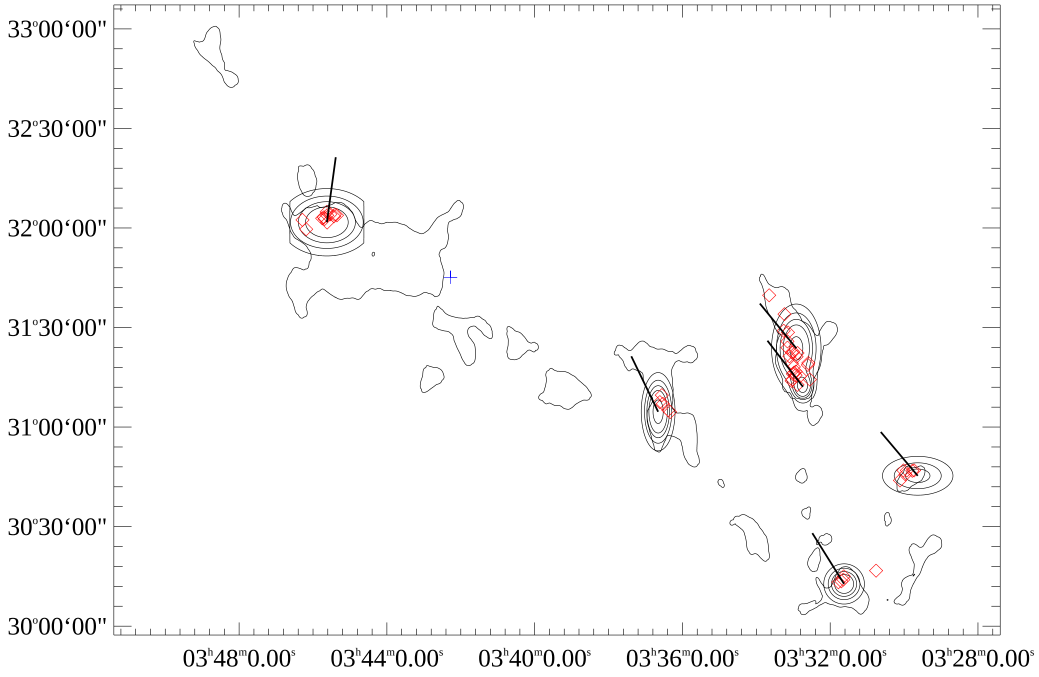

Figure 6.1: Possible evidence for triggering in the Perseus molecular cloud. The background contour indicates the $A_V = 5$ level in the cloud to aid in orientation. Other contours represent gaussian fits to the extinction cores containing significant numbers of submillimetre clumps (red diamonds). Vectors denote the direction of the B star 40 Persei, which has been suggested as a trigger for star formation in the region (see discussion in text). The blue plus indicates the centre of the 'Perseus ring' (see discussion in text).

The small scale ('globule squeezing') triggering scenario shows a promising explanation. Near the Perseus molecular cloud, a group of already-formed, young stars already exists (the Perseus OB association). The massive stars in this group emit copious amounts of ultraviolet radiation which can then heat and ionize nearby dense regions, such as the extinction cores we identify. With sufficient radiation, the core heating can be large enough to lead to mass loss (Walawender et al. 2004). UV radiation would erode the core surface facing the incoming radiation, and could lead to triggering the evolution of substructure on this side through the increase in pressure, while the far side of the core is shielded from the radiation. A triggering source to the north east of the centre of our map (the general direction of the Perseus OB association) appears consistent with the geometry we observe in preferential submillimetre clump locations.

The intermediate scale ('collect and collapse') triggering scenario should lead to the formation of a large ridge or sheet of material which would then collapse to form clumps and stars. The distribution of extinction cores that we observe does not appear to support this scenario, even when viewing the entire extinction map (presented in Alves et al. 2005), although geometry or a set of complex interacting flows could explain this.

Similarly, the large scale ('rings and shells') triggering scenario does not appear to be applicable due to the lack of large scale ring- or shell- like structure visible in the extinction map derived from 2MASS data.

Small-scale triggering has in fact been previously suggested in the Perseus molecular cloud. (Walawender et al. 2004). Infrared observations of a cometary cloud in the L1451 region that appears to be eroding by UV radiation lead to the suggestion that the star 40 Persei, a B0.5 star belonging to the Perseus OB assocation (Walawender et al. 2004), is the likely candidate for triggering. This star is reasonably close and it possesses a position angle well matched to the observed angle of erosion present. The vectors in Figure 6.1 indicate the direction of 40 Per from each of the relevant extinction cores. These vectors may not appear to all point precisely to a single point due to the effect of the projection of our map onto a tangent plane. (All of the direction vectors were computed on the sky, rather than on the tangent plane.) While the correspondence between the vectors and the preferential submillimetre clump locations is not perfect, the two are clearly in very good agreement given that we are only viewing a 2D projection of the actual 3D situation. We therefore conclude that the scenario of 40 Per as a source of triggering is consistent with our observations; this does not rule out the possibility of a different source being responsible for triggering of the region, although such a source would need to have a similar angle of separation between each of the extinction cores. Given the projected proximity of the extinction cores to one another, the triggering scenario is also consistent with the discussion in the previous section on the possibility of each core containing roughly the same age oldest protostar.

Another interesting feature in the Perseus molecular cloud is a ring observed in $C^{18}O$ velocity observations as a part of the COMPLETE survey (Ridge et al. 2005). These observations led to the suggestion that the ring was behind the bulk of the cloud and would thus not be responsible for any triggering. We test the possibility of the source of the ring as a potential source of the trigger and find the location to be inconsistent with our observations. The centre of the ring lies at RA $\sim$ 3h40m and dec $\sim 31^o 45'$(the plus in Figure 6.1), and thus is much too low to be the trigger, consistent with the hypothesis of a location behind the cloud (Ridge et al. 2005).

One outstanding puzzle is the extinction cores which show no evidence of clumps, especially the ones with significant portions above the extinction threshold (#6, 7, 9, 11, and 26) as discussed earlier (Section 4.1). The three dimensional geometry of the extinction cores is not known, but this could explain the lack of submillimetre clumps seen in these 'empty' extinction cores. Shielding by a large column of cloud material separating the empty extinction cores from the trigger is possible. Higher signal to noise observations of the 'empty' extinciton cores may reveal submillimetre clumps, but any such clumps would possess a lower mass and central density than the clumps presented here. This would still lead to the question of why two extinction cores with similar peak extinctions would develop different populations of submillimetre clumps. Detailed observations of the 'empty' extinction cores (especially extinction core #6 which does not belong to a super core in which clumps are observed) are required to understand what processes are going on.

Chapter 7

Conclusions & Future Work

7.1 Conclusion

We present an analysis of 3.5 square degrees of submillimetre continuum data and the corresponding extinction map of the Perseus molecular cloud. We identify structure in both the submillimetre (clumps) and extinction (cores and super cores) maps. The cumulative mass distribution of all three sets of structures are well characterized by broken power laws. The submillimetre clumps and extinction cores have high-end mass distribution slopes of $\alpha \approx 2\pm0.1$ and 1.8 ± 0.1 respectively. These are steeper than the Salpeter IMF ($\alpha \sim 1.35$), but within the range found in submillimetre clumps in other star forming regions. The mass distribution of extinction super cores was best fit by a shallow slope of $\alpha = 0.8\pm0.2$, corresponding to slopes observed in large scale CO maps. The difference between the extinction cores and super cores may be an observational bias (e.g., a result of the definition of the two groupings) or it may indicate the scale over which different processes become important in fragmentation.

The majority of submilimetre clumps are well fit by a Bonnor-Ebert sphere model with external pressures ranging from $5.5 < \log_{10}(\mathrm{P_{ext}/k}) < 6.2$ and temperatures ranging from 13 to 25 K. The derived pressures are comparable to the pressures expected to be exerted by the weight of the surrounding cloud material and the temperatures fall within the range expected for a molecular cloud.

We show that small scale (submillimetre) structure is located only in regions of high extinction. Submillimetre clumps are found only at $A_V > 5$-7, although BE models suggest that we should have been able to detect clumps at lower A_V had they existed. In turn, this suggests that clumps are only able to form above a certain extinction level. An extinction threshold is consistent with the model of magnetic support, where the timescale for ambipolar diffusion is only of a reasonable length in regions above an A_V of 4 - 8 mag. It is less clear if the turbulent support model can explain our observations.

The relationship between the submillimetre clumps and their parent extinction cores was examined. Extinction cores containing submillimetre clumps tended to contain approximately one Jeans mass of submillimetre clump material, although this was found to be split into a larger number of clumps for the more massive extinction cores. The mass of the submillimetre clumps tended to be more concentrated towards the extinction core centre than the total core mass.

The submillimetre clumps were preferentially found in specific off-axis regions of the extinction cores. The correlation of these locations suggests a small-scale triggering event formed the submillimetre clumps in the region. Furthermore, the position of the young B0 star 40 Per, previously suggested as a source of triggering for the region, coincides with the expected position of a triggering source.

7.2 Future Work

In addition to the observations of the Perseus molecular cloud presented here, we also have coverage of the Ophiuchus molecular cloud, much of which was published in Johnstone, Di Francesco, & Kirk (2004). This latter data set has not yet had the full analysis described here applied to it and a small amount of data has been collected since publication. The structure in the extinction map of Ophiuchus is much less discrete and 'clumpy' than in Perseus, and it will be interesting to find out if this has a bearing on the results of an analysis similar to that done for Perseus.

Observationally, the COMPLETE survey in the submillimetre has not yet been completed - one of the survey goals was to map the Perseus, Ophiuchus, and Serpens molecular clouds over the entire region with $A_V \geq 5$. The outer edges of the Perseus and Ophiuchus maps and the bulk of the Serpens map require further observations. The analysis of correlations between the submillimetre and extinction structure would be strengthened with coverage to a uniform A_V. We have applied for time at the JCMT to complete the coverage of all three clouds throughout semesters 05A (Ophiuchus) and 05B (Perseus and Serpens). Both proposals were highly ranked (within the top quartile); unforunately, due to continued mechanical problems with the SCUBA cryogenic detector, these observations will not be completed. A new detector, SCUBA-2, is planned for the JCMT and installation on the telescope tentatively will begin in early 2006. SCUBA-2 consists of a larger, more sensitive array of bolometers that will be able to map large regions to the same depth as SCUBA at speeds up to 1000 times faster. This instrument will be well suited for providing deep maps covering an entire molecular cloud to a lower extinction level. Large surveys have been proposed to take advantage of SCUBA-2, including one ('Gould's Belt', in which I am involved) to survey all nearby star forming regions (within 500 pc) to uniform A_V. The tools of analysis and results developed for this work will be of great use to apply to such observations.

These results will complement the direction of my future research in star formation. The goal is to use this set of tools in a future project to approach the formation of clumps in molecular clouds from a more theoretical angle. We have data from turbulent simulations from several different groups of researchers (including both driven and non-driven turbulence) to which we can apply the above set of tools in determining how well each does at simulating reality. Applications to the magnetic support and triggering scenarios should also be included.

I am also part of a collaboration including Mario Tafalla (OAN, Spain) that has begun an observational project which will also tie in with the goals of the research above. The project involves measuring the velocities of clumps in order to characterize the nature of the turbulence present in the molecular cloud and thus constrain the various models of star formation. The clumps are to be used as 'tracer particles' which follow the global internal motions of the molecular cloud. The internal clump velocity dispersion (derived from observations of N_2H^+ across the clump) gives a measure of the conditions for clump formation, while the dispersion of center-line velocities of the collection of clumps measures the overall cloud or core turbulence. Simulations are able to predict these measures as well, and hence the observations can be used to constrain directly the numerical simulations of star formation. We have successfully obtained data from the IRAM 30m telescope in Spain, applying this observational technique to the submillimetre clumps in Perseus listed in this thesis. The variety of star forming environments can then also be observed through the comparison of the results we find here with those previously observed in the Taurus molecular cloud, well known as a region undergoing an isolated mode of star formation, unlike Perseus which is undergoing a more clustered mode of formation.

As a second goal, we have found the multi-wavelength analysis of B1 described in Appendix B to be enlightening, and are expanding the project to similarly characterize other star forming regions. We are currently working on a similar analysis of the IC348 region of star formation in Perseus.

Chapter 8

Tables

Table 8.1. Properties of submillimetre clumps in Perseus.

RA [a] (J2000.0)	Dec [a] (J2000.0)	f_0 [b] (Jy/bm)	S_{850} [b] (Jy)	R_{eff} [b] ($''$)	Mass[c] $M_\odot$	Conc[d]	Temp[d] (K)	M_{BE}[d] $M_\odot$	log n_{cent}[d] cm^{-3}	log P_{ext}/k[d] cm^3 K^{-1}	H05 [e] #
3:29:09.9	31:13:31.1	5.26	15.62	38.	14.2	0.84	25.	6.65	5.8	6.1	48
3:25:36.0	30:45:10.8	2.98	22.98	61.	20.9	0.84	24.	10.22	5.4	5.6	27
3:29:11.3	31:13:07.4	2.60	10.75	42.	9.8	0.82	21.	6.00	5.7	5.8	41
3:29:03.2	31:15:53.6	2.33	11.55	37.	10.5	0.72	22.	5.73	5.8	6.0	43
3:28:55.3	31:14:27.9	1.69	9.21	48.	8.4	0.82	18.	6.11	5.5	5.6	44
3:25:38.9	30:43:59.8	1.33	6.84	42.	6.2	0.77	17.	4.95	5.6	5.7	29
3:33:17.9	31:09:27.8	1.28	7.15	46.	6.5	0.79	17.	5.30	5.5	5.6	1
3:32:18.0	30:49:45.4	1.21	3.94	32.	3.6	0.75	16.	3.39	5.8	5.8	76
3:33:21.7	31:07:22.2	1.20	10.11	49.	9.2	0.73	19.	6.44	5.5	5.6	2
3:43:57.0	32:00:49.7	1.20	6.15	39.	5.6	0.73	17.	4.52	5.6	5.7	12
3:25:22.5	30:45:06.5	0.97	5.50	41.	5.0	0.74	16.	4.54	5.6	5.6	30
3:29:01.4	31:20:23.1	0.95	9.32	45.	8.5	0.63	20.	5.53	5.3	5.8	45
3:29:10.5	31:18:25.1	0.86	5.72	40.	5.2	0.68	17.	4.39	5.5	5.7	46
3:43:57.2	32:03:01.6	0.84	3.88	34.	3.5	0.70	15.	3.49	5.6	5.7	13
3:28:59.5	31:21:28.7	0.62	4.46	39.	4.1	0.63	16.	3.73	5.3	5.7	47
3:29:06.5	31:15:36.3	0.59	3.03	27.	2.8	0.45	20.	1.73	5.1	6.1	50
3:29:08.8	31:15:12.8	0.53	3.09	31.	2.8	0.53	16.	2.43	5.2	5.9	51
3:31:21.0	30:45:25.6	0.53	1.14	19.	1.0	0.55	13.	1.29	5.6	6.2	77
3:29:03.7	31:14:47.7	0.51	4.50	38.	4.1	0.52	18.	3.10	5.0	5.8	52
3:33:16.1	31:06:51.6	0.50	8.57	53.	7.8	0.53	20.	5.01	4.8	5.6	4
3:27:39.0	30:12:53.6	0.47	2.93	32.	2.7	0.54	16.	2.50	5.2	5.8	35
3:44:44.2	32:01:26.9	0.44	1.37	24.	1.2	0.57	13.	1.67	5.5	5.9	14
3:28:36.7	31:13:23.6	0.43	1.88	28.	1.7	0.57	14.	2.04	5.3	5.9	49
3:25:25.7	30:45:01.6	0.42	5.33	44.	4.9	0.49	19.	3.34	4.8	5.7	34
3:29:10.2	31:21:43.0	0.39	2.71	31.	2.5	0.44	19.	1.74	4.9	5.9	54
3:29:07.4	31:21:48.4	0.38	3.46	38.	3.1	0.50	17.	2.65	5.0	5.7	56
3:27:42.7	30:12:24.5	0.36	3.39	39.	3.1	0.52	16.	2.83	5.0	5.7	36
3:43:51.1	32:03:20.9	0.32	2.64	37.	2.4	0.54	14.	2.59	5.0	5.7	81
3:28:40.1	31:17:48.4	0.32	2.27	31.	2.1	0.44	18.	1.59	4.9	5.9	55
3:25:49.3	30:42:15.1	0.30	3.71	41.	3.4	0.44	19.	2.28	4.7	5.7	32
3:28:39.1	31:18:24.1	0.30	2.58	35.	2.3	0.45	17.	1.91	4.8	5.8	60
3:47:41.8	32:51:40.3	0.29	1.07	22.	1.0	0.43	15.	0.95	5.1	6.0	78
3:29:18.4	31:25:02.7	0.29	3.53	45.	3.2	0.54	15.	3.36	4.9	5.5	57
3:29:18.5	31:23:08.8	0.29	1.81	30.	1.7	0.44	16.	1.46	4.9	5.8	63
3:27:48.3	30:12:08.0	0.29	2.96	39.	2.7	0.47	16.	2.34	4.8	5.7	37

Table 8.1 (cont'd)

RA [a] (J2000.0)	Dec [a] (J2000.0)	f_0 [b] (Jy/bm)	S_{850} [b] (Jy)	R_{eff} [b] ($''$)	Mass[c] $M_\odot$	Conc[d]	Temp[d] (K)	M_{BE}[d] $M_\odot$	log n_{cent}[d] cm^{-3}	log P_{ext}/k[d] $cm^3\ K^{-1}$	H05 [e] #
3:44:01.8	32:01:54.6	0.28	1.67	28.	1.5	0.40	19.	1.04	4.8	5.9	16
3:29:06.8	31:17:18.3	0.27	1.38	25.	1.3	0.37	23.	0.65	4.7	5.9	62
3:29:52.0	31:39:03.4	0.25	0.75	20.	0.7	0.42	14.	0.73	5.1	6.0	–
3:47:39.0	32:52:11.2	0.25	1.12	26.	1.0	0.48	13.	1.30	5.1	5.8	79
3:44:03.3	32:02:24.3	0.23	1.72	29.	1.6	0.30	24.	0.77	4.6	5.8	18
3:27:37.9	30:13:53.2	0.23	1.04	24.	0.9	0.40	17.	0.79	4.8	5.9	39
3:29:23.4	31:33:15.7	0.23	0.68	19.	0.6	0.35	19.	0.41	4.8	6.0	58
3:29:17.2	31:27:44.4	0.22	0.88	23.	0.8	0.40	16.	0.71	4.9	5.9	61
3:43:58.2	32:04:01.4	0.21	1.27	27.	1.2	0.35	22.	0.66	4.6	5.8	17
3:44:06.6	32:02:05.6	0.19	1.14	26.	1.0	0.29	21.	0.61	4.6	5.8	20
3:29:25.1	31:28:16.1	0.18	0.37	15.	0.3	0.28	17.	0.27	5.0	6.1	64
3:29:00.2	31:11:53.0	0.18	0.35	15.	0.3	0.30	17.	0.27	5.0	6.1	65
3:29:15.0	31:20:32.1	0.18	0.69	21.	0.6	0.30	19.	0.44	4.7	5.9	70
3:33:13.8	31:19:51.3	0.18	0.67	20.	0.6	0.28	19.	0.42	4.8	5.9	82
3:44:36.9	31:58:40.7	0.18	0.52	18.	0.5	0.31	18.	0.36	4.8	6.0	19
3:26:37.2	30:15:18.7	0.18	0.31	14.	0.3	0.27	16.	0.25	5.0	6.2	80
3:33:05.9	31:04:56.6	0.17	1.32	29.	1.2	0.28	21.	0.70	4.5	5.7	6
3:43:38.3	32:03:05.6	0.16	0.47	17.	0.4	0.23	17.	0.34	4.9	6.0	23
3:43:44.0	32:02:46.4	0.16	1.21	27.	1.1	0.20	21.	0.64	4.6	5.8	26
3:25:42.5	30:45:12.9	0.15	2.30	40.	2.1	0.26	23.	1.05	4.3	5.5	–
3:43:42.6	32:03:16.7	0.15	0.88	24.	0.8	0.20	20.	0.52	4.6	5.8	24
3:33:02.2	31:04:20.3	0.15	1.93	36.	1.8	0.24	23.	0.93	4.3	5.6	5

[a] Position of peak flux within clump (accurate to $6''$).

[b] Peak flux, total flux, and radius derived from *clfind* (Williams, de Geus, & Blitz 1994).

[c] Mass derived from the total flux assuming $T_d = 15$ K and $\kappa_{850} = 0.02\,\mathrm{cm}^2\ \mathrm{g}^{-1}$.

[d] Concentration, temperature, mass, central number density, and external pressure derived from Bonnor-Ebert modelling (see text).

[e] Best corresponding submillimetre clump in Hatchell et al. (2005). Different methods in data reduction and clump identification are responsible for most of the differences in identified clumps.

Table 8.2. Properties of extinction cores in Perseus.

Ref #	RA [a] (J2000.0)	Dec [a] (J2000.0)	Peak [b] A_V	Mass [b] ($M_\odot$)	R_{eff} [b] ($''$)	<n> [b] ($10^5 cm^{-3}$)	$Peak_g$ [c] (A_V)	A_{0g} [c] (A_V)	$Mass_g$ [c] ($M_\odot$)	σ_x [c] ($''$)	σ_y [c] ($''$)
1	3:29:01.7	31:22:53.1	11.8	1599.1	601.	1.9	6.9	3.7	413.4	291.	429.
2	3:32:29.8	30:58:10.7	11.5	578.6	351.	3.4	7.4	2.8	289.4	393.	184.
3	3:43:57.5	32:00:55.6	10.6	1302.2	499.	2.7	5.8	3.5	438.6	604.	328.
4	3:28:50.0	31:11:14.7	10.8	734.2	410.	2.7	6.4	4.1	82.4	145.	159.
5	3:27:37.7	30:11:35.3	10.2	623.2	376.	3.0	5.9	3.5	167.9	249.	203.
6	3:36:22.5	31:11:01.3	9.9	1594.1	656.	1.4	6.0	3.5	202.4	322.	191.
7	3:41:56.5	31:47:36.3	9.7	1115.7	487.	2.5	3.6	5.6	128.0	340.	212.
8	3:33:21.3	31:18:52.1	9.6	1256.7	543.	2.0	5.9	2.6	386.6	429.	321.
9	3:40:49.8	31:49:33.6	8.5	745.3	392.	3.1	–	–	–	–	–
10	3:47:41.0	32:52:46.5	8.5	747.5	446.	2.1	4.5	2.8	188.1	221.	352.
11	3:40:24.3	31:58:18.6	8.0	574.7	378.	2.7	–	–	–	–	–
12	3:30:25.5	30:26:35.0	7.2	540.2	372.	2.7	4.9	2.0	267.7	475.	239.
13	3:24:49.6	30:22:14.9	6.6	340.4	298.	3.3	3.4	2.4	183.3	567.	213.
14	3:39:27.1	31:22:24.3	6.7	859.8	471.	2.1	2.3	4.2	34.7	111.	282.
15	3:28:35.3	30:18:48.9	6.4	204.2	235.	4.0	2.7	2.2	184.9	267.	725.
16	3:25:15.7	30:43:28.4	6.1	367.3	319.	2.9	3.5	2.2	189.2	516.	233.
17	3:44:35.9	32:13:52.6	6.2	682.8	437.	2.1	3.4	2.3	170.6	402.	242.
18	3:37:54.3	31:23:17.8	6.1	697.6	438.	2.1	2.2	3.3	133.9	556.	266.
19	3:28:58.3	30:44:17.2	5.9	410.1	359.	2.3	2.8	3.1	31.2	174.	122.
20	3:40:27.2	31:15:00.5	5.8	1102.5	563.	1.6	1.8	3.9	42.7	270.	189.
21	3:25:25.6	30:18:56.9	6.0	333.5	297.	3.2	–	–	–	–	–
22	3:28:05.6	30:25:17.6	5.7	101.2	163.	5.9	–	–	–	–	–
23	3:28:51.3	30:04:11.2	5.7	260.2	270.	3.4	–	–	–	–	–
24	3:28:48.5	30:33:09.3	5.7	170.1	221.	4.0	2.9	2.5	51.9	198.	163.
25	3:26:11.5	30:30:22.5	5.4	148.6	210.	4.0	3.0	2.3	59.4	254.	143.
26	3:41:45.2	31:56:26.0	9.1	517.8	324.	3.9	4.0	4.3	143.4	464.	165.
27	3:44:50.0	31:41:07.9	7.2	594.5	377.	2.8	3.0	3.7	141.3	264.	338.
28	3:43:27.4	31:43:02.1	8.6	300.4	239.	5.6	3.5	4.6	161.0	246.	381.
29	3:33:25.1	31:04:28.5	9.7	327.1	247.	5.5	7.2	2.2	277.7	196.	375.

[a] Position of peak extinction within core (accurate to 2.5′).

[b] Peak extinction, mass, radius, and mean number density derived from Clumpfind (Williams, de Geus, & Blitz 1994) with several clumps further separated. See text for details.

[c] Peak extinction, background extinction, mass, and σ's derived from results of Gaussian fitting. See text for details.

Table 8.3. Properties of extinction super cores in Perseus.

Ref #	RA [a] (J2000.0)	Dec [a] (J2000.0)	Peak [b] A_V	Mass [b] ($M_\odot$)	R_{eff} [b] ($''$)	<n> [b] 10^5cm^{-3}
1	3:29:01.7	31:22:53.1	11.8	2333.3	727.	1.5
2	3:32:29.8	30:58:10.7	11.5	2162.3	692.	1.7
3	3:43:57.5	32:00:55.6	10.6	5833.4	1130.	1.0
5	3:27:37.7	30:11:35.3	10.2	623.2	376.	3.0
6	3:36:22.5	31:11:01.3	9.9	1594.1	656.	1.4
10	3:47:41.0	32:52:46.5	8.5	747.5	446.	2.1
12	3:30:25.5	30:26:35.0	7.2	540.2	372.	2.7
13	3:24:49.6	30:22:14.9	6.6	673.9	421.	2.3
14	3:39:27.1	31:22:24.3	6.7	2659.8	854.	1.1
15	3:28:35.3	30:18:48.9	6.4	305.4	286.	3.3
16	3:25:15.7	30:43:28.4	6.1	515.9	382.	2.3
19	3:28:58.3	30:44:17.2	5.9	410.1	359.	2.3
23	3:28:51.3	30:04:11.2	5.7	260.2	270.	3.4
24	3:28:48.5	30:33:09.3	5.7	170.1	221.	4.0

[a] Position of peak extinction within core (accurate to $2.5'$).

[b] Peak extinction, mass, radius, and mean number density derived from Clumpfind (Williams, de Geus, & Blitz 1994) with several clumps further separated. See text for details.

Table 8.4. Average, maximum and minimum submillimetre clump properties in each extinction core.

Core [a]	# [b]	S_{850}			f_0			R_{eff}			T_{BE}			Conc			P_{BE}		
#	Clumps	Avg	Max	Min	Avg	Max	Min	Avg	Max	Min	Avg	Max	Min	Avg	Max	Min	Avg	Max	Min
1	15	2.7	9.3	0.4	0.4	0.9	0.2	30.	45.	15.	17.5	23.0	14.5	0.46	0.68	0.28	5.8	6.1	5.5
2	2	2.9	3.9	1.9	0.7	1.2	0.2	34.	36.	32.	19.1	22.7	15.5	0.50	0.75	0.24	5.7	5.8	5.6
3	12	1.9	6.2	0.5	0.4	1.2	0.2	27.	39.	17.	18.4	23.9	12.7	0.40	0.73	0.20	5.8	6.0	5.7
4	9	6.7	15.6	0.3	1.6	5.3	0.2	34.	48.	15.	18.9	24.8	13.5	0.62	0.84	0.30	5.9	6.1	5.6
5	4	2.6	3.4	1.0	0.3	0.5	0.2	34.	39.	24.	16.2	16.8	15.6	0.48	0.54	0.40	5.8	5.9	5.7
8	4	6.6	10.1	0.7	0.8	1.3	0.2	42.	53.	20.	18.6	19.9	17.0	0.58	0.79	0.28	5.7	5.9	5.6
10	2	1.1	1.1	1.1	0.3	0.3	0.2	24.	26.	22.	14.1	15.2	13.1	0.46	0.48	0.43	5.9	6.0	5.8
16	6	7.8	23.0	2.3	1.0	3.0	0.2	45.	61.	40.	19.8	24.0	15.9	0.59	0.84	0.26	5.6	5.7	5.5
29	1	1.3	1.3	1.3	0.2	0.2	0.2	29.	29.	29.	21.4	21.4	21.4	0.28	0.28	0.28	5.7	5.7	5.7

[a] Extinction core reference number. See Table 8.2

[b] Number of submillimetre clumps in each extinction core.

Appendix A

An Extinction Threshold for Protostellar Cores in Ophiuchus

A.1 Abstract

We have observed continuum emission at $\lambda = 850\,\mu$m over ∼4 square degrees of the Ophiuchus star-forming cloud using SCUBA on the JCMT, producing a submillimetre continuum map twenty times larger than previous Ophiuchus surveys. Our sensitivity is $40\,\mathrm{mJy\,beam^{-1}}$, a factor of ∼2 less sensitive than earlier maps. Using an automated identification algorithm, we detect 100 candidate objects. Only two new objects are detected outside the boundary of previous maps, despite the much wider area surveyed. We compare the submillimetre continuum map with a map of visual extinction across the Ophiuchus cloud derived using a combination of 2MASS and R-band data. The total mass in submillimetre objects is ~ 50 $\mathrm{M}_\odot$ compared with ~ 2000 $\mathrm{M}_\odot$ in observed cloud mass estimated from the extinction. The submillimetre objects represent only 2.5% of the cloud mass. A clear association is seen between the locations of detected submillimetre objects and high visual extinction, with no objects detected at $A_V < 7$ magnitudes. Using the extinction map, we estimate pressures within the cloud from $P/k \approx 2 \times 10^5\,\mathrm{cm^{-3}\,K}$ in the

less-extincted regions to $P/k \approx 2 \times 10^6\,\mathrm{cm}^{-3}\,\mathrm{K}$ at the cloud centre. Given our sensitivities, cold ($T_d \approx 15\,\mathrm{K}$) clumps supported by thermal pressure, had they existed, should have been detected throughout the majority of the map. Such objects may not be present at low A_V because they may form only where $A_V >$ 15, by some mechanism (e.g., loss of non-thermal support).

A.2 Introduction

Stars must form out of gravitationally bound substructures within a molecular cloud but how the substructures themselves form is strongly debated. Possible scenarios for this process range from the gradual release of magnetic support (Mestel & Spitzer 1956; Shu 1983; Nakano 1984; Shu, Adams, & Lizano 1987; Mouschovias & Ciolek 1999; Basu & Ciolek 2004), leading to a slow, regulated evolution of structure in the cloud, to violent dissipation through interacting waves (Scalo 1985; Mac Low & Klessen 2004 and references therein).

Rotational transitions of molecules have been important for tracing both substructures and motions within molecular clouds. Transitions that probe low densities in clouds (e.g., CO (1-0)) reveal widespread emission. Lines observed over low-density regions are themselves very wide, indicating the presence of non-thermal motions on large scales that are crucial to overall cloud support. Transitions that probe high densities (e.g., NH_3 (1,1)), however, reveal more localized pockets within clouds, i.e., dense cores. Lines observed in dense cores are narrower than those observed in lower-density regions, indicating that non-thermal motions are reduced on smaller scales, with a concomitant reduction of support (Barranco & Goodman 1998; Goodman et al. 1998). Dense cores are typically associated with embedded protostellar objects, suggesting that they are the gravitationally bound substructures from which stars form (Tachihara, Mizuno, & Fukui 2000; Di Francesco, André, & Myers 2004).

Although observations of transitions that probe high densities have been a reliable means to investigate the small scale substructures of molecular clouds related to star formation, observations of submillimetre continuum emission from such regions are an attractive alternative given the high sensitivities such observations have to mass. For example, large-format bolometer arrays on large submillimetre or millimetre telescopes have been used in recent years to map several pc^2 of nearby star-forming molecular clouds, revealing many substructures in high-density regions at high sensitivities and resolution (Motte et al. 1998; Johnstone & Bally 1999; Johnstone et al. 2000a, 2001). In these regions, the detected continuum emission primarily originates from cold dust grains and is almost always optically thin, so continuum maps reveal temperature-weighted column densities. These data have revealed numerous stellar-mass substructures within the molecular cloud cores whose mass distributions have similarities to the stellar initial mass function.

Most of the regions targeted for widefield submillimetre continuum mapping have been those known previously to contain dense cores and active star formation. Much of the surrounding regions of lower-density cloud have been ignored in these maps, in part to maximize sensitivities. Significant information about the development of substructures may exist in these regions, however, but has been overlooked as a result of this bias. For example, investigation of Orion B North (Johnstone et al. 2001) found all the substructure to be confined to the densest molecular core regions but did not have sufficient cloud coverage to provide explicit environmental constraints. To provide an unbiased view of substructures within nearby star-forming molecular clouds, we present here submillimetre continuum and infrared extinction maps of $\sim$4 square degrees of the Ophiuchus star forming cloud. These observations are part of a larger project, the CO-ordinated Molecular Probe Line, Extinction, and Thermal Emission (COMPLETE) project (Goodman 2004), to obtain and compare high quality molecular line, submillimetre continuum, and infrared extinction data over the extents of the nearby Ophiuchus, Perseus, and Serpens star-forming molecular clouds. (These clouds, as well as the

Lupus and Chamaeleon clouds and many isolated cores, being observed extensively as part of the near- to mid-infrared "From Cores to Disks" (c2d) Legacy survey of the Spitzer Space Telescope (Evans et al. 2003).) The data presented here represent about half of the entire extent of Ophiuchus that will be mapped in the submillimetre for COMPLETE but already they comprise a map that is an order of magnitude larger than those of Ophiuchus by Motte et al. (1998) or Johnstone et al. (2000a) (albeit at lower sensitivity) and they sample an order of magnitude in column density of the cloud.

In this Letter, we demonstrate that all substructures detected in the Ophiuchus cloud are confined to a small fraction of the submillimetre continuum map. Despite the tenfold increase in the area of Ophiuchus probed here, only two objects located off the edges of previous maps are detected. No obvious substructures are found below an $A_V = 7$. Moreover, almost all bright submillimetre objects are found in the most-opaque, densest part of the cloud where $A_V \geq 15$ mag although simple models suggest they would have been detected at our sensitivity throughout most of the map if they existed. Instead, a column density or extinction threshold for substructure formation, and thus star formation, may exist in Ophiuchus and possibly in other molecular clouds.

A.3 Observations and Results

The data were obtained using the Submillimetre Common User Bolometer Array (SCUBA; see Holland et al. (1999)) on the James Clerk Maxwell Telescope (JCMT) on Mauna Kea, Hawaii[1]. The area chosen to map consisted of ∼4 square degrees in western Ophiuchus where $A_V > 3$ and includes the well-known cores Oph A, B1, B2, C, and D at its southeastern corner. This area was divided up into 38

---

[1] The JCMT is operated by the Joint Astronomy Centre in Hilo, Hawaii on behalf of the parent organizations Particle Physics and Astronomy Research Council in the United Kingdom, the National Research Council of Canada and The Netherlands Organization for Scientific Research.

square fields each ∼400 square arcminutes in size. Each field was observed over the course of ∼1 hour using the "fast scan" observing mode of SCUBA where the sky is sampled at a Nyquist rate at 850 μm. Each field was scanned six times but at a different chopping amplitude and direction each time. The chop maps were converted into an image by applying the matrix inversion data reduction technique (Johnstone et al. 2000b). Note that by using a chopping secondary to map the region, the data are insensitive to emission on scales larger than a few times the chop throw, i.e., $>120''$. The fields were observed separately through queue mode scheduling throughout Semester 03A. Since each field was observed at different times and thus under different atmospheric opacities, the sensitivity in the final map varies from field to field but only by a factor of ∼1.5. The mean and rms of the 1 σ rms sensitivity for all fields is 40 mJy beam^{-1} and 20 mJy beam^{-1} respectively. Since the JCMT beam is $\sim 14''$ FWHM at 850 μm, the final map consists of $\sim 1.9 \times 10^5$ resolution elements, the largest number obtained so far in a single SCUBA map.

Extinctions derived from R-band star count data by Cambrésy (1999) were used for the northern half of the map while those derived from Two Micron All Sky Survey (2MASS; Skrutskie et al. (1997)) stellar reddening data by Alves et al. (2005) as part of COMPLETE were used for the southern half since public release data were available for those fields. Since 2MASS is an infrared survey, its data are better for probing the highly-extincted regions at which the R-band extinctions saturate, $A_V \approx 8$. Extinctions derived from R-band or 2MASS data over regions in common show a slight difference of less than 1 mag and a tight linear correlation until $A_V \approx 8$. The resolution of the extinction map depends on the densities of stars used to derive extinctions, but it should be only as low as $\sim 3'$ at the highest extinctions (see Lombardi & Alves 2001). The mean and maximum A_V over the surveyed area are 4.2 and 36.2 mag respectively.

A.4 Discussion

The $\lambda = 850$ μm continuum map of Ophiuchus can be used to locate the incidences of substructure (i.e., objects of size <120″) in the cloud. To locate objects within the map in an unbiased manner, the Clumpfind algorithm (Williams, de Geus, & Blitz 1994) was used to identify 100 sources of flux in the map of comparable size to the beam or larger to a 5 σ threshold in peak brightness. All but 2 of these objects are associated with previously identified substructure in the smaller map of Johnstone et al. (2000a) surrounding the known Oph cores (i.e., A–G; see also Motte et al. (1998)) Table 1 lists the names, positions, and fluxes of two objects not previously identified since they lie beyond the edges of earlier continuum maps. They reside in two new cores in Ophiuchus, which we name Oph H and Oph I following Motte et al. (1998). No infrared or X-ray sources toward either core are reported within the SIMBAD database.

Detections of substructure in Ophiuchus allow us to measure their mass and determine their location while the extinction map can be used to estimate the total cloud mass over the same area. The integrated flux from all substructure in the cloud is 250 Jy. Assuming a dust temperature $T_d = 15$ K, a dust opacity at 850 μm $\kappa_\nu = 0.02$ cm^2 g^{-1}, and a distance of 160 pc to Ophiuchus then 1 Jy = 0.20 M$_\odot$ (Johnstone et al. 2000a). Therefore, the amount of mass in substructures detected is $\sim$ 50 M$_\odot$. From the extinction data and assuming $\mathrm{N}_H/A_V = 2 \times 10^{21}$, the total amount of mass residing within the map area is $\sim$ 2020 M$_\odot$. The detected substructures, therefore, only account for ~2.5% of the total amount of mass residing in the map area. Table 2 shows the distribution of these masses with A_V, and reveals that significant mass in substructure is found only at $A_V > 15$ mag.

Cumulative mass calculations may be easily biased by a few massive objects, but this is not the case for our surveyed area. Figure A.1 plots the peak flux, total flux, and radius of each identified object versus the A_V at their respective positions. No bright objects are found at $A_V < 15$ despite the large cloud area and mass of that region. A similar result was obtained by Johnstone et al. (2001) for submillimetre objects in Orion B North. At high extinction the total mass in clumps is determined not by a single object but by an ensemble, although the Oph A core accounts for one quarter of the mass in compact objects. Comparison of the mass estimation in this paper with the results of Johnstone et al. (2000a) shows that a significant amount of mass (almost 50% of the submillimetre flux in compact substructure) in the earlier paper was removed by the flattening and filtering techniques, stressing the difficulty in obtaining proper flux baselines for chopped submillimetre maps.

What is the physical significance of having most of the detectable substructure only at $A_V > 15$ mag? A threshold in A_V may need to be exceeded for such objects to form. Alternatively, our observations may not have been sensitive enough to detect substructure in regions of low A_V, e.g. if such objects are larger or less dense than their more-embedded brethren. Here, we use a simple model to argue that such objects in locations of low A_V in Ophiuchus should have been detected by our observations if they indeed existed.

Within a molecular cloud, pressure increases with A_V. Following McKee (1989), the pressure at depth r is $P(r) = \pi\, G\, \bar{\Sigma}\, \Sigma(r)$, where $\bar{\Sigma}$ is the mean column density through the cloud and $\Sigma(r)$ is the column density measured inward from the cloud surface to depth r. Near the centre of the cloud, $\Sigma(r) \approx \Sigma(s)/2$, where $\Sigma(s)$ is the column density through the cloud at impact parameter s. Thus, pressure in the cloud at depth r can be approximated as $P(r)/k = 1.7 \times 10^4\, \bar{A_V}\, A_V(s)\ \mathrm{cm}^{-3}\,\mathrm{K}$, where $\bar{A_V}$ is the mean extinction through the cloud, $A_V(s)$ is the extinction through the cloud at impact parameter s, and adopting $A_V = (\Sigma/\Sigma_0)\,\mathrm{mag}$ where $\Sigma_0 = 4.68 \times 10^{-3}\,\mathrm{g\,cm}^{-2}$. Taking the mean extinction through the cloud as $\bar{A_V} \approx 4$ and the range of measured $A_V = 3 - 30$ mag, $P/k \approx 0.2 - 2 \times 10^6\,\mathrm{cm}^{-3}\,\mathrm{K}$. Although admittedly approximate, the value at the highest extinctions (e.g., the Oph cores) is similar to the $3 \times 10^6\,\mathrm{cm}^{-3}\,\mathrm{K}$ found by Johnstone et al. (2000a) from fitting stable Bonnor-Ebert (BE) sphere models (Bonnor 1956; Ebert 1955) to submillimetre objects in the Ophiuchus cores to estimate their masses, internal temperatures, and bounding pressures.

Pressure support for a molecular cloud must come from non-thermal sources like magnetic fields or turbulence. Most of the previously-detected submillimetre objects in Ophiuchus, however, were fit reasonably well by models of BE spheres supported internally entirely by thermal pressure (Johnstone et al. 2000a). A similar analysis holds true for Orion B North (Johnstone et al. 2001). Note that these fits should not be construed as evidence that the objects are in stable equilibrium, since dynamic entities produced in turbulent clouds can appear like BE spheres (Ballesteros-Paredes et al. 2003). Similarly, the condensed central regions of clumps evolving via ambipolar diffusion approach a similar, albeit flattened, profile (Basu 1997; Basu & Ciolek 2004). The BE sphere model, however, provides a lower limit for the critical mass and column density at which an object will become unstable to gravitational collapse since only thermal pressure is available to act as support. Aside from scaling relations, BE spheres are a one-dimensional family of objects defined only by the ratio of central density to surface density, $\lambda = \rho(0)/\rho(R)$, with larger λ implying a greater importance of self-gravity. BE spheres are stable against gravitational collapse if $\lambda < 14$. The mass and density scaling relations of a BE sphere with fixed λ are $M_{BE} \propto P^{-1/2}$ and $\Sigma_{BE} \propto P^{1/2}$.

Can stable objects exist in Ophiuchus where $A_V < 15$ mag and remain undetected in our data? The total submillimetre continuum flux S_{850} associated with a BE sphere is a measure of its mass, weighted by temperature. Thus, for BE spheres with a fixed value of λ, the submillimetre flux as a function of the bounding pressure (assuming that both κ_ν and T remain constant) is $S_{850} \propto P(r)^{-1/2}$ or $S_{850} \propto A_V(s)^{-1/2}$. Similarly, the peak flux f_0 measures the column density and should scale as $f_0 \propto A_V(s)^{1/2}$ and the radius $R \propto A_V(s)^{-1/2}$. The total flux, peak flux, and radius *increase* with increasing λ (until a gravitationally unstable BE sphere is produced).

In Figure A.1 the above BE sphere relations are overlaid (solid line) on the data to show that non-detections at $A_V = 10$ are incompatible with detections at higher A_V. That is, the lack of significant observed substructure at moderate A_V implies that no objects in these regions are dominated by self-gravity to the extent of those at higher extinction. Since the low A_V regions contain most of the cloud mass, the lack of such detected objects is not due to a lack of material. Also shown in Figure A.1 is the upper boundary for stable BE spheres (dashed-dotted line), assuming that the gas and dust temperature is $T = 15\,\mathrm{K}$. Unstable objects, those which are capable of collapsing to stars, are only found where $A_V > 17$.

How do these results fit with present theoretical models for star formation? If the dominant mechanism for molecular cloud support is magnetic pressure mediated by collisions between ions (which couple to the magnetic field) and neutrals then the timescale for ambipolar diffusion would be long in regions of high ionization, limiting the formation of significant substructure. Crutcher (1999) has shown that the typical magnetic field strength in a molecular cloud is strong enough to supply most, if not all, of the required support against collapse. McKee (1989) demonstrates that in the lower column density regions of molecular clouds, where the extinction to the cloud surface is $A_V < 4$, the interstellar radiation field is capable of maintaining such a high ion fraction. Following this reasoning, the total extinction through regions of the cloud where substructure exists should be $A_V > 8$. This prediction is in excellent agreement with our observations. The somewhat higher threshold A_V that we find is plausibly a result of the non-uniform structure of the molecular cloud. In the regions of high extinction where only cosmic rays are capable of maintaining an ionization fraction, ambipolar diffusion enables the growth of prestellar cores. Recent theoretical calculations show that MHD turbulence may shorten the timescale for ambipolar diffusion within the core by a factor of 3-10 (Fatuzzo & Adams 2002; Zweibel 2002), bringing the ratio of observed cores with and without stars into agreement with their expected lifetimes. Johnstone et al. (2000a) found that approximately half their submillimetre objects in Ophiuchus were associated with infrared emission[2].

An alternative model for the support of molecular clouds utilizes turbulent motions to supply 'non-thermal' pressure support (MacLow & Klessen 2004). Such motions are observed within molecular clouds via the widths of molecular transitions like CO $1-0$. Indeed, simple virial analysis models indicate that the observed linewidths are large enough to provide support of the cloud against collapse, assuming that the 'non-thermal' pressure is isotropic and uniform throughout the cloud (Larson 1981). For Ophiuchus typical linewidths are $\Delta V > 1.5\ \mathrm{km\,s^{-1}}$ (Loren 1989). Within turbulent clouds, the formation of substructure is due to intersecting waves, producing local density maxima, most of which are transient. Ballesteros-Paredes et al. (2003) showed that such features can look similar to BE spheres despite being non-equilibrium objects. It remains to be determined, however, how the formation of substructure depends on local conditions, such as the mean pressure. Naively one might expect that these objects should follow a similar scaling relation to BE spheres. Regardless of the exact nature of the scaling, it is difficult to understand how turbulent models can produce the sharp decline in observed objects found in this investigation.

Molecular clouds are likely influenced by both magnetic fields and turbulent motions. The SCUBA observations presented in this paper suggest an extinction threshold, which is compatible with the predictions of McKee (1989), preventing the formation of relevant substructure over the bulk of the cloud. Thus, observations of submillimtere structure in molecular clouds yield similar conclusions to surveys of the latter-stage embedded stars (Lada & Lada 2003). As with the embedded stars, most if not all of the submillimetre objects reside in highly extincted cores, account for about twenty percent of the total core mass, and have an IMF-like initial mass function (Motte et al. 1998; Johnstone et al. 2000a). Thus, clustered star formation appears limited to the densest regions of molecular clouds where turbulent motions and enhanced ambipolar diffusion are able to seed an

---

[2] The high sensitivity of the Spitzer c2d survey will likely change this fraction.

ensemble of prestellar cores.

The research of D. J. has been supported by an NSERC Discovery Grant. H. K. is supported by an NSERC graduate scholarship. This research has made use of the SIMBAD database, operated at CDS, Strasbourg, France.

Table A.1: Newly-Identified Ophiuchus Objects

Name	R.A. (J2000)	decl. (J2000)	Peak Flux (Jy beam^{-1})	Total Flux (Jy)	Radius ($''$)	Cloud A_V
H-MM1	16 27 58.3	-24 33 42	0.40	4.2	36	18
I-MM1	16 28 57.7	-24 20 48	0.30	2.7	32	7

Table A.2: Percentages of Totals in Ranges of Extinction

A_V	Cloud Area	Cloud Mass		Clump Mass		Mass Ratio
Range	(%)	(M$_\odot$)	(%)	(M$_\odot$)	(%)	(%)
0–36	100	2020	100	49.4	100	2.5
0–7	88	1380	68	0	0	0
7–15	9	400	20	3.1	6	0.8
15–36	3	240	12	46.3	94	19

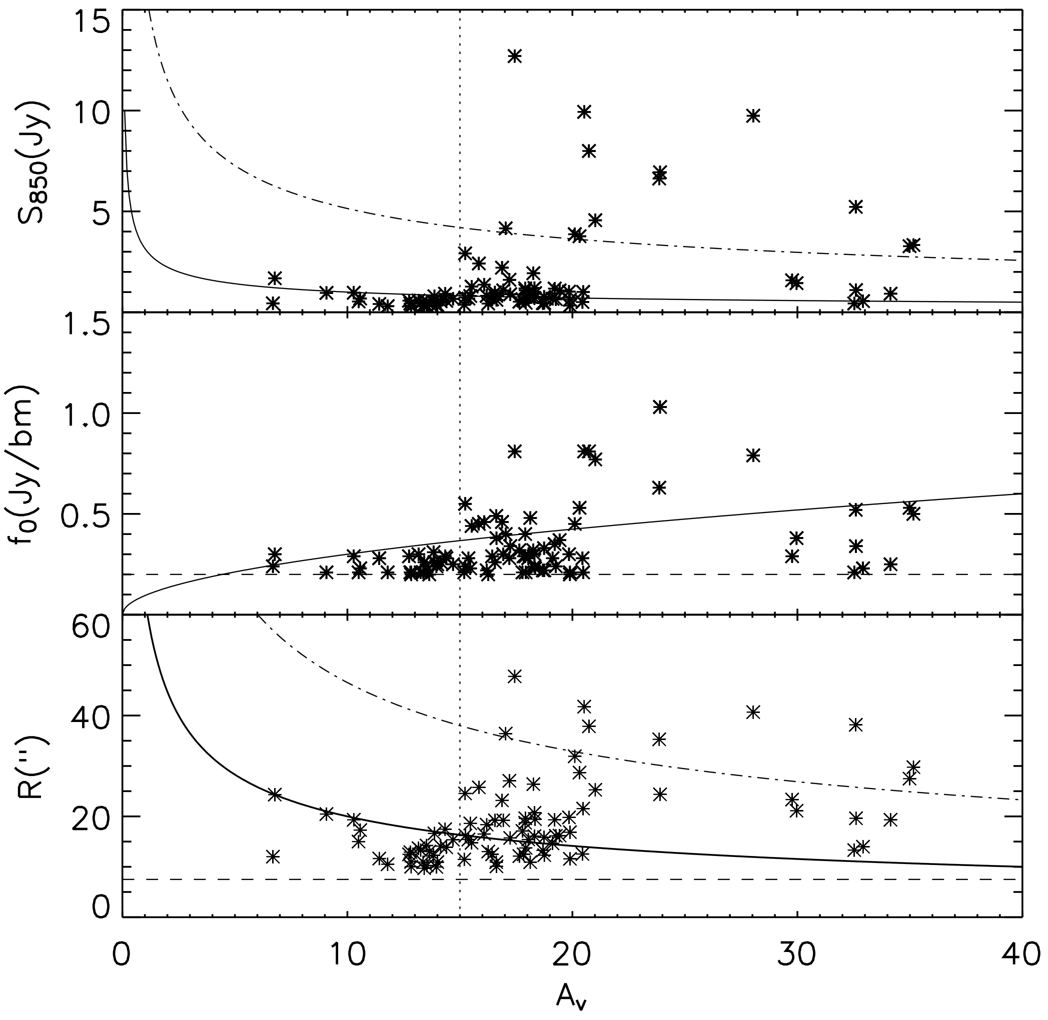

Figure A.1: Distribution of the observed properties of measured submillimetre clumps with cloud extinction. Panels from top to bottom show for each clump the integrated flux, peak flux, and size. Horizontal dashed lines denote sensitivity and resolution limits while vertical dotted lines at $A_V = 15$ mag mark the boundary of observed bright objects. The solid lines show the expected evolution with A_V of a BE sphere with a fixed value of λ but only marginally observed at $A_V = 10$ mag (see text). The dash-dotted lines show the upper limit for size and mass of stable BE spheres ($T = 15\,\mathrm{K}$) as a function of A_V.

Appendix B

Multiple Outflows and Protostars in Barnard 1

B.1 Abstract

Using optical (Hα & [SII]), Near-IR (H_2 & K_S), and submillimeter (850 μm & 450 μm) data, we have examined the region surrounding the Barnard1 (B1) core and found a multitude of new shocks from protostellar outflows. We trace several flows, some of which are large, parsec scale outflows with dynamic ages of order 10^4 yr, indicating that star formation has been taking place in Barnard 1 for at least that long. We can confidently identify eight protostars which are driving outflows. Of those eight protostars, one source, SMM 2 (SMMJ 033330+31095) is a new class-0 source, giving B1 a total of 3 class-0 protostars. Based on the number of shocks and protostars in this region, B1 appears to be a much more active region of star formation than previously thought. The number of shocks is comparable to or greater than those of other active star forming regions in Perseus (e.g. IC 348, L1455, & L1448).

B.2 Introduction

Star formation is usually accompanied by bipolar outflows which can be traced by optical emission lines as Herbig-Haro (HH) objects (for a review see Reipurth & Bally 2001). New large format, wide field CCDs are enabling the study of how outflows shape molecular clouds and influence the process of star formation. Shocks from outflows heat, dissociate, and ionize the gas. They also inject kinetic energy and momentum into the cloud which may drive turbulence and affect the rate of gravitational collapse of cores within these clouds (e.g. Leorat, Passot, & Pouquet 1990). Chains of HH objects and/or H_2 shocks often trace internal working surfaces in parsec scale outflows (Reipurth & Bally 2001). Their locations and orientations, together with their morphology, indicate the presence of embedded protostars. Outflows may play a fundamental role in the evolution of star forming molecular clouds, turbulence generation, and cloud destruction.

The Barnard 1 (B1) cloud lies on the eastern rim of a $\sim$1 degree diameter cavity in the Perseus Molecular Cloud. On the western edge of this cavity lies NGC 1333, the most active region of current star formation in the Perseus Molecular Cloud. The southern edge of this cavity includes the L1455 region which is also actively forming stars. Walawender, Bally, & Reipurth (2005) have speculated that the formation of this cavity has triggered star formation in the compressed gas making up its walls.

There are several measurements of the distance to the Perseus Molecular Cloud: Herbig & Jones (1983) adopted a distance of 350 pc to the western end of the cloud containing NGC 1333 while Cernis (1990) argued for a distance of 220 pc. Herbig (1998) adopted a distance of 316 pc as the distance to the IC 348 cluster associated with the eastern end of the Perseus Cloud. The Spitzer Legacy program Cores to Disks (c2d, Evans et al. 2003) has adopted a distance of 320 pc following measurements by de Zeeuw et al. (1999). For calculations in this paper, we will also use a distance of 320 pc.

The wide-field Hα, [SII], and i-band survey of the Perseus cloud (Walawender, Bally, & Reipurth 2005) revealed a large concentration of HH objects along the western rim of the Perseus cavity (a cavity in the CO gas distribution which lies between NGC1333 and B1). Several parsec scale chains radiate from the B1 core, pointing to a large concentration of embedded protostars in this region. There are additional HH objects in or near the rim of the Perseus cavity southwest of B1 including a cluster of activity surrounding IRAS 03276+3022. In this paper we will confine our discussion to the region which is roughly North and East of IRAS 03282+3035, leaving discussion of the activity around IRAS 03276+3022 for a future paper.

The B1 cloud has been well studied in molecular line radio maps (e.g. Bachiller & Cernicaro 1984; Ungerects & Thaddeus 1987; Bachiller, Menten & del Rio-Alvarez 1990). The cloud core is roughly 2 pc by 5 pc in size and has a mass of approximately 1200 $M_\odot$. B1 is one of only a few dark clouds with a measurement of it's magnetic field. Goodman et al. (1989) measured the magnetic field around IRAS 03301+3057 using the Zeeman effect and found $B_{los} = -27 \pm 4\mu G$.

Matthews & Wilson (2002) studied the polarization of submillimeter emission from the core of B1. They found evidence for an ordered magnetic field across the main core of B1 which has a position angle of roughly 90° East of North. Of the four clumps in the core of B1 (B1-a, B1-b, B1-c, and B1-d, following the nomenclature of Hirano et al. 1999; our SMM 6, SMM 1, SMM 2, and SMM 3 respectively), the two brightest (B1-b and B1-c) exhibit different mean position angles of polarization than the rest of the region.

Several young stars are known to exist in this region (Ladd, Lada, & Myers 1993; Cohen & Kuhi 1979). Bachiller, Menten & del Rio-Alvarez (1990) searched for high velocity CO emission around six young stellar objects (LZK 21 / IRAS 03295+3050, LkHα 327 / IRAS 03304+3100, LkHα 328, IRAS 03292+3039, IRAS 03301+3111, & IRAS 03301+3057). Only one source, IRAS 03301+3057 showed any evidence of high velocity gas. Hirano et al. (1994) and Hirano et al.

(1997) studied the high velocity CO gas around this source and concluded that it is driving a bipolar outflow which is observed pole-on.

IRAS 03282+3035 lies about 1 degree to the southwest of the main B1 cores. Bachiller, Martin-Pintado, & Pleanesas (1991) found a collimated, bipolar CO outflow emanating from this source with a terminal velocity of about 70 km s^{-1} and a length of 0.5 pc giving it a dynamic age of $\sim 10^4$ yr.

Alten et al. (1997) discovered HH 356 in the Northern portion of B1. Yan et al. (1998) found 5 HH objects in the B1 region (HH 429-433), however, they could not conclusively connect most of them with sources because of their distribution and uncertain morphologies.

B.3 Data Acquisition and Reduction

Visible wavelength images were obtained as part of an NOAO Survey Program and were described in Walawender, Bally, & Reipurth 2005. The central 36′ field of B1 received a total integration time of 1000 seconds in the narrowband filters (Hα and [SII]) and 90 seconds in the broadband SDSS i′ filter. Outer parts of B1 received 400 seconds and 30 seconds of exposure time respectively.

Near IR images were obtained on the nights of 2005 January 28 and 30 with the NIC-FPS near infrared imager on the f/10 naysmith focus of the 3.5 meter ARC telescope at Apache Point Observatory. NIC-FPS uses a Hawaii-1RG detector with 1024×1024 pixels with a pixel scale of 0.27″ pixel $^{-1}$ and a field of view 4.6′ on a side. A narrowband filter centered on the 2.12μm S(0) line of H_2 with an 0.4% bandpass was used for the molecular hydrogen observations and a K-short filter was used for continuum observations. Each of the pointings in the deep survey received a total integration time of 720 seconds in the narrowband filter and 60 seconds in the broadband filter. Some pointings at the periphery of the IR survey received only a third of the integration time per field.

The submillimeter data from SCUBA was taken from the JCMT[1] archives, run by the CADC[2]. The 850 and 450 μm data were first flat-fielded and extinction corrected using the standard SCUBA software (Holland et al, 1999). We then applied the matrix inversion technique (Johnstone et al, 2000) to convert the two data sets into images with pixel sizes of 3 arcsec. The 850 μm map has an intrinsic beamsize of 14 arcsec, however, it was convolved with a $\sigma = 1.5$ pixel (4.5 arcsec) gaussian to aid in the reduction of pixel noise, producing an effective 17.6 arcsec beam. Similarly, the 450 μm map has an intrinsic beamsize of 8.5 arcsec, and was convolved with a $\sigma = 1$ pixel (3 arcsec) gaussian, yielding an effective beamsize of 10.6 arcsec.

Structure on scales several times larger than the chop throw (>120 arcsec) may be an artifact of the image reconstruction (this is independent of reconstruction technique; Johnstone et al, 2000a), and so we also removed these from the map. This was done through the subtraction of a map convolved with a sigma of 90 arcsec. To minimize negative "bowling" around bright source, all points with values outside of ± 5 times the mean noise per pixel were set to those values before convolution. The noise in the 850 μm map is ~ 6 mJy bm^{-1} and ~ 40 mJy bm^{-1} in the 450 μm map. We identified twelve submillimeter clumps in the 850 μm map using the 2D version of Clumpfind (Williams et al. 1994). Hatchell et al. (2005) also studied the clumps in B1 and their clump properties are similar to ours. The locations and names of the clumps along with the Hatchell et al. (2005) designations are provided in Table 1. The observed and physical properties of these clumps are presented in Table 2.

A useful parameter for classifying the clumps is the degree to which they are

---

[1] The JCMT is operated by the Joint Astronomy Center in Hilo, Hawaii on behalf of the parent organizations Particle Physics and Astronomy Research Council in the United Kingdom, the National Research Council of Canada and The Netherlands Organization for Scientific Research.

[2] Guest User, Canadian Astronomy Data Center, which is operated by the Dominion Astrophysical Observatory for the National Research Council of Canada's Herzberg Institute of Astrophysics.

centrally condensed. This parameter can be easily found using the values obtained by Clumpfind. Following Johnstone et al. (2001), the total flux (F), peak flux density (S) and effective radius ($\mathrm{R_{eff}}$) combine to measure the concentration of a clump; $\mathrm{C} = 1 - \frac{\mathrm{F}}{\pi \mathrm{R_{eff}^2\, S}}$. This parameter can be physically interpreted in the context of the Bonnor-Ebert sphere model (Bonnor 1956; Ebert 1955; Hartmann 1998) where thermal support within the clump balances self-gravity and external bounding pressure. Stable Bonnor-Ebert spheres can only exist for concentrations below 0.72 (Hartmann 1998); objects possessing higher concentrations require additional support (e.g. from turbulence or magnetic fields) or else they will collapse. At the other end of the concentration spectrum, a uniform density sphere has a concentration of 0.33. Clumps with concentrations below this value are likely poorly defined or not in equilibrium. Since the concentration gives a measure of the importance of self-gravity within an object, one would expect that objects with a higher concentration (especially near or above 0.72) would generally be more evolved than their lower concentration counterparts.

We can estimate the internal dust temperature clump by modeling each clump as a Bonnor-Ebert sphere. Following the procedure outlined by Johnstone et al. (2005), we assume that each clump is in equilibrium, supported against gravitational collapse by an equal amount of thermal and non-thermal turbulent pressure. Conversion between the observed total flux and mass requires knowledge of both the dust opacity at 850 μm, which we take to be $\kappa = 0.02\ \mathrm{cm^2 g^{-1}}$, and the distance to B1 which we take to be $d = 320\,\mathrm{pc}$. The resulting temperatures range from 15 to 21 K. An alternate estimate for the clump temperatures can be derived from the ratio of flux found at 850 and 450 μm. To prevent misleading results from the differing beam sizes at these two wavelengths, we first convolve the image at each wavelength with the estimated beam of the other wavelength (see Reid & Wilson (2005) for the procedure and the beam parameters). Assuming that the dust opacity follows a power-law with index $\beta = 2$, we estimate temperatures ranging from 8 to 23 K. Significant uncertainty remains for each of these temperature measures and thus we adopt a 'typical' dust temperature of 15 K in order to measure the mass associated with each clump. Thus, the conversion from 850 μm total flux in Janskys to clump mass, in Solar masses, is 0.8. Table 2 lists the mass of each clump.

B.4 Results

The SCUBA map of B1 (Fig. 1) shows that the dust is distributed in a NE-SW oriented filament with the dense clumps SMM 1 (SMMJ 033336+31075)[3], SMM 2 (SMMJ 033330+31095), and SMM 3 (SMMJ 033327+31069) near the head. The position angle of this filament (PA $\sim 45°$) corresponds to the position angle of the cometary cloud in L1451 of Walawender et al. (2004) to within 1 degree. Walawender et al. (2004) concluded that this cometary cloud was shaped by soft UV radiation from the star 40 Per which lies North of IC 348. It is possible that the dust in B1 was also shaped by the same radiation field.

The visible wavelength images revealed 20 new HH objects in the region (see Walawender, Bally, & Reipurth 2005) bringing the total number of HH objects in B1 to 26. Many of these HH objects are faint and their morphology is unclear. Some are as much as tens of arcminutes from the nearest IRAS source or submillimeter clump, indicating that parsec scale outflows must exist in this region. The dynamic age of a 1 pc flow, assuming an outflow velocity of 100 km s^{-1} is about 10,000 years, indicating that star formation has been taking place in B1 for at least that long. It is difficult to associate HH objects with embedded young stars solely on the visible wavelength images. Furthermore, in confused regions such as the B1 core, it can be difficult to link individual shocks to specific large scale outflows.

---

[3] For clarity we will refer to the submillimeter clumps in the text as SMM 1 through SMM 12 (see Table 1). More formal designations are based on the J2000 coordinates: SMMJ hhmm.mmdddmm.m (e.g. SMMJ 033336+31075). We will note this designation at the first mention in the text of any particular clump. In addition, Table 1 contains both designations.

Near IR images of the core of B1 reveal a previously unknown complex of bright shocks (MH 1 & 2)[4] which have no optical counterparts (Fig. 2). There are also several other fainter molecular hydrogen shocks which have no optical counterparts (Table 3) and some molecular hydrogen shocks correspond to optically visible HH objects (Table 3). Most of the molecular hydrogen shocks are extremely faint, indicating the necessity of deeper H_2 imaging of this region. We describe the morphology and possible flow associations of individual shocks in the appendix.

Using the morphology of the shocks in the optical and near-IR images, we have linked several shocks into large scale flows and associated them with specific protostars identified in the submillimeter map or in the IRAS point source catalog (see appendix A). We identify a total of ten young stellar objects (YSOs) in Barnard 1. Eight of these power outflows made visible by optical or near-IR shocks. The other two (B1-bN and B1-bS of Hirano et al. 1999) lie in a confused region of the core of B1 and we are thus unable to confidently associate any shocks with these sources. Other IRAS sources and submillimeter clumps exist in this region and may represent additional protostars, however, we are unable to clearly link any outflow activity with those objects.

In the Barnard 1 core, we can confidently identify 6 protostars (LkHα 327, SMM 2, SMM 6, SMM 11, B1-bN, and B1-bS) in a region approximately 0.5 pc across. This corresponds to a stellar density in the core of nearly 100 stars pc^{-3}.

Walawender, Bally, & Reipurth (2005) estimated that a solar mass star may inject 1-10 $M_\odot$ km s^{-1} of momentum into the surrounding cloud over its life. If Barnard 1 contains of order a few hundred to a thousand solar masses of molecular material with a turbulent velocity of order one kilometer per second, that gives it a turbulent momentum of $\sim 10^3$ $M_\odot$ km s^{-1}. The 10 protostars identified in this paper are clearly insufficient to have an impact on the turbulent momentum of the cloud. Walawender, Bally, & Reipurth (2005), however, speculate that in

---

[4] Shocks which are visible in H_2 but have no optical counterpart can not be assigned HH numbers. In this paper we will refer to them as MH N, numbered roughly in order of brightness.

star forming cores, collapse may progress until sufficient stars form to disrupt the gas dynamics, thus halting collapse and regulating star formation. If this is the case, then Barnard 1 may represent a core in the early phases of collapse and the nearby NGC1333 cluster with its virulent star formation and outflow activity may represent a more advanced stage.

Clumpfind found twelve clumps in our SCUBA map. Of those twelve, six contain protostars. If we compare the properties of the submillimeter clumps containing protostars to those which do not contain protostars (Table 2), some interesting trends emerge. The concentration of the clump seems to be a good indicator of whether or not it contains a protostar. All of the clumps which have concentrations greater than 0.75 contain protostars (SMM 1, SMM 2, SMM 5, & SMM 7). The SMM 3 clump with a concentration of 0.58 may contain a protostar, but we can not conclusively associate any shocks or outflow activity with it because it lies in the confused core of B1. The MH 5 shock, however, lies nearby and its morphology suggests that SMM 3 may be the source. Two of the four clumps with concentrations between 0.4 and 0.5 contain protostars and none of the clumps with concentrations below 0.4 appear to contain protostars.

The correlation between total flux of a clump and whether it contains a protostar is somewhat less clear, but there does appear to be a correlation. Of the 7 brightest clumps, 5 contain protostars and one (SMM 3) is uncertain. Of the five faintest clumps, only one contains a protostar.

B.5 Summary

Using multiwavelength data: 850 & 450 micron SCUBA dust continuum, near-IR (H_2 & Ks) imaging, and visible wavelength (Hα, [S II], & SDSS i′) widefield imaging, we have examined the region surrounding the B1 core and found a multitude of new shocks from protostellar outflows. Though we are unable to confidently link many of the shocks into individual flows, we can trace several flows, some of which are large, parsec scale outflows with dynamic ages of order 10^4 yr. We can confidently identify eight protostars which are driving outflows (in addition to two class-0 sources identified by Hirano et al. 1999). Of those eight protostars, one (SMM 2) is a new class-0 source, giving B1 a total of 3 class-0 protostars.

The concentration we measure for submillimeter clumps is approximate since SCUBA's beam size is a significant fraction of the clump size, however, there appears to be a good correlation between the concentration of a submillimeter clump and whether it contains a protostar. All of our clumps with concentrations higher than 0.75 contain a protostar and about half of those with concentrations between 0.4 and 0.75 contain protostars. Our results are consistent with interpreting concentration as a measure of stability – i.e. clumps with high concentrations are likely to be unstable to collapse.

Based on the number of shocks and protostars in this region, B1 appears to be a much more active region of star formation than previously thought. The number of shocks is comparable to or greater than those in other regions of active star formation in Perseus: IC 348, L1455/L1451, & L1448. Only the NGC 1333 region in Perseus contains substantially more star formation activity.

B.6 Acknowledgments

The research of D.J. is supported through a grant from the Natural Sciences and Engineering Research Council of Canada. H.K. is supported by an NSERC PGSA fellowship and a National Research Council of Canada GSSSP award. The JCMT is operated by the Joint Astronomy Centre on behalf of the Particle Physics and Astronomy Research Council of the UK, the Netherlands Organization for Scientific Research, and the National Research Council of Canada. The authors acknowledge the data analysis facilities provided by the Starlink Project which is run by CCLRC on behalf of PPARC.

Based in part on observations obtained with the Apache Point Observatory

3.5-meter telescope, which is owned and operated by the Astrophysical Research Consortium.

B.7 Appendix

B.7.1 Individual Protostars in Barnard 1

SMM 2: This source powers the bright H_2 shock system MH 1 & 2 (Fig. 2). There is no IRAS counterpart to SMM 2 indicating that it may be a very young protostar which is deeply embedded. Each lobe of the outflow extends $\sim 200''$ to either side of the submillimeter clump. Assuming a 100 km s^{-1} outflow velocity, this gives a dynamic age of the flow of about 3000 yr, consistent with our interpretation of the protostar as a young class-0 source.

The polarization observations of Matthews & Wilson (2002) show a strong flattening of the p versus I relation in this core (B1-c using their nomenclature). They suggest that "this is usually attributed to either changing grain or alignment physics with increasing density or varying ... magnetic field geometry." They speculate that if SMM 2 (their B1-c) is a starless core (and thus no disk or outflow is present), then the field in the core may have a straight geometry. Our observations, however, show that SMM 2 contains at least one protostar which drives a bipolar flow.

Matthews & Wilson (2002) measured the polarization position angle for SMM 2 to be $\sim 35°$, lying roughly along the semi-minor axis of the extended emission surrounding the clump. Thus the magnetic field, which is expected to be perpendicular to the polarization angle, should have a position angle of $\sim 125°$. The outflow axis has a position angle of $\sim 115°$, thus we conclude that the magnetic field may have influenced the geometry of the protostellar source and its jet.

Matthews, Hogerheijde, & Bergin (2005) have studied SMM 2 (B1-c) using BIMA looking at dynamics, abundances and the molecular outflow/envelope interaction. In addition, they detect the outflow from SMM 2 in Spitzer Space Telescope IRAC images.

IRAS 03304+3100 / LkHα327: This source appears to drive a flow consisting of HH 432, HH 788, & MH 7 (Fig. 2). It may also be the driving source for HH 433, 791, 793, & 794 to the southeast and HH 430 to the northwest, though this is unclear. This source lies at the edge of the dense core of B1 and is bright in optical images ($m_B \sim 15$) and does not correspond to any SMM clump. The IRAS luminosity of this source is 1.77 $L_\odot$ and the 12 to 100 micron slope is consistent with a class-I source.

SMM 6 / IRAS 03301+3057: The SMM 6 (SMMJ 033328+31078) source is invisible in our SDSS i′ image, however, it shows up in the near-IR images (Fig. 2). It appears to power a string of H_2 knots to the West designated MH 4. The Ks image shows a small reflection nebula extending $\sim 8''$ to the southwest, about 45° misaligned from the line of H_2 knots.

Hirano et al. (1997) detected a high velocity CO outflow from the IRAS 03301+3057 source which they concluded was an outflow seen pole-on. In examining our SDSS i′ images and the POSS plates of this region, we do not see a "faint red object" at the position reported by Hirano et al. (1997). There is a faint object about $80''$ North of the position of IRAS 03301+3057 (rather than the $7''$ reported by Hirano et al. 1997). This object corresponds to HH 431, not a reflection nebula.

The IRAS luminosity of IRAS 03301+3057 is 2.37 $L_\odot$ and the 12 to 100 micron slope is consistent with a class-I source. The 2MASS magnitudes are: $m_J = 18.1$, $m_H = 16.1$, & $m_K = 14.2$.

SMM 11: SMM 11 (SMMJ 033346+31071) is invisible in our SDSS i′ image, however, it shows up faintly in the near-IR images (Fig. 2). This source is not in the 2MASS point source catalog. The Ks image shows a faint, filamentary reflection nebula extending about $45''$ to the South and East. The star itself is much brighter in the H_2 filter than in the Ks filter and is surrounded by faint, filamentary H_2 emission.

B1-bN & B1-bS / SMM 1: These two sources, identified by Hirano, et al. (1999) as class-0 protostars have no IRAS counterparts, but are coincident with our SMM 1 clump, the brightest submillimeter clump in our map which shows elongation along the same axis as the separation of these protostars (Fig. 2). Hirano et al. (1999) estimate that these protostars have masses of about 1.6-1.8 $M_\odot$ and $L_{bol} = 2.6 - 3.1\ L_\odot$.

We can not confidently associate any optical or near-IR shocks with these flows, however, that is primarily because of the large number of shocks in the core of B1. The MH 5 shock is filamentary and may be driven, by one of these sources, but that is unclear.

IRAS 03293+3052: This source is a bright near-IR visible star with a bright reflection nebula visible in the Ks and H_2 filters (Fig. 3). There is also bright H_2 emission coincident with the source which may also be reflected light. There is some faint SMM emission, but it was not strong enough to be selected by Clumpfind as a clump. The IRAS luminosity of this source is 0.78 $L_\odot$ and the 12 to 100 micron slope is consistent with a class-I source. The 2MASS point source catalog contains two entries coincident with this object, probably because of its extended structure. The brighter of the two has 2MASS magnitudes of $m_J = 15.9$, $m_H = 14.0$, & $m_K = 12.6$.

IRAS 03295+3050: This source is coincident with an Hα bright C-shaped reflection nebula and jet (Fig. 3). There is a nearby ($\sim 25''$ away) bright star visible in the i$'$ image which is $25''$ from the nominal position of the IRAS source. This star, however, lies within the error ellipse quoted in the IRAS Point Source Catalog, so it may be the source star. The IRAS luminosity of this source is 0.52 $L_\odot$ and the 12 to 100 micron slope is consistent with a class-I source. The 2MASS magnitudes of this star are $m_J = 11.3$, $m_H = 10.1$, & $m_K = 9.4$.

SMM 7 / IRAS 03282+3035: SMM 7 (SMMJ 033135+30455) lies about $30'$ to the southwest of the main B1 core (Fig. 4). Bachiller, Martin-Pintado, & Planesas

(1991) found a high velocity molecular jet emerging from this source. Bally et al. (1993) found bright H_2 emission coincident with the blueshifted lobe of Bachiller, Martin-Pintado, & Planesas (1991). Our near-IR survey does not cover this source, but we did find the optical shock HH 773 about $2.6'$ from the source along the position angle of the jet. The IRAS luminosity of this source is 0.94 $L_\odot$ and the 12 to 100 micron slope is consistent with a class-I source.

SMM 5 / IRAS 03292+3039: SMM 5 (SMMJ 033230+30497) lies about $22'$ southwest of the core of B1 (Fig. 4). The tip of HH 782 lies about $12.5'$ southeast of the source and a faint [SII] filament points back toward the source. It appears that this source drives a $\sim$ 1.1pc flow, terminating in HH 782. The IRAS luminosity of this source is 0.82 $L_\odot$ and the 12 to 100 micron slope is consistent with a class-I source.

B.7.2 Optical and Near-IR Shocks

In the Core of Barnard 1

MH 1 & 2: The bright shocks MH 1 & 2 (Fig. 2) appear to be emanating from the SMM 2 clump which lies near the northeastern end of the dust filament visible in the SCUBA maps (Fig. 1). The shocks appear to extend to roughly the same distance on either side of the clump ($r \sim 12'$). The MH 2 shock has a much more complex and knotty structure than the MH 1 shock, implying that perhaps the flow is breaking out of the cloud on the MH 2 end.

HH 431 & 787: HH 431 (Fig. 2) is an Hα bright shock with a double lobed structure which is oriented along the axis defined by the HH 774, 775, and 783 flow. In the discovery paper, Yan et al. (1998) indicated that this object had a bow shock morphology, however, our deeper images indicate that the morphology is amorphous and may not be a bow shock. HH 787 is a diffuse, Hα dominated shock which also lies along the axis of the HH 774, 775, and 783 flow.

The SMM 2 clump lies approximately $1.3'$ to the NE of HH 431 along the

HH 774, 775, and 783 axis. We conclude, however, that the SMM 2 clump powers the MH 1 & 2 flow, thus we suggest that HH 431 and HH 787 are part of the northeastern extension of the HH 774, 775, and 783 flow which is powered by IRAS 03293+3052.

HH 432, 788, & MH 7: HH 432 lies just East of the main core of B1 (Fig. 2). Yan et al. (1998) concluded that HH 432 is a shock in a flow emanating from IRAS 03304+3100 (LkHα327). Our images support this conclusion, showing faint diffuse Hα emission which traces back from HH 432 toward that source. In addition, the MH 7 knot lies South of HH 432 and appears to be an extension of the flow. To the North and West, along the axis defined by HH 432, MH 7, and IRAS 03304+3100, lies HH 788, a compact Hα bright knot. It would appear that these three shocks define a NW-SE oriented flow driven by IRAS 03304+3100.

HH 433, MH 8, & 9: HH 433 is a large shock visible in both Hα and [SII] (Fig. 2). It lies South of HH 432 along the axis defined by IRAS 03304+3100 & HH 432, leading Yan et al. (1998) to conclude that it is part of the same flow. In our images, however,it appears to be linked to HH 790 through some diffuse Hα filaments and through MH 8 & 9. Thus, it is unclear if HH 433 is part of the LkHα 327 flow. The MH 8 shock is a filamentary structure coincident with one of the brighter knots of the Hα filament connecting HH 433 with HH 790. The MH 9 shock is a compact knot of H_2 emission, also coincident with an Hα knot.

HH 789: This compact Hα bright knot lies approximately 30$''$ North of the SMM 11 clump in the center of B1 (Fig. 2). We can not make a clearer association of this shock with other shocks or potential outflow sources.

HH 790: This object consists of a region of diffuse Hα emission and a more compact [SII] filament (Fig. 2). Both the Hα and [SII] filaments are oriented roughly SE-NW and may be emanating from the nearby SMM 11, SMM 1, or SMM 3 clumps in the core of B1. There appears to be a very faint H_2 bowshock in this area, but deeper imaging is necessary to confirm this.

MH 3 & 10: MH 3 (Fig. 2) is a bright H_2 shock, which looks like a bowshock emanating from IRAS 03301+3057 / SMM 6 to the southeast, however, there is a faint filament of emission which connects this shock to MH 10 to the East. In addition, the IRAS 03301+3057 source, appears to be launching a jet (MH 4) to the West. Thus, we tentatively conclude that MH 3 is part of a larger E-W oriented flow which passes through the center of B1 and which also includes MH 10.

MH 4: This bright H_2 shock (Fig. 2) is part of a short chain of shocks aligned nearly E-W emanating from IRAS 03301+3057. There also appears to be a small, elongated reflection nebula visible in the Ks filter which is oriented SW-NE, not parallel to the chain of shocks.

MH 5: This shock is a bright NE-SW oriented filament located in the very densest part of the B1 core (Fig. 2). There are several plausible sources for this shock including SMM 3 or the B1-bS or B1-bN sources of Hirano et al. (1999) which are part of SMM 1.

MH 11: A very faint, diffuse emission (Fig. 2) which needs to be confirmed with deeper H_2 observations.

MH 12: A star, visible in the Ks filter, but with extended H_2 emission surrounding the star (Fig. 2). The star is coincident with the SMM 11 clump which lies in the center of the B1 core.

HH 429, 781, 785: Originally discovered by Yan et al.(1998), HH 429 (see Walawender et al. 2005, Fig. 30) lies approximately 20′ West of the core of B1 (Fig. 1) and is clearly facing away from the core, indicating that this is likely the terminal bowshock in an E-W oriented flow emanating from one of the young stars in B1. HH 781 (see Fig. 1 & Walawender et al. 2005, Fig. 30) and 785 (Fig. 2) which lie between the B1 core and HH 429 are also likely part of this parsec scale flow. These three shocks define an axis pointing toward the core of B1, however, due to the multitude of sources and shocks in the core of B1 it remains unclear what other shocks are members of this flow or which source might be powering it.

HH 791, 793, & 794: These are a cluster of diffuse [SII] filaments (see Walawender et al. 2005, Fig. 30) which lie roughly 10′ South and East of the B1 core

(Fig. 1). They may define a large, low surface brightness bowshock at the end of the HH 433, MH 8 & 9, HH 790 chain. The may also define the terminal shock in the HH 432, MH 7 flow powered by IRAS 03304+3100.

The Southwest Potion of Barnard 1

HH 774, 775, and 783: This chain of shocks (Fig. 3) points toward the HH 770, 771, & 772 complex (see below) and may be the large scale flow which powers that bowshock. HH 775 has a filamentary structure in Hα which extends along a NE-SW axis which points toward HH 783 to the NE and HH 774 to the SW. HH 775 also has a faint H_2 counterpart. HH 783 coincides with IRAS 03293+3052 which may power this parsec scale outflow. The axis of this flow points back to the NE and may drive shocks near the core of B1 (see HH 787 & 431 below).

HH 784, 776, & MH 6: HH 784 is an Hα jet embedded in a C-shaped reflection nebula (Fig. 3) and is roughly coincident with IRAS 03295+3050. Positioned along the jet axis, equally spaced (r $\sim 4.2'$) on either side of the jet lie HH 776, an Hα bright shock and MH 6 a faint H_2 shock. The axis defined by the jet passes near the shocks in the core of B1, however, is is unclear whether this jet is powering any of those shocks. The jet axis also passes near HH 775, 774, and the HH 770, 771, 772 complex and is another candidate source for those shocks.

HH 770, 771, & 772: This trio of HH objects have a filamentary Hα structure (Fig. 4). HH 770 and 771 have bright [SII] knots. All three filaments are roughly NE-SW aligned and may represent a large, low surface brightness bowshock pointing back toward the core of B1. IRAS 03281+3039, however, lies only $2'$ from HH 770 and may be a young star.

HH 773: This faint [SII] knot (Fig. 4) lies roughly $2.5'$ SE of SMM 7 (SMMJ 033135+30455) which is coincident with IRAS 03282+3035. There are no other potential sources in this area, thus it is likely that HH 773 is driven by the SMM 7 / IRAS 03282+3035 protostar.

HH 782: This HH object has a long filamentary structure in the [SII] image (see

Fig. 5 & Walawender et al. 2005, Fig. 31). The filament is oriented NW-SE and lies in a relatively low extinction region. The filament, however, points directly back to SMM 5 which contains IRAS 03292+3039 and lies in a much higher extinction region. The most distant knot in HH 782 lies approximately 12.5′ from SMM 5, making this flow roughly 1.1 parsecs in length.

HH 786: This shock is a compact knot, brighter in Hα than [SII] (Fig. 3). It has a faint H_2 counterpart. IRAS 03295+3050 and IRAS 03293+3052 are 3.9′ and 6.3′ away respectively, but both appear to be driving flows which would not intersect this shock. Three small submillimeter clumps (SMM 8 / SMMJ 033273+30599, SMM 12 / SMMJ 033251+30600, & SMM 9 / SMMJ 033244+30590) lie nearby, but it is unclear whether any of these may contain a protostar which drives this shock.

The Northern Edge of Barnard 1

HH 430: This shock lies well to the North of the main core of B1 (Fig. 5). HH 430 lies 10.9′ and 10.4′ from SMM 10 (SMMJ 033322+31199) and IRAS 03301+3111 respectively. HH 430 is large, diffuse, brighter in [SII] than Hα, and has a diffuse H_2 counterpart. Yan et al. (1998) reported this object as having the morphology of a jet in their discovery paper. Our deeper images show this object is actually large and diffuse and not jet-like.

This object lies 19′ northwest of LkHα 327 / IRAS 03304+3100 along the same line as HH 788. In addition, the HH 791, 794, 793 shock complex lies about the same distance southeast of LkHα 327 along a line defined by LkHα 327 and HH 432. It is possible that LkHα 327 is powering a giant flow which stretches roughly 3.5 parsecs from the HH 791, 794, 793 complex to HH 430.

HH 356: This shock lies well to the North of the main core of B1 (Fig. 5). HH 356 lies 6.7′ and 5.3′ from SMM 10 and IRAS 03301+3111 respectively. The morphology of HH 356 indicates that it may be emanating from one of those two sources, or possibly IRAS 03303+3108 which lies 3.0′ southeast of SMM 10.

HH 356 is bright in Hα, [SII], and H_2.

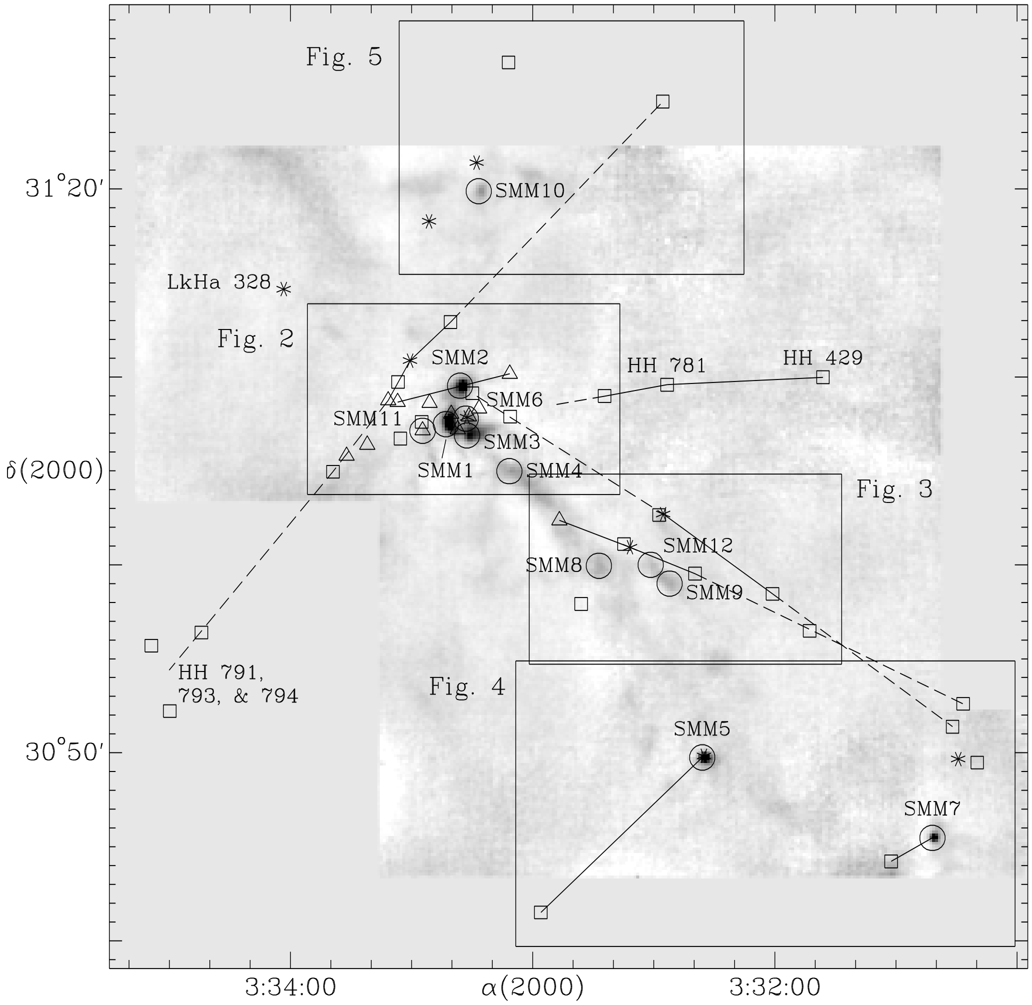

Figure B.1: Greyscale image of the 850 μm SCUBA map covering the entire Barnard 1 region. Boxes and triangles represent HH objects and H_2 shocks respectively. Asterisks represent IRAS sources. Submillimeter clumps are labeled. The regions shown in Figs. 2, 3, 4, & 5 are boxed and labeled.

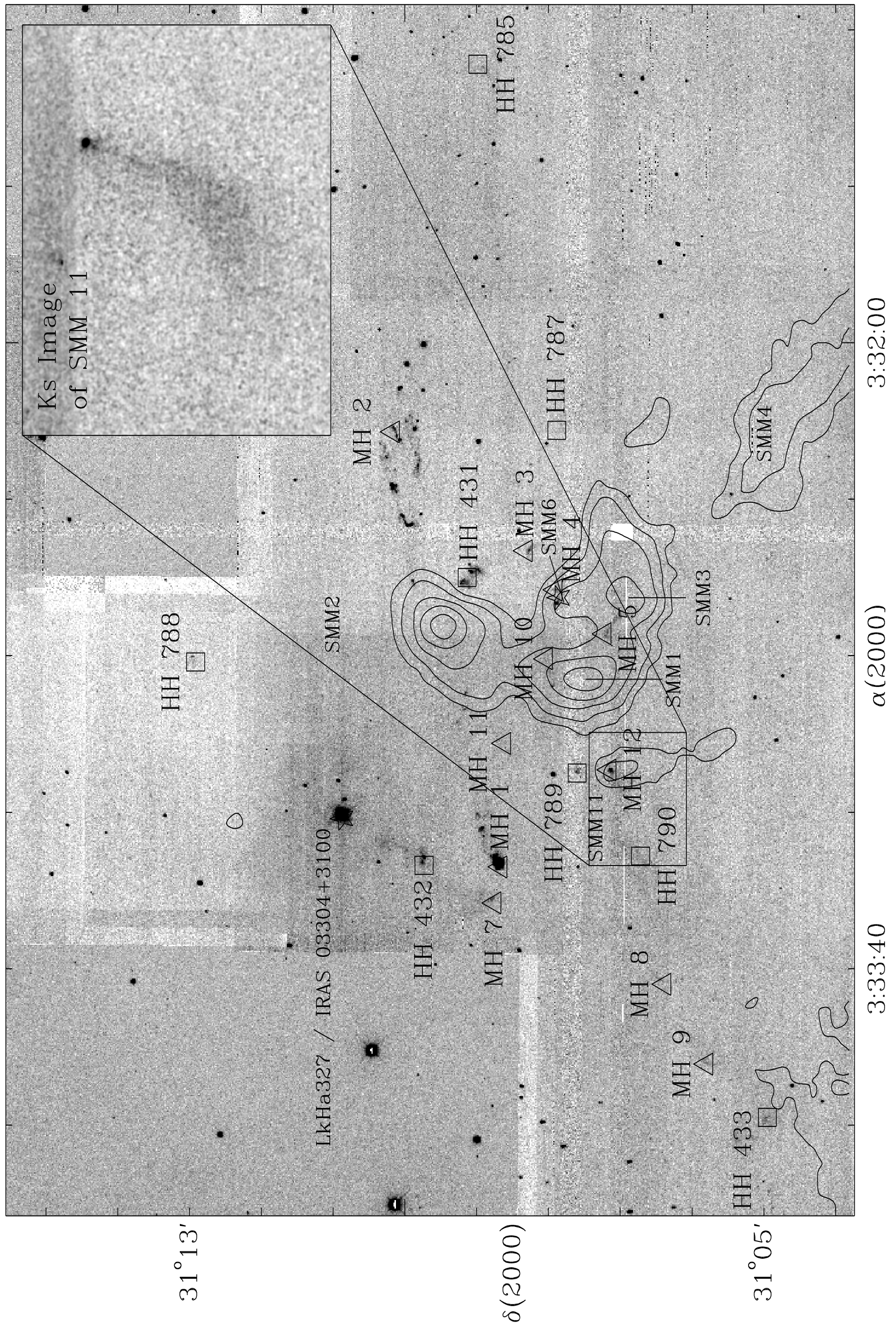

Figure B.2: An Hα + H_2 image of the core of Barnard 1. The contours show the 0.05, 0.1, 0.2, 0.4, & 0.8 Jy bm^{-1} flux boundaries from the SCUBA 850 μm map. Boxes mark HH objects, triangles mark the H_2 shocks. The inset shows the faint IR reflection nebula surrounding the star in SMM 11.

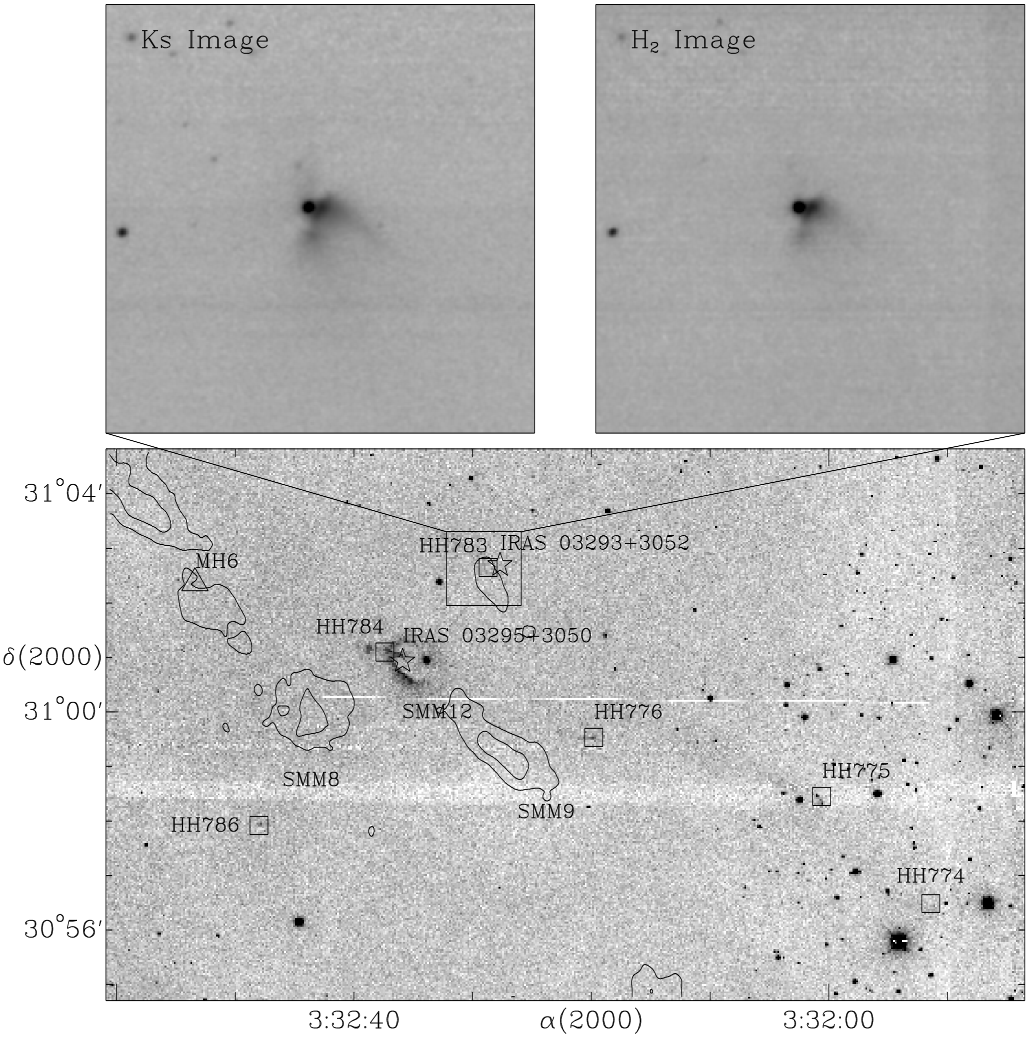

Figure B.3: An Hα image of the region southwest of Barnard 1. The contours show the 0.05 & 0.1 Jy bm^{-1} flux boundaries from the SCUBA 850 μm map. Boxes mark HH objects, triangles mark the H_2 shocks. The insets show the H_2 images of MH 6 and the reflection nebula around IRAS 03293+3052 respectively.

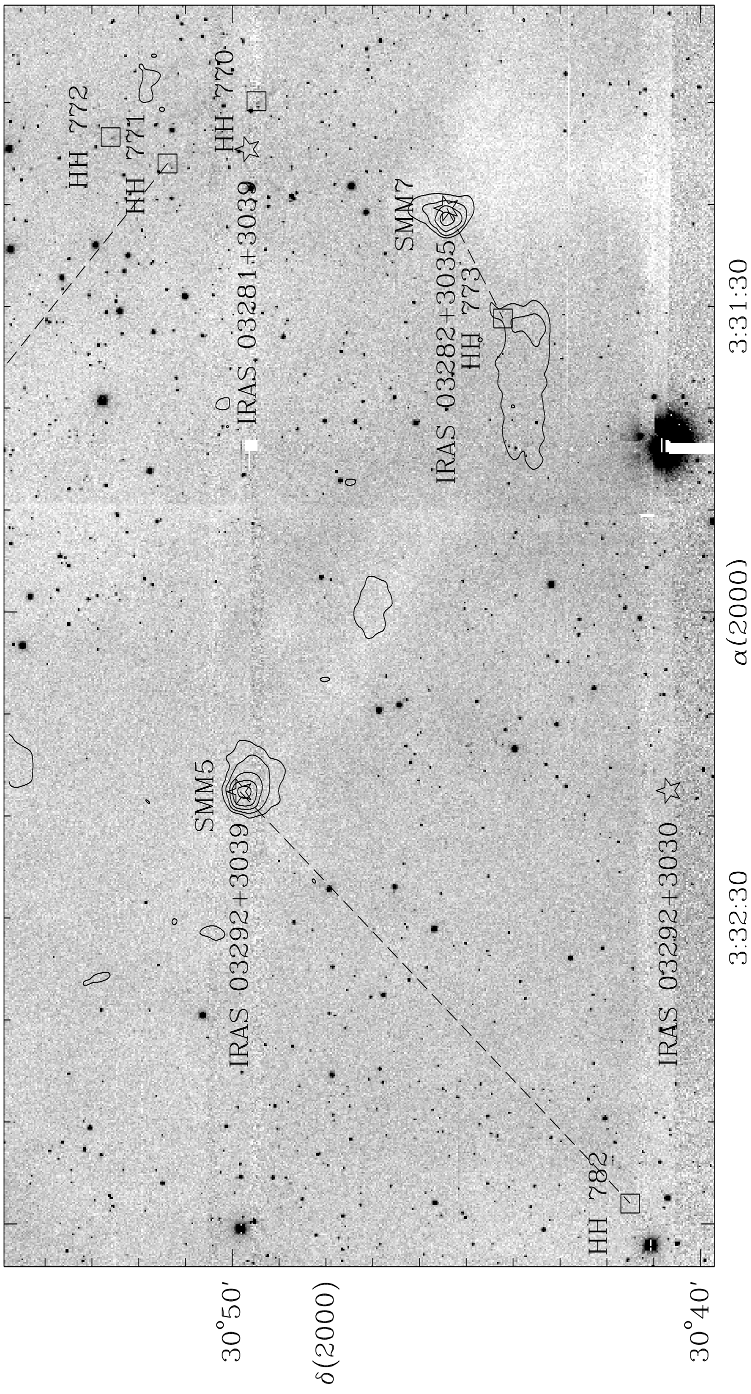

Figure B.4: An Hα image of the region south of the Barnard 1 core. The contours show the 0.05 & 0.1 Jy bm^{-1} flux boundaries from the SCUBA 850 μm map. Boxes mark HH objects, triangles mark the H_2 shocks.

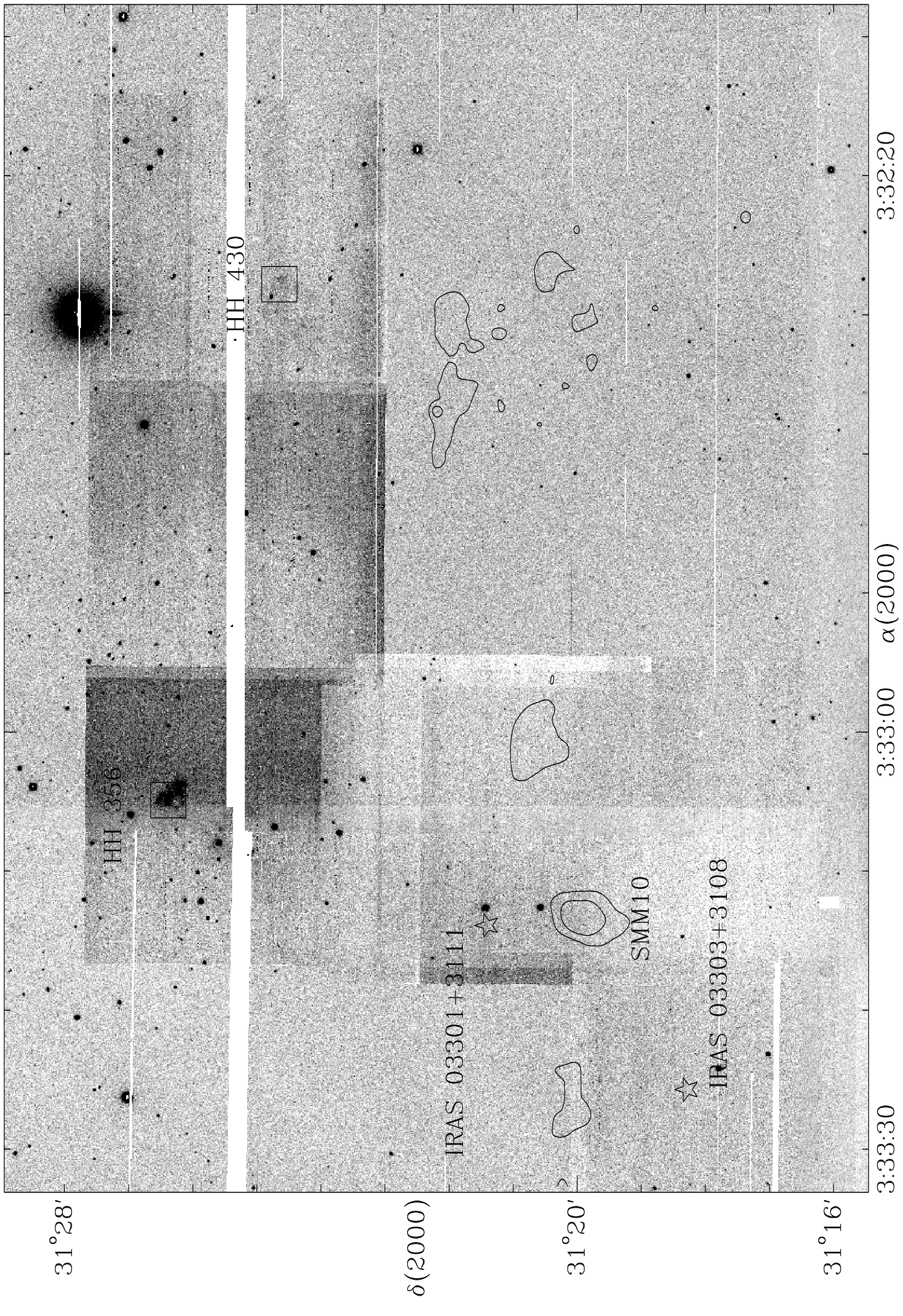

Figure B.5: An Hα + [SII] + H_2 image of the region north of the Barnard 1 core. The contours show the 0.05 & 0.1 Jy bm^{-1} flux boundaries from the SCUBA 850 μm map. Boxes mark HH objects, triangles mark the H_2 shocks.

Table B.1. Positions of SCUBA Clumps in the Barnard 1 Region.

Name SMM	Designation SMMJ	α (J2000.0)	δ (J2000.0)	Hatchell Name
1	033336+31075	$3^h33^m21^s.5$	$31^\circ07'29''$	2
2	033330+31095	$3^h33^m18^s.0$	$31^\circ09'32''$	1
3	033327+31069	$3^h33^m16^s.3$	$31^\circ06'53''$	4
4	033310+31050	$3^h33^m05^s.8$	$31^\circ04'59''$	6
5	033230+30497	$3^h32^m18^s.0$	$30^\circ49'45''$	76
6	033328+31078	$3^h33^m16^s.6$	$31^\circ07'47''$	7
7	033135+30455	$3^h31^m21^s.0$	$30^\circ45'28''$	77
8	033273+30599	$3^h32^m43^s.6$	$30^\circ59'57''$	...
9	033244+30590	$3^h32^m26^s.1$	$30^\circ59'00''$	89
10	033322+31199	$3^h33^m13^s.4$	$31^\circ19'53''$	82
11	033346+31071	$3^h33^m27^s.3$	$31^\circ07'08''$	10
12	033251+30600	$3^h32^m30^s.8$	$31^\circ00'00''$	89ext

Table B.2. Properties of SCUBA Clumps in the Barnard 1 Region.

Name SMM	Total Flux 850 μm (Jy)	Peak Flux[a] 850 μm (Jy/bm)	Total Flux 450 μm (Jy)	Peak Flux[b] 450 μm (Jy/bm)	Radius ($''$)	Conc.[c]	Mass[d] ($M_\odot$)	Protostar?
1	8.56	1.32	40.0	3.41	45	0.75	6.9	Y
2	7.30	1.44	39.2	5.01	49	0.84	5.8	Y
3	6.45	0.54	29.2	1.17	47	0.58	5.2	?
4	5.19	0.18	31.4	0.45	63	0.44	4.2	
5	4.62	1.53	16.9	2.84	39	0.85	3.7	Y
6	2.69	0.27	12.5	0.72	37	0.43	2.2	Y
7	2.05	0.78	4.05	2.20	29	0.76	1.6	Y
8	1.51	0.13	5.06	0.23	37	0.34	1.2	
9	1.30	0.13	11.8	0.52	33	0.29	1.0	
10	0.97	0.19	4.99	0.40	26	0.43	0.8	
11	0.51	0.15	1.43	0.35	21	0.40	0.4	Y
12	0.46	0.10	4.84	0.45	21	0.23	0.4	

[a] Peak flux within a beam of 17.6$''$

[b] Peak flux within a beam of 10.6$''$

[c] Concentration measure (see text)

[d] Mass derived from the total flux at 850 μm assuming $T_d = 15\,K$ and $\kappa_{850} = 0.02\,cm^2g^{-1}$.

Table B.3. Positions of H_2 Shocks in the Barnard 1 region.

Shock Label	α (J2000.0)	δ (J2000.0)	comment
MH 1	$3^h33^m33^s.5$	$31°08'40''$	Bright H_2 knot
MH 2	$3^h33^m05^s.7$	$31°10'10''$	Bright, complex H_2 shock system
MH 3	$3^h33^m13^s.3$	$31°08'19''$	H_2 bowshock, possibly emanating from IRAS 03301+3057
MH 4	$3^h33^m15^s.8$	$31°07'54''$	H_2 coincident w/ IRAS 03301+3057
MH 5	$3^h33^m18^s.6$	$31°07'13''$	H_2 filament possibly associarted with scuba core
MH 6	$3^h32^m53^s.4$	$31°02'22''$	Small H_2 shock, possibly from IRAS 03295+3050
MH 7	$3^h33^m35^s.8$	$31°08'45''$	Faint H_2 knot, possibly part of HH432
MH 8	$3^h33^m41^s.0$	$31°06'23''$	Faint arc between HH 790 and HH 433
MH 9	$3^h33^m46^s.1$	$31°05'48''$	Faint filament between HH 790 and HH 433
MH 10	$3^h33^m20^s.2$	$31°08'02''$	Filament of H_2
MH 11	$3^h33^m25^s.6$	$31°08'37''$	Diffuse filament of H_2
MH 12	$3^h33^m27^s.3$	$31°07'09''$	H_2 surrounding star
HH 775	$3^h32^m00^s.6$	$30°58'27''$	Small H_2 filament.
HH 430	$3^h32^m27^s.8$	$31°24'39''$	Diffuse H_2 associated with [SII] knot.
HH 786	$3^h32^m48^s.0$	$30°57'55''$	Faint H_2 knot ~ 15" from optical shock.
HH 356	$3^h33^m06^s.0$	$31°26'44''$	Three bright H_2 knots.
HH 789	$3^h33^m27^s.5$	$31°07'36''$	Compact H_2 knot coincident with optical shock.
HH 790	$3^h33^m32^s.8$	$31°06'43''$	Diffuse H_2 emission coincident with optical shock.
HH 432	$3^h33^m33^s.4$	$31°09'44''$	Knot of H_2 emission coincident with brightest Hα knot

Appendix C

Definition of Frequently Used Symbols

A_V	magnitudes of extinction
BE	Bonnor-Ebert; used to denote quantities derived from modelling an object as a Bonnor-Ebert sphere
bm	beam; SCUBA's beamsize is $\sim 14''$
C	measure of central concentration of clumps; used in fitting to Bonnor-Ebert spheres
f_0	peak flux of submillimetre clumps, measured in Jy/beam
κ_{850}	dust grain opacity at 850 μm; used in conversion of measured submillimetre flux into mass
λ	measure of importance of self-gravity used in parameterizing Bonnor-Ebert spheres (defined as the ratio of central to edge density)
$M_\odot$	solar masses
N_H	hydrogen column density (in number)
pc	parsecs
S_{850}	total flux within submillimetre clumps, measured in Jy
σ	radius measure in 2D Gaussians (of the form $Ae^{-\frac{r^2}{2\sigma^2}}$)

σ_C	parameter in Clumpfind algorithm controlling the levels data is divided into for clump identification
σ_e	‘effective separation’; the σ of the 2D Gaussian fit to an extinction core *in the direction of the separation vector* between the core centre and object of interest

Bibliography

Adams, F. C., Lada, C. J., Shu, F. H. 1987, ApJ, 312, 788

Alten, V. P., Bally, J., Devine, D., & Miller, G. J. 1997, IAU Symp. 182: Herbig-Haro Flows and the Birth of Stars, 182, 51P

Alves, J., Lada, C., & Lada, E. A. 2001, Nature, 409, 159

Alves, J., et al 2005, in preparation

Bachiller, R. & Cernicharo, J. 1984, A&A, 140, 414

Bachiller, R. & Cernicharo, J. 1986, A&A, 168, 262

Bachiller, R., del Rio Alvarez, S., & Menten, K. M. 1990, A&A, 236, 461

Bachiller, R., Martin-Pintado, J., & Planesas, P. 1991, A&A, 251, 639

Ballesteros-Paredes, J., Klessen, R. S., & Vázquez-Semadeni, E. 2003, ApJ, 592, 188

Barnard, E. E. 1913, ApJ, 38, 496

Barnard, E. E. 1919, ApJ, 49, 1

Barranco, J. A. & Goodman, A. A. 1998, ApJ 504, 207

Basu, S. 1997, ApJ, 485, 240

Basu, S. & Ciolek, G. E. 2004, ApJ, 607L, 39

Bonnell, I. A. 2005, from IMF@50 (astroph-0501258)

Bonnor, W. B. 1956, MNRAS, 116, 351

Briceño, C., Luhman, K. L., Hartmann, L., Stauffer, J. R., & Kirkpatrick, J. D. 2002, ApJ, 580, 317

Burkert, A. & Hartmann, L. 2004, ApJ, 616, 288

Cambrésy, L. 1999, A&A, 345, 965

Carpenter, J. 2000, AJ, 120, 3139

Cernis, K. 1990, Ap&SS, 166, 315

Cohen, M. & Kuhi, L. V. 1979, ApJS, 41, 743

Crutcher, R. 1999, ApJ, 520, 706

Dame, T. M., Ungerechts, H., Cohen, R. S., deGeus, E. J., Grenier, I. A., May, J., Murphy, D. C., Nyman, L.-A., Thaddeus, P. 1987, ApJ, 322, 706

de Zeeuw, P. T., Hoogerwerf, R., de Bruijne, J. H. J., Brown, A. G. A., & Blaauw, A. 1999, AJ, 117, 354

Di Francesco, J., André, P., & Myers, P. C. 2004, ApJ, 617, 425

Ebert, R. 1955, Z. Astrophys., 37, 217

Elmegreen, D. 1998, ASPC, 148, 150

Emerson, D. T., Klein, U., & Haslam, C. G. T. 1979, A&A, 76, 92

Evans, N. J., et al. 2003, PASP, 115, 965

Fatuzzo, M. & Adams, F. C. 2002, ApJ, 570, 210

Goodman, A. A., Crutcher, R. M., Heiles, C., Myers, P. C., & Troland, T. H. 1989, ApJL, 338, L61

Goodman, A. A., Barranco, J. A., Wilner, D. J., & Heyer, M. H. 1998, ApJ, 504, 223

Goodman, A. A. 2004, ASP Conf. Ser.: Star Formation in the Insterstellar Medium, p171

Hartmann, L. 1998, Accretion Processes in Star Formation(Cambridge: Cambridge University Press)

Hartmann, L., Ballesteros-Paredes, J., Bergin, E. 2001, ApJ, 562, 852

Hatchell, J., Richer, J. S., Fuller, G. A., Qualtrough, C. J., Ladd, E. F., & Chandler, C. J. 2005, A&A, in press

Herbig, G. H. & Jones, B. F. 1983, AJ, 88, 1040

Herbig, G. H. 1998, ApJ, 497, 736

Heyer, M. H. & Brunt, C. B. 2004, ApJ, 615L, 45

Hiemstra, B. 1938, PGro, 48, 1

Hirano, N., Kameya, O., Kasuga, T., Mikami, H., Saito, S., Umemoto, T., & Yamamoto, S. 1994, Astronomical Society of the Pacific Conference Series, 59, 224

Hirano, N., Kameya, O., Mikami, H., Saito, S., Umemoto, T., & Yamamoto, S. 1997, ApJ, 478, 631

Hirano, N., Kamazaki, T., Mikami, H., Ohashi, N., & Umemoto, T. 1999, Star Formation 1999, Proceedings of Star Formation 1999, held in Nagoya, Japan, June 21 - 25, 1999, Editor: T. Nakamoto, Nobeyama Radio Observatory, p. 181-182

Holland, W.S., et al. 1999, MNRAS, 303, 659

Johnstone, D. & Bally, J. 1999, ApJ, 510l, L49

Johnstone, D., Wilson, C.D., Moriarty-Schieven, G., Giannakopoulou-Creighton, J., & Gregersen, E. 2000, ApJ, 131, 505

Johnstone, D., Wilson, C.D., Moriarty-Schieven, G., Joncas, G., Smith, G., Gregersen, E., & Fich, M. 2000, ApJ, 545, 327

Johnstone, D., Fich, M., Mitchell, G.F. & Moriarty-Schieven, G. 2001, ApJ, 559, 307

Johnstone, D., Di Francesco, J., & Kirk, H. 2004, ApJ, 611L, 45

Johnstone, D., Matthews, H., & Mitchell, G. 2005, ApJ, submitted

Kenyon, S. J., Dobrzycka, D., & Hartmann, L. 1994, AJ, 108, 1872

Klessen, R. S., Ballesteros-Paredes, J., Vázquez-Semadeni, E., & Duran-Rojas, C. 2005, ApJ, 620, 786

Kramer, C., Stutzki, J., Rohrig, R. & Corneliussen, U. 1998, A&A, 329, 249

Kroupa, 2002, Science, 295, 82

Kuiper, T. B. H., Whiteoak, J. B., Fowler, J. W., Rice, W. 1987, MNRAS, 227, 1013

Lada, C. J., Lada, E. A., Clemens, D. P., & Bally, J. 1994, ApJ, 429, 694

Lada, C., & Lada, E. 2003, ARA&A, 41, 57

Ladd, E. F., Lada, E. A., & Myers, P. C. 1993, ApJ, 410, 168

Larson, R. B. 1981, MNRAS, 194, 809

Larson, R. B. 2004, from IMF@50 (astroph-0406624)

Larson, R. B. 2005, MNRAS, 359, 311

Leorat, J., Passot, T., & Pouquet, A. 1990, MNRAS, 243, 293

Lombardi, M. & Alves, J. 2001, A&A, 377, 1023

Loren, R. B. 1989, ApJ, 338, 902

Matthews, B. C. & Wilson, C. D. 2002, ApJ, 574, 822

Matthews, B. C., Hogerheijde, M. R., & Bergin, E. A. 2005 (in prep.)

MacLow, M-M. & Klessen, R. 2004, RvMP, 76, 125

McKee, C. 1989, ApJ, 345, 782

Mestel, L. & Spitzer, L. 1956, MNRAS, 116, 503

Motte, F., André, P., Neri, R. 1998, A&A, 336, 150

Mouschovias, T. C. 1976, ApJ, 207, 141

Mouschovias, T. C. & Ciolek, G. E. 1999, NATO ASIC Proc. 540: The Origin of Stars and Planetary Systems, 305

Myers, P. C. 2005, ApJ, 623, 280

Nakamura, F. & Li, Z. 2005, astroph - 0502130

Nakano, T. 1984, Fundamentals of Cosmic Physics, 9, 139

Neugebauer, G. et al. 1984, ApJ, 278L, 1

Onishi, T., Mizuno, A., Kawamura, H. O., & Fukui, Y. 1998, ApJ, 502, 296

Padoan, P., Bally, J., Billawala, Y., Juvela, M., Nordlund, A. 1999, ApJ, 525, 318

Padoan, P. & Nordlund, A. 2004, from IMF@50 (astroph-0411474)

Palmer, P., Zuckerman, B., Buhl, D., Snyder, L. E. 1969, ApJ, 156L, 147

Palla, F. & Stahler, S. W. 2002, ApJ, 581, 1194

Press, W. H., Flannery, B. P., Teukolsky, S. A. 1992, Numerical Recipes in C (Cambridge : Cambridge University Press)

Reid, M. A. & Wilson, C. D. 2005, ApJ, 625, 891

Reipurth, B. & Bally, J. 2001, ARA&A, 39, 403

Ridge, N. A., Schnee, S. L., Goodman, A. A., Li, J. G., Foster, J. B., ApJ, 2005, submitted

Salpeter, E.E. 1955, ApJ, 121, 161

Sánchez, N., Alfaro, E. J., Pèrez, E. 2005, ApJ, 625, 849

Scalo, J. M. 1985, Protostars and Planets II, 201

Shu, F. H. 1983, ApJ, 273, 202

Shu, F., Adams, F., Lizano, S. 1987, ARA&A, 25, 23

Skrutskie, M. F., et al. 1997, in The Impact of Large Scale Near-IR Sky Surveys, ed. F. Garzon, N. Epchtein, A. Omont, W. B. Burton, & P. Persi (Dordrecht: Kluwer), 25

Tachihara, K., Mizuno, A., & Fukui, Y. 2000, ApJ, 528, 817

Tafalla, M., Myers, P. C., Caselli, P., Walmsley, C. M., Comito, C. 2002, ApJ, 569, 815

Tafalla, M., Myers, P. C., Caselli, P., & Walmsley, C. M. 2004, A&A, 416, 191

Tassis, K. & Mouschovias, T. 2004, ApJ, 616, 283

Tilley, D. A. & Pudritz, R. E. 2004, MNRAS, 353, 769

Ungerechts, H. & Thaddeus, P. 1987, ApJS, 63, 645

Vázquez-Semadeni, E. Kim, J., Shadmehri, M., Ballesteros-Paredes, J. 2005, ApJ, 618, 344

Walawender, J., Bally, J., Reipurth, B., & Aspin, C. 2004, AJ, 127, 2809

Walawender, J., Bally, J., Kirk, H., Johnstone, D. (2005), ApJ, accepted

Walawender, J., Bally, J., & Reipurth, B. 2005, AJ, 129, 2308

Williams, J.P., de Geus, E.J., & Blitz, L. 1994, ApJ, 428, 693

Williams, J. P., Bergin, E. A., Caselli, P., Myers, P. C., Plume, R. 1998, ApJ, 503, 689

Wilson, R. W., Jefferts, K. B., & Penzias, A. A. 1970, ApJ, 161, L43

Wolf-Chase, G. A., Barsony, M., O'Linger, J. AJ, 120, 1467

Womack, M., Ziurys, L. M., & Wyckoff, S. 1992, ApJ, 387, 417

Yan, J., Wang, H., Wang, M., Deng, L., Yang, J., & Chen, J. 1998, AJ, 116, 2438

Young, C. H. & Evans, N. J. II 2005, astroph/0503456

Zweibel, E. G. 2002, ApJ, 567, 962

University of Victoria Partial Copyright Licence

Title of Dissertation:

Understanding Star Formation in the Perseus Molecular Cloud

Author: ______________________

Helen M. Kirk
August 19, 2005